Study of Electron-Impact Induced Fragmentation of Thymine

Francis Anthony Mahon

A thesis submitted for the degree of Masters of Science

NUI MAYNOOTH
Ollscoil na hÉireann Má Nuad

Department of Experimental Physics
N.U.I. Maynooth
Maynooth
Co.Kildare

May 2013

Head of Department
Professor J. Anthony Murphy

Research Supervisor
Dr. Peter J. M van der Burgt

Contents

Chapter 1. Introduction

Chapter 2. Principles and Instrumentation of Mass Spectrometry

Chapter 3. Experimental setup

Chapter 4. Interfacing, Data acquisition and Data analysis software

Chapter 5. Test measurements with thymine

Chapter 6. Electron impact fragmentation of thymine

Abstract

The aim of the experiment described in this thesis was to generate a molecular beam of thymine and to investigate the fragmentation processes induced by low-energy electron impact. A molecular beam of thymine is generated by placing thymine in powder form inside a resistively heated oven. The beam of thymine is then crossed by a pulsed electron beam from an electron gun that consists of four electrostatic lens elements and a deflection system for steering the beam. A reflectron time-of-flight mass spectrometer with a microchannel plate detector is used to detect and mass resolve the positively charged fragments. LabVIEW based data acquisition techniques are used to accumulate the time-of-flight data as a function of electron impact energy.

The work described in this thesis is based on a single data set of thymine with electric impact energy varied from 0.5 to 99.7 eV in steps of 0.5 V. To determine the yield of the various fragment ions, groups of peaks were fitted with a sequence of normalised Gaussian peaks using a specially developed LabVIEW program. Using this program the fitting of the peaks was done automatically for all electron energies. Excitation functions for the most positively ionised fragments have been extracted/or determine and their appearance energies have been determined and compared to current research on thymine. Because all excitation functions have been generated from this single data set and assuming that the detection efficiency of the RTOFMS is mass independent, the yield of all fragments are on the same relative scale and are comparable. Total ionisation cross sections have been obtained for our data set and are in good agreement with theoretical calculations.

CHAPTER 1

Introduction

1.1 Radiation damage of DNA

In recent years a lot of research has focused on the interaction of low energy electrons with biomolecules such as the DNA bases, after experiments in Leon Sanche's group in Sherbrooke (Canada) showed that low energy electrons are very effective in causing DNA strand breaks [1]. Of the secondary species generated when high-energy ionizing radiation interacts with living cells, low energy electrons (with energies less than 20 eV) are the most abundant [2].

Experimental techniques such as mass spectrometry and electron spectroscopy are being used in many laboratories to study the building blocks of biomolecules in the gas phase [3-5]. These techniques allow detailed information on the properties of molecules and the dynamics of reactions to be explored.

Biological effects on a cell can result from both direct and indirect action of radiation. Direct effects such as a strand break in DNA are produced by the initial action of the radiation itself and indirect effects are caused by the later chemical action of free radicals and other secondary radiation products. An example of an indirect effect is a strand break that results when an OH radical attacks a DNA sugar at a later time (between about 10^{-12} s and 10^{-9} s) [6]. Depending on the dose and the type of radiation, the biological effects of radiation can differ widely. Some effects can occur rapidly while others may take years to become evident. The types of DNA damage produced by radiation can be broadly classified as single-strand breaks, double-strand breaks and base damages. These structural changes and errors in their repair can lead to gene mutations and alterations in the chromosome. Presently, a great deal is understood about damage repair and misrepair in DNA and its relation to potential tumor induction, but how a cell operates to deter or prevent the transmission of genetic damage is still largely an open question. Molecular genes at specific stages of the cell reproductive cycle appear to recognise and react to the management and repair of damaged DNA. [7]

For genetic alterations to occur in a cell, the cell nucleus must be traversed by a charged-particle track. Nearby cells called bystanders can also sustain genetic damage, even though no tracks pass through them and they receive little or no radiation dose. In some systems, a small dose of radiation triggers a cellular response that protects the cells from a larger dose of radiation. Radiation used to protect biological material is being successfully practiced in tumor therapy. The problem in tumor therapy is to only expose the cancerous material while keeping all other areas unirradiated. One method of treatment uses radiosensitisers with the effect that the sensitised cancerous cells will be destroyed with radiation dosages that leave the healthy material essentially unaffected.

The most important component of the cell nucleus is Deoxyribonucleic acid (DNA). This is the part of the cell nuclei where genetic information is stored. DNA is a biopolymer consisting of two strands containing the 4 heterocyclic bases, thymine (T), adenine (A), cytosine (C) and guanine (G). Each of these bases are bound to the DNA backbone which itself is composed of phosphate and sugar units. Both strands of the DNA are connected through reciprocal hydrogen bonding between pairs of bases in opposite positions. The geometry is such that, adenine pairs with thymine (AT) and guanine with cytosine (GC). [7]

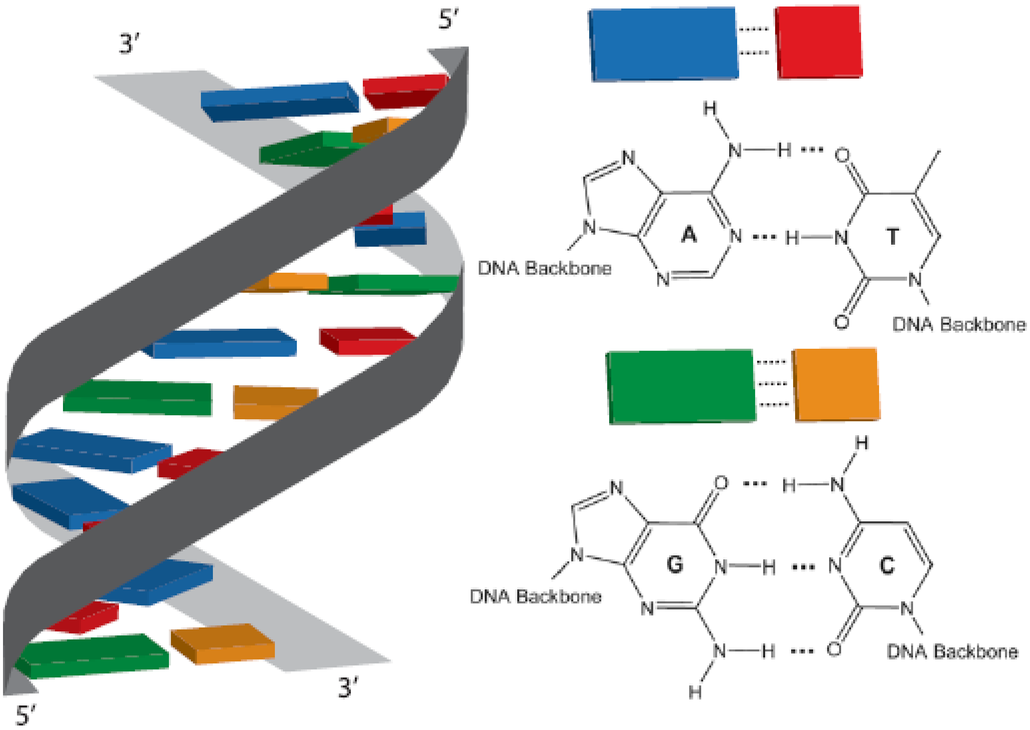

Figure 1.1. Helical Structure of DNA including the DNA bases adenine (A), thymine (T), cytosine (C) and guanine (G) [7]

The structure of the thymine molecule studied in this thesis is shown in figure 1.2

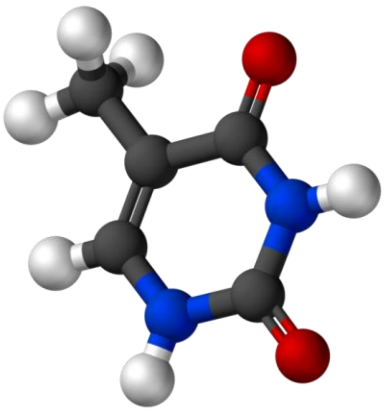

Figure 1.2. Structure of the thymine molecule. [8]

In order to understand the effect of high energy radiation on DNA, one must consider this interaction in terms of its chronological sequence. Consider a beam of protons at energies in the keV - MeV range. The primary photon interaction either absorption or scattering, removes electrons from essentially any occupied state. These can range from valence orbitals to core levels. Depending on the energy of these ionized electrons, they induce further ionization events thereby losing energy and slowing down. These electrons are usually assigned as secondary although they are the result of primary, secondary and tertiary interactions [7]. The estimated quantity is 10^4 secondary electrons per 1 MeV primary quantum [10].

The sequence described above can involve any of the cell components (DNA, water, proteins) separately or in any combination. Water is the most abundant component of a cell and generates the reactive OH radical which can attack any cell component in its surrounding. It is assumed that damage of the genome in a living cell by ionizing radiation is about one third direct and two third indirect. [11]

Direct damage concerns energy deposition and reactions directly in the DNA and its closely bound water molecules. Indirect damage concerns energy disposition in water molecules and the other biomolecules in the vicinity of the DNA. Most of the indirect damage is believed to occur from the attack by the highly reactive hydroxyl radical OH. [6]

There are three major processes and reactions that occur in the molecular network of a living cell. [9]

(i) *The physical stage*. This refers to processes and reactions in the fs and ps time frame after the primary interaction. In this time frame, electronic excitation and ionization occur along with subsequent bond ruptures to create radicals like OH and also an abundant number of secondary electrons.

(ii) *The chemical stage*. This includes molecular relaxation which involves multiple bond cleavages and the subsequent formation of new molecules. At this stage, free radicals take part in an array of reactions which include enzymatic repair and rejoining of DNA breaks that reduce the initial damage that can occur in the physical stage.

(iii) *The biological stage*. This stage refers to the changes occurring on a longer time scale, including the overall response of the system which could extend over a time range of several years. Cell functions can be affected within minutes. The majority of DNA strand breaks are repaired but, the unrepaired strands lead to cell death. Some of the damage to the DNA might not induce cell death but can pass mutations on to the daughter cells.

1.2 Low energy electrons in DNA damage

High energy quanta generate large amounts of electrons at initial energies up to some tens of eV. It is these electrons that are responsible for triggering the reactions that are relevant to direct damage of DNA. Low energy electrons (<10 eV) are especially responsible for strand breaks in DNA.

Single strand (SSB) breaks occur when one of the two backbones is broken. To repair damage to one of the two paired molecules, there exist a number of excision repair mechanisms that remove the damaged nucleotide and replace it with an undamaged one. There are three pathways that exist to repair single strand breaks, these are base excision repair, nucleotide excision repair and mismatch repair [12].

When two chains are broken within a short distance, the damage is referred to as a Double strand break (DSB). The DSB damage is difficult for the cell to repair and without reparation the cell can mutate or eventually die. Three mechanisms exist for repair of DSB [13], [14].

The role low energy electrons would have in DNA damage became more evident after experiments conducted by Sanche and co-workers in 2000 [10]. The group used an electron beam over the energy range of 3–30 eV to irradiate plasmid DNA. They observed the appearance of SSB and DSB at energies above 15 eV, with strand breaks continuously increasing as a function of electron energy. Most notably, they observed SSB and DSB in the range below the ionization threshold (<10 eV). Further experimentation by Sanche and co-workers [15] in 2004, saw the electron energy being brought down to a range of 0-3 eV where strand breaks were detected at 3 eV and peaking at 0.8 eV. Although at this low range, the resonances were found to be solely associated with DSB. These finding were completely unexpected, because before 2004 it was believed that only electrons at energies above the isolation threshold could damage DNA.

1.3 Dissociative Electron Attachment (DEA)

At low energies, below the electronic excitation level, electrons can be captured by molecules into transient negative ions which subsequentially decompose into several fragments. This process is called dissociative electron attachment (DEA), and schematically it can be written as:

$$\mathrm{AB} + \mathrm{e}^{-} \rightarrow \mathrm{AB}^{-*} \rightarrow \mathrm{A} + \mathrm{B}^{-} \text{ or } \mathrm{A}^{-} + \mathrm{B}$$

This process is initiated when an electron becomes temporarily trapped in a resonant state of a molecule. This resonance can either decay by the emission of the extra electron (auto detachment), leaving the molecule in the ground state or in a vibrationally exited state, or it can dissociate in the same manner as the above equation. The dissociation will only occur if the electron energy is sufficient and the resonance is long lived. Burrow *et al* [16] have attributed the sharp peaks observed in the DEA cross sections of uracil and thymine at energies below 3 eV to vibrational Feshback resonances, in which the electron is weakly bound to a vibrationally excited level of the molecule. Hotop *et al* [17] have reviewed experimental investigations of resonance and threshold phenomena occurring in low energy electron collisions with molecules, at electron energies below 1 eV.

DEA experiments were conducted in 2003 by Pan *et al* [18]. Two types of DNA sample were bombarded with low energy electrons: synthetic 40-base-pair linear DNA and natural plasmid DNA which was purified from bacteria. The linear DNA was formed from complementary oligonnucleotides, 40 nucleotides in length, purified by polyarcylamide gel electrophoresis [18]. Once the samples were prepared, they were transferred to a rotary target holder housed in an UHV chamber via a gate valve. The samples were irradiated by an electron gun producing a beam of 1.5 nA on a 4 mm^2 spot with an energy spread of 0.5 eV full width at half maximum. Pan *et al* [18] demonstrated that DEA is involved in low energy electron induced DNA damage, and exhibits a maximum intensity around 9-9.5 eV. This is close to the maximum in the yields of SSB and DSB induced by the low energy electrons on DNA. DEA is therefore not limited to small molecules, but can also occur in extremely large molecules which induce fragmentation and produce anions and radicals. The results reported from this experiment indicate that H produced from DEA to DNA arises principally from the bases and the sugar ring of the backbone whereas O is produced from fragmentation in the backbone. The main results are shown in figure 1.2. The incident electron energy dependence of the H, O and OH yields from 40-base-pair DNA is represented as A in figure 1.3. They exhibit a single broad peak near 9 eV with a continuous rise at higher energies. Low energy electron bombardment of natural DNA is represented as curve B and they exhibit the same characteristics as shown in A. Curves C, D and E exhibit the H yield functions from films of thymine, amorphous ice and α-tetrahydrofuryl alchohol [18]. These curves indicate that DEA to the ring is the main H desorption pathway, but the H peak energy from amorphous ice in curve D is too low to be associated with DEA.

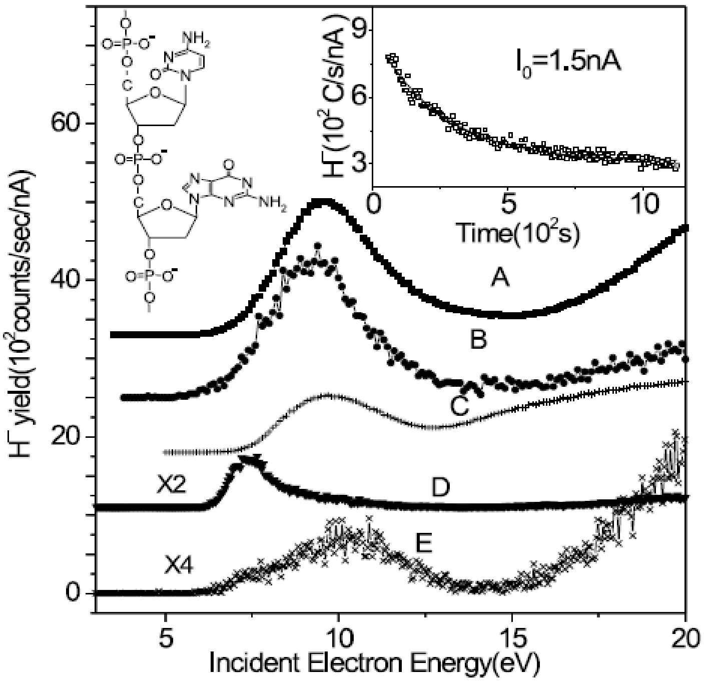

Figure 1.2. Incident electron energy dependence of H⁻ yields from thin films of: A) double stranded DNA, B) supercoiled plasmid DNA, C) thymine, D) amorphous ice and E) ribose analog [18]. The dependence of the magnitude of the H⁻ signal on time of exposure to the electron beam is shown by the open squares in the upper right inset. The solid line is an exponential fit to the data.

1.4 Experiments in thymine

This section outlines the fragmentation pathways that occur in thymine and details the major experiments that have been conducted using thymine and the results obtained. Experiments using techniques such as electron impact via DEA or ionization, ion impact, photon impact and collision experiments with clusters are also described. A brief overview of research and goals for this project is also detailed in section 1.5.

1.4.1 DEA

DEA experiments were conducted by Heuls *et al* [19]. They measured the electron energy dependence for production of anion fragments, induced by resonant attachment of subionisation electrons to thymine and cytosine. Their measurements suggest that this resonant mechanism may relate to critical damage of irradiated cellular DNA by subionisation electrons prior to thermalisation.

In 2003, Denifl *et al* [20] conducted an experiment to study DEA to thymine using an electron/molecule beam apparatus where the electron beam was formed in a custom built hemispherical electron monochromator with a resolution of 30 meV. In their measurements they could not observe the negative thymine parent ion (T^-) but they observed the dominant $(T\text{–}H)^-$ resonance at 1.05 eV followed by a peak at 1.48 eV and a broad resonance at 1.75 eV. Further advancements in the study of DEA were made by S. Denifl and his team in 2004 [21]. They studied DEA to isolated gas-phase cytosine (C) and thymine (T) and identified the resulting fragments, using a crossed electron beam instrument combined with a quadrupole mass spectrometer. The team discovered again that electron attachment to C and T leads to dissociation into the various fragments without any hint of the C and T parent anions.

For thymine the following 9 fragments were observed within the energy range of 0 to 14 eV [20]:

$$\begin{aligned}
\mathrm{e}+\mathrm{T} \leftrightarrow (\mathrm{T})^{-*} &\rightarrow (\mathrm{T}-\mathrm{H})^{-}+\mathrm{H} && (125\ \mathrm{u})\\
&\rightarrow (\mathrm{T}-2\mathrm{H})^{-}+2\mathrm{H} && (124\ \mathrm{u})\\
&\rightarrow (\mathrm{C_4H_5N_2O})^{-}+\ \text{fragments} && (97\ \mathrm{u})\\
&\rightarrow (\mathrm{C_2H_3N_2O})^{-}+\ \text{fragments} && (71\ \mathrm{u})\\
&\rightarrow (\mathrm{C_3H_2NO})^{-}+\ \text{fragments} && (68\ \mathrm{u})\\
&\rightarrow (\mathrm{C_3H_4N})^{-}+\ \text{fragments} && (54\ \mathrm{u})\\
&\rightarrow (\mathrm{OCN})^{-}+\ \text{fragments} && (42\ \mathrm{u})\\
&\rightarrow (\mathrm{CN})^{-}+\ \text{fragments} && (26\ \mathrm{u})\\
&\rightarrow (\mathrm{O})^{-}+\ \text{fragments} && (16\ \mathrm{u})
\end{aligned}$$

It is noted here that $(\mathrm{T{-}H})^{-}$ indicates the negative ion formed by the detachment of a single proton from the parent thymine molecule. Likewise, $(\mathrm{T{-}2H})^{-}$ indicates the detachment of a hydrogen atom and a proton from the thymine molecule. This notation, which is contrary to standard chemical notation, is commonly used in this research field. Other DEA experiments were conducted by Heuls et al [21]. They measured the electron energy dependence for production of anion fragments, induced by resonant attachment of subionisation electrons to thymine and cytosine. Their measurements suggest that this resonant mechanism may relate to critical damage of irradiated cellular DNA by subionization electrons prior to thermalization.

1.4.2 Bond Selective DEA

S. Ptasinska *et al* [22] studied electron attachment to thymine in the electron energy range 0-15 eV. The formation of fragment anions that are formed by the loss of one or two H atoms is analysed as a function of incident electron energy. In their experimental setup, an effusive beam of neutral molecules is produced by evaporating thymine power in a resistively heated oven up to a temperature of 430 K. Gas phase molecules are introduced through a 1 mm diameter capillary into the collision chamber where they are crossed with a well defined beam of electrons that originate from a hemispherical electron monochromator (HEM). The electrons are produced by a hairpin filament and are accelerated with lens system into a hemispherical electrostatic field analyser. Anions that are formed via electron attachment reactions are extracted by a weak electric field towards the entrance of a quadrupole mass filter where the mass per charge ratio of the anions are analysed.

A) DEA yielding $(T\text{-}H)^-$

They suggest that the dominant negative ions formed via DEA to nucleobases are the closed-shell dehydrogenated molecular anions. For thymine the reaction pathway is:

$$\mathrm{T} + \mathrm{e}^- \rightarrow \mathrm{T}^{-^*} \rightarrow (\mathrm{T} - \mathrm{H})^- + \mathrm{H}^*$$

In thymine, the reaction above can occur at four different positions: $_1N$, $_3N$, $_6C$ or at the carbon atom of the methyl group. The values of the bond dissociation energies (BE) required for the removal of one H atom from the neutral thymine molecule and the electron affinities of the corresponding (T-H) isomers are shown in table 1.1 below.

Bond	BE	EA	BE-EA
^{1}N-H	4.29	3.4	0.89
^{3}N-H	5.8	4.5	1.3
CH_2-H	4.54	1.82	2.23
^{6}C-H	4.98	2.76	2.72

Table 1.1. The values of the bond dissociation energies (BE) and electron affinities (EA) of the corresponding (T-H) isomers [22]

The ion efficiency curve for the mass 125u (T-H) in the range of 0 to 4 eV is shown in figure 1.4. This figure also includes the ion efficiency curve for the partially deuterated thymine masses 129 u (T_D-H) and 128 u (T_{D3}-H). The electron energy resolution for thymine was 60 meV.

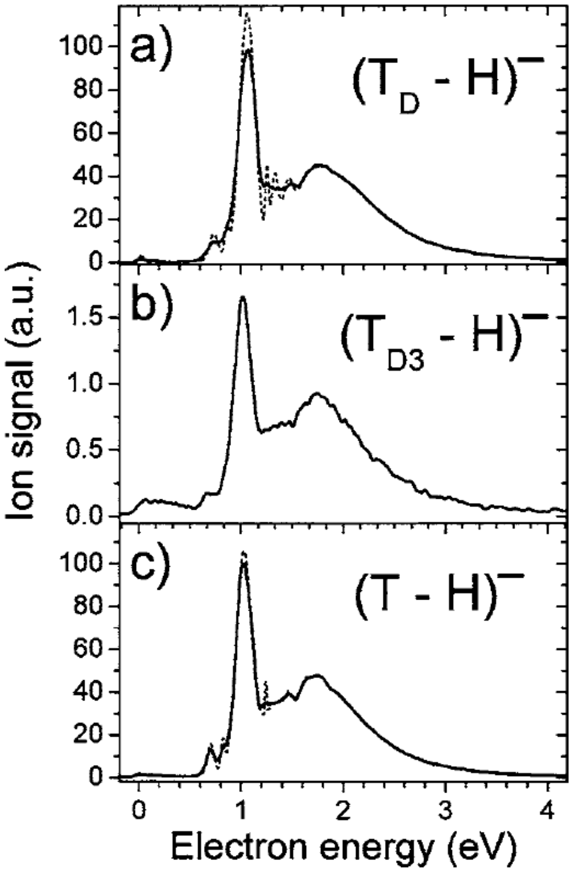

Figure 1.4. ion efficiency curve for the masses (a) 129 u (T_D-H), (b) 128 u (T_{D3}-H) and (C) 125u (T –H) [22].

B) DEA yielding H^-

The formation of H^- is observed and investigated by S. Ptasinska *et al* [22]. The reaction channel is shown below.

$$\mathrm{T} + \mathrm{e}^- \rightarrow \mathrm{T}^{-^*} \rightarrow (\mathrm{T} - \mathrm{H})^* + \mathrm{H}^-$$

This anion was produced in the energy range 5 to 13 eV. In this range, the desorption of H^- from thin films of isolated DNA compounds and single and double strand break formation were observed. The anion yield of H^- exhibits 3 clearly separated peaks centered at 5.5, 6.8 and 8.5 eV. The 5.5 eV peak can be ascribed to the H^- loss from the $_1N$ position. The 6.8 eV peak comes from the H^- loss from the $_3N$ nitrogen atom and the 8.5 eV peak represents the H^- loss from the $_6C$ position.

C) DEA yielding $(T\text{-}2H)^-$

Site selectivity was also observed for the 124 u mass. The ion yield exhibits a well-pronounced narrow resonance close to 0 eV followed by a weak resonance at 1.5 eV. A broad structure of overlapping resonances at electron energies above 6 eV. The two hydrogen atoms that are removed from thymine may be lost as two independent atoms

$$\mathrm{T} + \mathrm{e}^- \rightarrow \mathrm{T}^{-^*} \rightarrow (\mathrm{T} - 2\mathrm{H})^- + \mathrm{H}^* + \mathrm{H}^*$$

or as an intact hydrogen molecule but the binding energy of H_2 reduced the required energy by 4.54 eV

$$\mathrm{T} + \mathrm{e}^- \rightarrow \mathrm{T}^{-^*} \rightarrow (\mathrm{T} - 2\mathrm{H})^- + \mathrm{H}_2$$

The minimum energies required for the removal of either two individual H atoms or one H_2 molecule are determined using high-level quantum-chemical calculations. More bond selective DEA experiments have been conducted by S. Ptasinska *et al* [23], [24] and Abdoul-Carime *et al* [25]

1.4.3 Electron impact on thymine

Rice *et al* [26] study the fragmentation patterns of thymine by recording spectra at low electron beam energies in addition to the standard 70 eV. The solid compounds were introduced directly into the ion source of a double-focusing mass spectrometer. To generate a sufficiently high vapor pressure, the vicinity of the ion source was heated to 200 ^{o}C. Mass spectra were recorded at electron impact energies of 70 and 20 eV. They identified the molecular ion peak at 126 u and intense fragment ion peaks at 83 and 55 u corresponding to the loss of HNCO. Decarbonylation of deuterated 83 u is followed by loss of either a hydrogen or a deuterium atom.

Imhoff *et al* [27] use 70 eV electron impact to study both thymine and thymine-methyl-d3-6-d in the gas phase. A large amount of thymine was deposited on a Pt substrate, which is then placed in front of the entrance of a quadrupole mass spectrometer. The thymine molecules are then evaporated from the Pt into the quadrupole mass spectrometer by warming the Pt substrate to 89-95 ^{o}C and subjected to electron impact. The positive ion fragmentation from thymine produced by 70 eV electron impact is shown in figure 1.5 (a). They observed that the 83 u fragment which formed from the loss of HCNO group from thymine was found to shift to 87 u in the case of thymine-methyl-d3-6-d indicating that it contains the four deuterium atoms. Further loss of a hydrogen atom gives the 82 u fragment which shifts to 85 u in the mass spectrum of thymine-methyl-d3-6-d as a result of further loss of carbon-bound deuterium.

Shafranyosh *et al* [28] used a crossed molecular and electron beam to study the electron impact on thymine and determine the energy dependencies and absolute values of total cross sections for the formation of positive and negative ions of thymine molecules. They found that the maximal cross section for the formation of positive ions is reached at an energy of 95 eV. The results from Rice *et al* [26], Imhoff *et al* [27] and Shafranyosh *et al* [28] will be compared to the results obtained for this report in chapter 6.

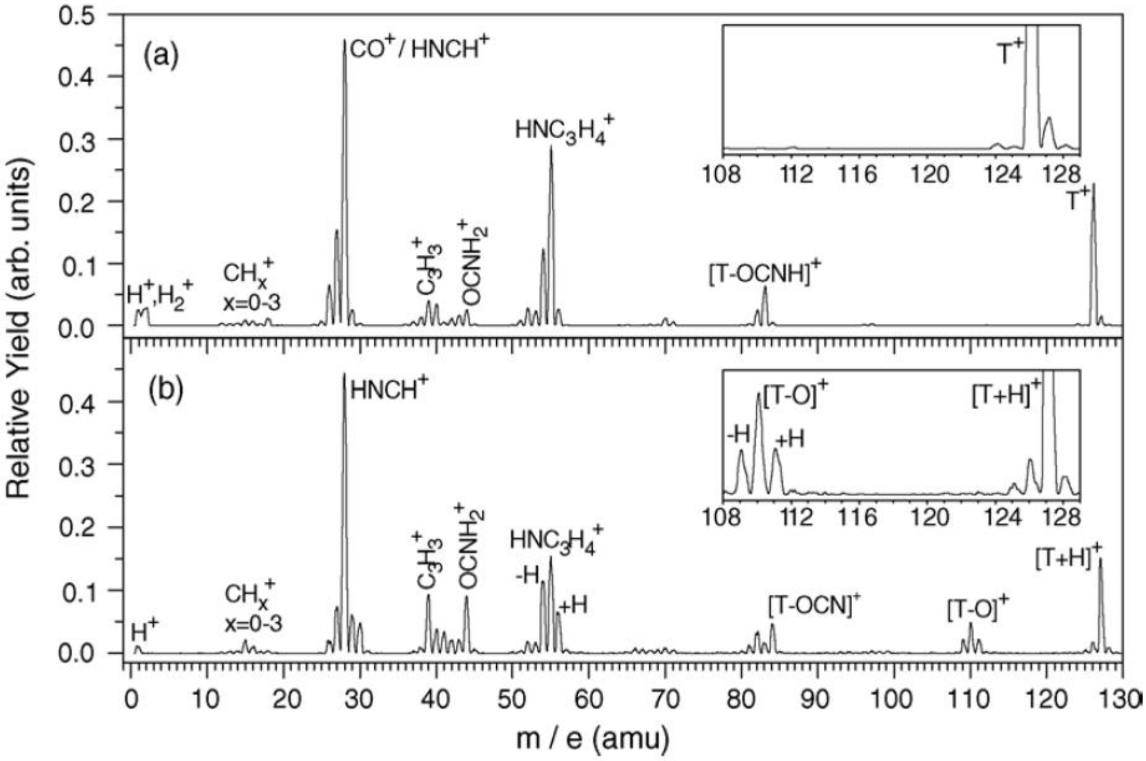

Figure 1.5. The positive ion fragmentation pattern from thymine by (a) 70 eV electron impact in the gas phase and (b) 200 eV Ar$^+$ ion irradiation. [27]

1.4.4 Photon impact on thymine

Jochims *et al* [29] used synchrotron radiation as an excitation source in the 6-22 eV photon energy region to conduct a photoionization study of thymine. They report on the fragmentation patterns, ionization energies and ion appearance of thymine, mostly for the first time. The nucleic acid base vapor was introduced into the ionization chamber by direct evaporation of solid samples in open containers placed 1-2cm below the position of the incident VUV radiation within the ion extraction zone. The chamber was heated to a temperature range of 120 - 140 ^{o}C. A quadrupole mass spectrometer was used to measure the parent and fragment ions formed via photoionization of thymine and ion yield curves were obtained through photon energy scans with measuring intervals of 25 meV. Transmitted photons were detected by the fluorescence of a sodium salicylate coated window.

The primary decay routes of thymine ($C_5N_2O_2H_6$) are shown in figure 1.6 [26]. Described below are the main fragments that can occur in the thymine molecule.

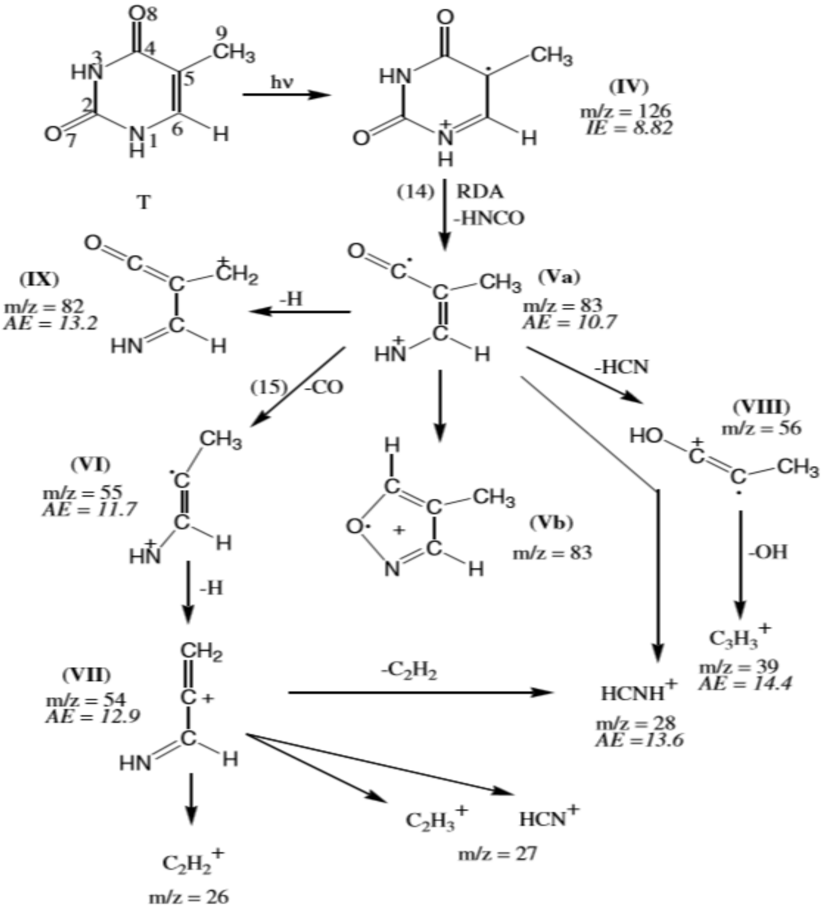

Figure 1.6. The main fragmentation pathways of thymine [29]

They found that the principle fragmentation pathways of the thymine parent cation involves the loss of HNCO. One unit loss gives rise to the 83 u ion with an appearance energy of 10.7 eV.

$$C_5H_6N_2O_2^+ \text{ (126 u)} \rightarrow C_4H_5NO^+ \text{ (83 u)} + HNCO \text{ (43 u)}$$

The 83 u fragment can then lose a CO molecule to form the most abundant ion in the mass spectrum 55 u, whose appearance energy is 11.7 eV

$$C_4H_5NO^+ \text{ (83 u)} \rightarrow C_3H_5N^+ \text{ (55 u)} + CO \text{ (28 u)}$$

The resultant 55 u cation can suffer a loss of a further hydrogen atom to produce the 54 u fragment with an appearance energy of 12.9 eV

$$C_3H_5N^+ \text{ (55 u)} \rightarrow C_3H_4N^+ \text{ (54 u)} + H$$

They also suggest that the 55 u fragment might also have the structure $C_3H_3O^+$ which is brought about by the rupture of the central carbon bond in the 83 u cation. A weak 43 u ion with an appearance energy of 11.9 eV was found, assigned to $HNCO^+$. They suggest that this fragment formed in a reaction corresponding to a charge switch in the reaction which leads to the formation of the 83 u ion above. They suggest the most probable assignment of the 39 u ion is to $C_3H_3^+$, which could be formed by the loss of a hydrogen atom from $C_3H_4^+$ (40 u).

The linear structure of the 54 u ion could give rise to the formation of the 28 u and the 26 u ions by rupture of the central carbon bond.

$$C_3H_4N^+ \text{ (54 u)} \rightarrow HCNH^+ \text{ (28 u)} + C_2H_2 \text{ (26 u)}$$

Less intense fragment ion peaks were also observed but with no appearance energy measurements. A weak ion is observed at 97 u which is $C_4H_3NO_2^+$ resulting from loss of NH_2CH. Some other weak ion peaks were found to occur directly from the parent molecule.

$$C_5H_6N_2O_2^+ \text{ (126 u)} \rightarrow C_2HNO_2^+ \text{ (71 u)} + C_3H_5N \text{ (55 u)}$$

$$C_5H_6N_2O_2^+ \text{ (126 u)} \rightarrow C_2H_2N_2O^+ \text{ (70 u)} + C_3H_4O \text{ (56 u)}$$

Itala *et al* [30] used a photoelectron-photoion-photoion coincidence technique to study the photofragmentation of thymine into cation and neutral fragments following the core ionisation from soft x-rays.

The findings from Jochims *et al* [29] are very important for the current work at Maynooth. The appearance energies of the fragments, ion yields and fragmentation patterns stated in this section will be compared to the results obtained for this report in chapter 6.

1.4.5 Proton impact on thymine

J. Tabet *et al* [31] present the first fragmentation ratios for the ionization of gas-phase DNA bases by 80 keV proton impact. In their experimental setup, protons are produced in a standard RF- gas discharge source and are accelerated to 80 keV with an energy resolution of 0.01 keV. The primary magnetic sector field is used to separate protons from other ions in the source and the background pressure is maintained below 10^{-6} Torr along the beamline. The proton beam is then crossed at right angles with an effusive target beam of thymine. To maximise statistics, the measurements were recorded over a number of days. The temperature range used for the measurements is 125-133 ^{o}C for thymine. A linear time-of-flight mass spectrometer is used to analyse the product ions formed by the collision of a proton with thymine. The mass spectrum for proton impact ionization of thymine by electron capture and direct ionisation is shown in figure 1.7.

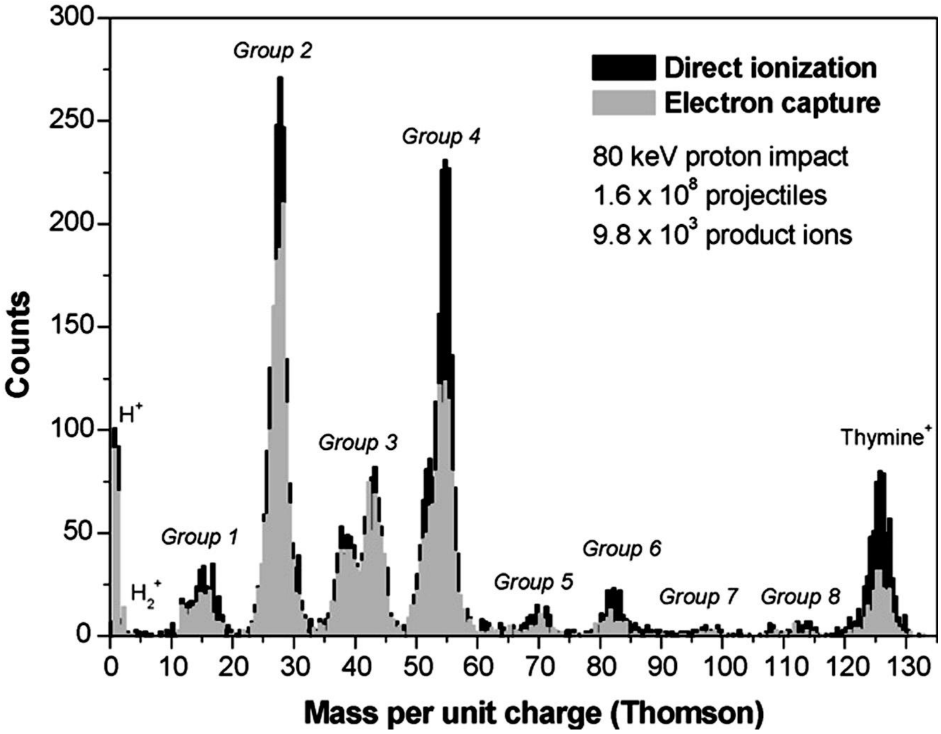

Figure 1.7. Mass spectrum for proton impact ionization of thymine by electron capture and direct ionisation [31]

They found an ionisation energy of 8.82 ± 0.03 eV for thymine. The weak 108-115 u band (group 8) with a maximum at 112 u points to fragmentation around the CH_3 group. The 95-100 u group with a maximum at 98 u is associated with CH_2N. The local maximum at 83 u is due to the lower appearance energy of $C_4H_5NO^+$ (10.7 eV) than $C_4H_4NO^+$ (13.2 eV). $HCNO^+$ production (43 u) is attributed to a charge reversal in the fragmentation associated with group 6 by Jochims *et al* [29] and has been identified as the first step in the most important pathways for sequential fragmentation following ionization. They suggest $C_3H_3^+$ (39 u) production occurs via a sequence of three fragmentations with considerable atomic scrambling. Ion production in the range of 10-20 u shows a local maximum at 15 u which is consistent with the relatively low energy required to break the single C-C bond joining the CH_3 group to the C_4N_2 ring.

1.4.6 Ion impact on thymine

Imhoff *et al* [27] used Ar^+ ion irradiation in the 10-200 eV to study the chemical composition of charged fragments desorbing from 200 ng/cm^2 thymine and thymine-methyl-$d_{3\text{-}6\text{-}d}$ films. A low energy ion beam system delivers a highly focused positive or negative ion beam in the 1-500 eV energy range into a ultra high vacuum reaction chamber for sample film irradiation. A high resolution quadrupole mass spectrometer is installed perpendicularly to the ion beam to monitor desorbing positive and negative ions during ion impact. The positive ion fragmentation pattern from thymine produced by 200 eV Ar^+ ion irradiation of a 200 ng/cm^2 thymine film is shown in figure 1.5 (b).

They identified the major cation fragments produced by Ar^+ impact of thymine films as $HNCH^+$, $HN(CH)CCH_3^+$, $C_3H_3^+$, $OCNH_2^+$, $[T\text{-}OCN]^+$, $[T\text{-}O]^+$, and $[T+H]^+$. They suggest that the anion fragments produced by Ar^+ impact on thymine films are dominated by H^-, O^-, CN^- and OCN^- with smaller amounts of $NC_3H_2^-$, $HNC_3H_3^-$, $OC_3H_3^-$ and other hydrocarbon anions. Positive ion fragment desorption involves exocyclic and endocyclic bond cleavage which extends down to about 15-18 eV for positive ion fragments.

Schlatholter *et al* [32] also conducted ion impact experiments on thymine using an electron cyclotron resonance ion source to generate Xe^{25+} and a time-of-flight mass spectrometer to detect the ions.

1.5 Maynooth research

The apparatus in Maynooth is designed for the study of electron impact on biomolecules and small molecular clusters. Positive ions are detected using a reflectron time-of-flight mass spectrometer. The purpose of the research described in this Masters of Science thesis was to study the interaction of electron impact fragmentation of thymine. The work had several objectives including the identification and comparison of the fragmentation pathways of thymine by electron impact, the measurements of excitation functions, and the determination of appearance energies for all of the fragments observed in the Maynooth thymine mass spectrum. A secondary objective was the development of a LabVIEW program that could fit all of the peaks with normalised gaussians in 0-99.7 eV range from a single data set.

Chapter 2 provides an overview of the principles of mass spectrometry and the reflectron time-of-flight technique used in this project. A brief introduction to other types of mass spectrometry is also included.

Chapter 3 describes the current apparatus. A detailed look is taken at the biomolecular oven, the reflectron time-of-flight mass spectrometer, the electron gun and faraday cup and the interlock box.

Chapter 4 presents the LabVIEW software used for data analysis and data acquisition. A description of the pulsing and timing used in the experiment and the peak fitting program is provided.

Chapter 5 contains various test measurements that were conducted on thymine. These include an examination of the oven temperature and oven depletion, the calibration of the electron gun and mass spectra. An analysis of the water peaks is also provided.

Chapter 6 presents the results from electron impact on thymine. The fragments are identified and compared to other literature and excitation functions of the fragments and the appearance energy of the fragments are also provided.

CHAPTER 2

Principles and Instrumentation of Mass Spectrometry

2.1 What is mass spectrometry?

The basic principle of mass spectrometry is to generate ions from either in-organic or organic compounds by any suitable method, to separate these ions by their mass-to-charge ratio (*m/q*) and to detect them qualitatively and quantitatively by their respective *m/q* and abundance [33]. The ions can be ionized thermally, by electric fields or by impacting energetic electrons, ions or photons. Mass spectrometer instruments consist of three modules: an ion source which converts gas phase sample molecules into ions, a mass analyser, which sorts the ions by their masses by applying electromagnetic fields, and a detector which detects the incoming ions.

The separation of ions with different mass/charge ratios (*m/q*) at an equal kinetic energy in static mass spectrometers is based on the difference of the radii of their trajectories in a uniform dc magnetic field. No combination of static electric fields is capable of separating a flux of such ions by mass. This can only be done by applying periodically changing or pulsed fields. The basic idea is that monoenergetic ions with different *m/q* ratios are given different velocities so that they take different times to traverse a given path in the instrument. By applying a periodically varying or a pulsed electric field in certain parts of the path, one can impart different energies to ions with different velocities, thus making their separation possible. [34]

By properly varying the radio frequency in a quadrupole mass filter, one can measure the whole mass spectrum. If a pulse is applied in a time-of-flight mass spectrometer, a short ion packet is created and ions with different velocities will separate in to their individual packets. This means their consecutive arrival to the detector can be recorded in the form of a mass spectrum. Discussed in this chapter is the time-of-flight technique used for this project and other techniques such as mass filters and mass spectrometry using ion traps.

2.2 Mass filters

A quadrupole mass filter consists of four parallel metal rods arranged as in figure 2.1. Two opposite rods have an applied potential of $(U + V\ \cos\omega t)$ and the other two rods have a potential of $-(U + V\ \cos\omega t)$, where U is a DC voltage and $V\ \cos\omega t$ is an AC voltage. The trajectory of the ions in the flight path are affected by the applied potential between the four rods. Depending on the DC and AC voltages, only ions of a certain mass-to-charge ratio pass through the quadrupole filter and all other ions are thrown out of their original path. By varying the voltages on the rods, a mass spectrum can be obtained by monitoring the ions passing through the quadrupole. The conventions are that x is the horizontal plane and y is the vertical plane when looking directly at the four rods. The x-direction acts as a high-pass mass filter, only high masses will be transmitted to the other end of the quadrupole without striking the x-electrodes. For low mass ions, they stay in phase with the RF drive, gain energy from the field and oscillate with increasingly large amplitude until they encounter one of the rods and are discharged.

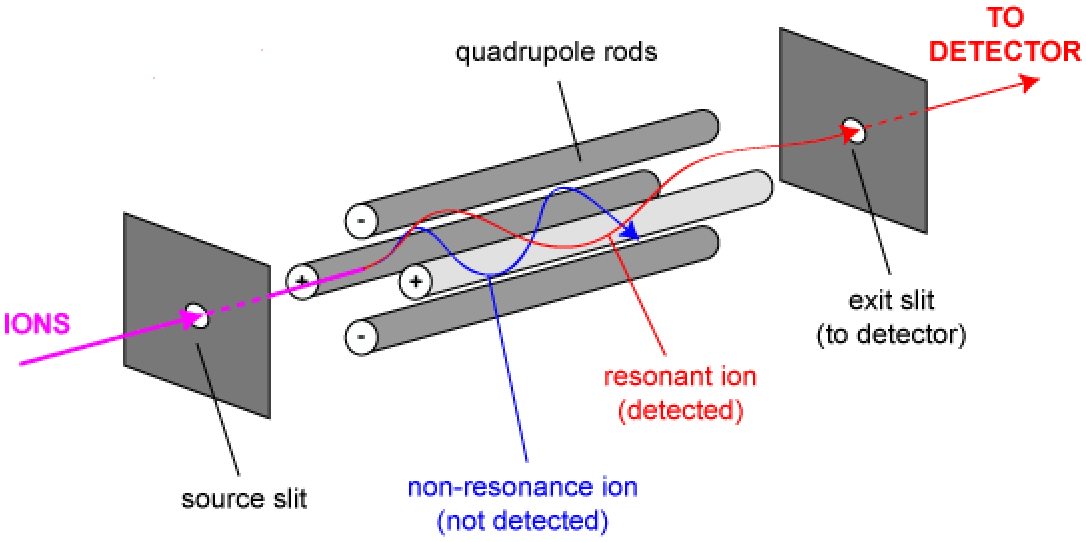

Figure 2.1. Example schematic of a quadrupole mass filter [35]

On the other hand, the y-direction acts as a low-pass mass filter where only low masses will be transmitted to the other end of the quadrupole without striking the y electrodes. Heavy ions will be unstable because of the defocusing effect of the DC component, but some lighter ions will be stabilised by the AC component if its magnitude is such as to correct the trajectory whenever its amplitude tends to increase. By a suitable choice of RF/DC ratio, the two directions together give a mass filter which is capable of resolving individual atomic masses [36].

Disadvantages of quadrupole mass filters are:

1. As a ratio of the voltage (U, V) changes, a limit in the resolution is reached largely determined by the accuracy with which the various quadrupole parameters are controlled and by the initial motion of the ion as it enters the quadrupole field. [34]
2. The efficiency of transmission of ions through the quadrupole decreases as ion mass increases, leading to a relative loss in sensitivity at higher masses.

2.3 Mass spectrometry using traps

The quadrupole ion trap uses constant DC and radio frequency (RF) oscillating AC electric fields to trap ions. The 3D trap consists of two hyperbolic metal electrodes with their foci facing each other and two hyperbolic ring electrodes halfway between the other two electrodes. The ions are trapped in the space between these four electrodes by AC and DC electric fields.

This overlap of a direct potential with an alternative one gives a kind of three-dimensional quadrupole in which the ions of all masses are trapped on a three-dimensional trajectory. In quadrupole instruments, the potentials are adjusted so that only ions with a selected mass go through the rods. In a quadrupole ion trap, ions with different masses are present together inside the trap and are expelled according to their masses to create a mass spectrum. The ions repel each other in the trap which causes an expansion of their trajectories as a function of time. [37]

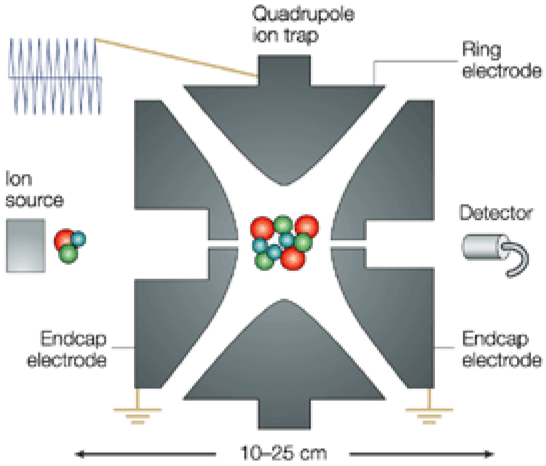

Figure 2.2. Example schematic of a quadrupole ion trap [38]

To avoid ion loss, the trajectory has to be reduced by maintaining in the trap a pressure of helium gas that removes excess energy from the ions by collision.

Shown in figure 2.2 is an example schematic of a quadrupole ion trap. Bari et al [39] used an RF-ion trap combined with a linear time-of-flight mass spectrometer to study keV ion-induced dissociation of protonated peptides.

2.4 Time-of-flight mass spectrometry

The essential principle of time-of-flight mass spectrometry is that ions need to be extracted from an ion source in short pulses and then directed down an evacuated straight tube to a detector. The time taken to travel the length of the flight tube depends on the mass over charge ratio. For singly charged ions, the time taken to traverse the distance from the source to the detector is proportional to a function of mass. When the ions reach the detector, a trace of ion abundance against time of arrival is obtained which is subsequently converted into a mass scale to give the final mass spectrum. A linear time-of-flight mass spectrometer has two acceleration regions both containing different electric fields which are used to accelerate the ions out of the source towards the detector. A reflectron time-of-flight mass spectrometer uses an einzel lens arrangement to accelerate and focus the ion beam towards a reflector which provides second order focussing of the beam towards the detector.

For this project a reflectron time-of-flight mass spectrometer (RTOFMS) by R.M. Jordan Company was used to detect the ions (shown in figure 2.3). The einzel lens arrangement consists of three electrodes whereby the first and third elements accelerate the ions and the second electrode focuses the beam (V_{focus} in figure 2.3). The electrostatic field created in the reflector is at the end of the flight path of the ions and has a polarity the same as that of the ions so they experience a retarding potential. The voltages applied to V_{r1} and V_{r2} in figure 2.3 create this retarding field that acts as an ion mirror by deflecting the ions and sending them back through the flight tube. The reflectron corrects for a small dispersion in the initial energy of the ions with the same m/q ratio. The ions with the slightly higher initial kinetic energy will penetrate the reflectron more deeply and will spend more time in the reflector, thus they reach the detector at the same time as slower ions of the same m/q.

The ions are detected with a microchannel plate detector (MCP). In our RTOFMS, ions of adjacent m/q values are separated by about 20 to 30 ns, when they arrive at the MCP detector. Over a total mass range of 0 - 150 mass units, all of the ions arrive at the detector over a relatively short time range (typically 62 μs in our instruments).

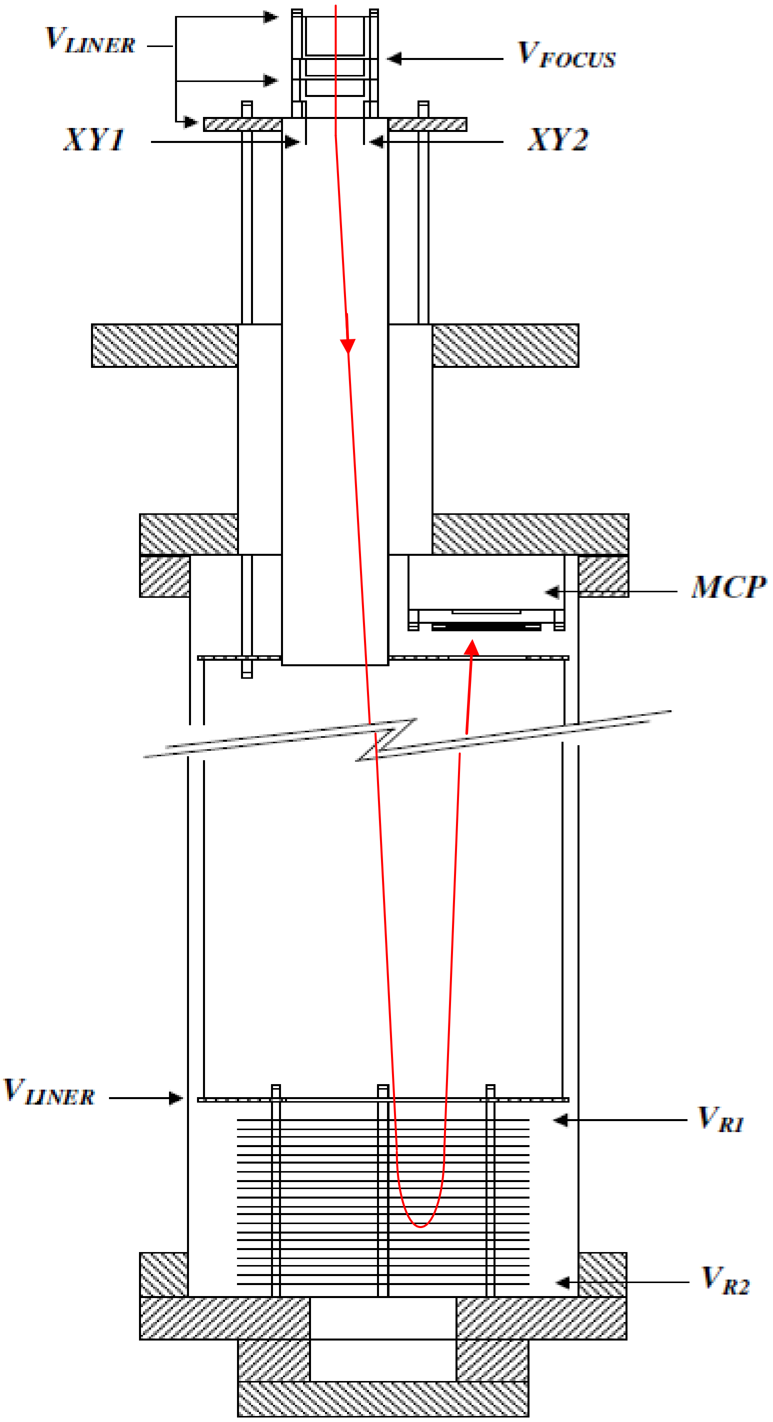

Figure 2.3. Schematic of the reflectron and MCP detector used in this project.

The advantages of time-of-flight mass spectrometry are:

1) With typical voltages on the elements of the TOFMS, a complete spectrum can be obtained every few microseconds (125 µs in our case). This enables the study of how the relative intensities of different ions vary when source conditions change rapidly.

2) An entire mass spectrum can be recorded for each accelerating pulse, thus it is possible to measure relative intensities accurately even though source conditions might vary unpredictably.

3) The accuracy of the TOFMS depends on electronic circuits rather than on extremely accurate mechanical alignment and on the production of highly uniform, stable magnetic fields. [40]

The main disadvantage of TOFMS are their limited resolution. Mass resolution is affected by factors that create a distribution in flight times among ions with the same *m/q* ratio. These factors are the length of the ion formation pulse, the size of the volume where the ions are formed and the variation of the initial kinetic energy of the ions. Digitizers can also affect the resolution and precision of the time measurements.

One solution to this problem in a linear time-of-flight mass spectrometer is delayed pulse extraction. To reduce the kinetic energy spread among ions with the same *m/q* ratio leaving the source, a delay between ion formation and extraction can be introduced. In this method, the ions initially are allowed to separate according to their kinetic energy in the field-free region. For ions of the same *m/q* ratio, those with more energy move further towards the detector than the initially less energetic ions. The extraction pulse applied after a certain delay transmits more energy to the ions that remained for a longer time in the source. [37]

A better way to improve mass resolution is to use a reflectron time-of-flight mass spectrometer. In this project, a reflectron and delayed pulse extraction are used to obtain a good mass resolution and sensitivity. The RTOFMS setup used for this project will be discussed in more detail in section 3.6.

Mass-to-charge ratios are determined by measuring the time that ions take to move through a field-free region between the source and the detector. The relationship between *m/q* and time is discussed below: [41]

The ion TOF in a reflectron can be written as:

$$t = A_0\left[\frac{A_1}{\sqrt{k}} + A_2\left(\sqrt{k} - \sqrt{k-p}\right)\right] \tag{1}$$

where $k = \frac{U}{U_0}$ and $p = \frac{U_b}{U_0}$

We define the following quantities independent of m, q:

$$A_1 = \frac{L_1+L_2}{4d_r U_o} \text{ and } A_2 = \frac{d_b}{d_r}\frac{U_r}{U_b}$$

where U_b is the potential in the decelerating gap d_b; U_r is the potential difference in the reflecting gap d_r. L_1 and L_2 are the lengths of the drift spaces, qU_0 is the mean ion energy and qU is the ion energy corresponding to the ion velocity components parallel to the instruments axis.

$$A_0 = \frac{4d_r}{\sqrt{\frac{2qU}{m}}}\frac{U_0}{U_r} = \frac{4d_r}{\sqrt{2U}}\frac{U_0}{U_r}\sqrt{\frac{m}{q}}$$

Inserting quantities A_1, A_2 and A_0 into equation (1) the ion flight time becomes:

$$t = A\sqrt{\frac{m}{q}} \tag{2}$$

with $A = \frac{4d_r}{\sqrt{2U}}\frac{U_0}{U_r}\left[\frac{A_1}{\sqrt{k}} + A_2\left(\sqrt{k} - \sqrt{k-p}\right)\right]$

To allow for the adjustment of the time delay between extraction and the start of the MCS card, a constant *B* is added to equation (2) which becomes:

$$t = A\sqrt{\frac{m}{q}} + B$$

The relationship between *m/q* and time becomes:

$$\frac{m}{q} = (Ct + D)^2$$

Where $C = \frac{1}{A}$ and $D = -\frac{B}{A}$

This relation is used to calibrate the *m/q* scale of the mass spectra in section 5.3. This will allows us to indentify the fragments appearing in our spectrum.

CHAPTER 3

Experimental setup

3.1 General overview of the experiment

The main purpose of this chapter is to describe the apparatus used for the research described in this thesis. The components of the system are discussed individually in detail under their relevant headings. Detailed below is a general overview of the experiment.

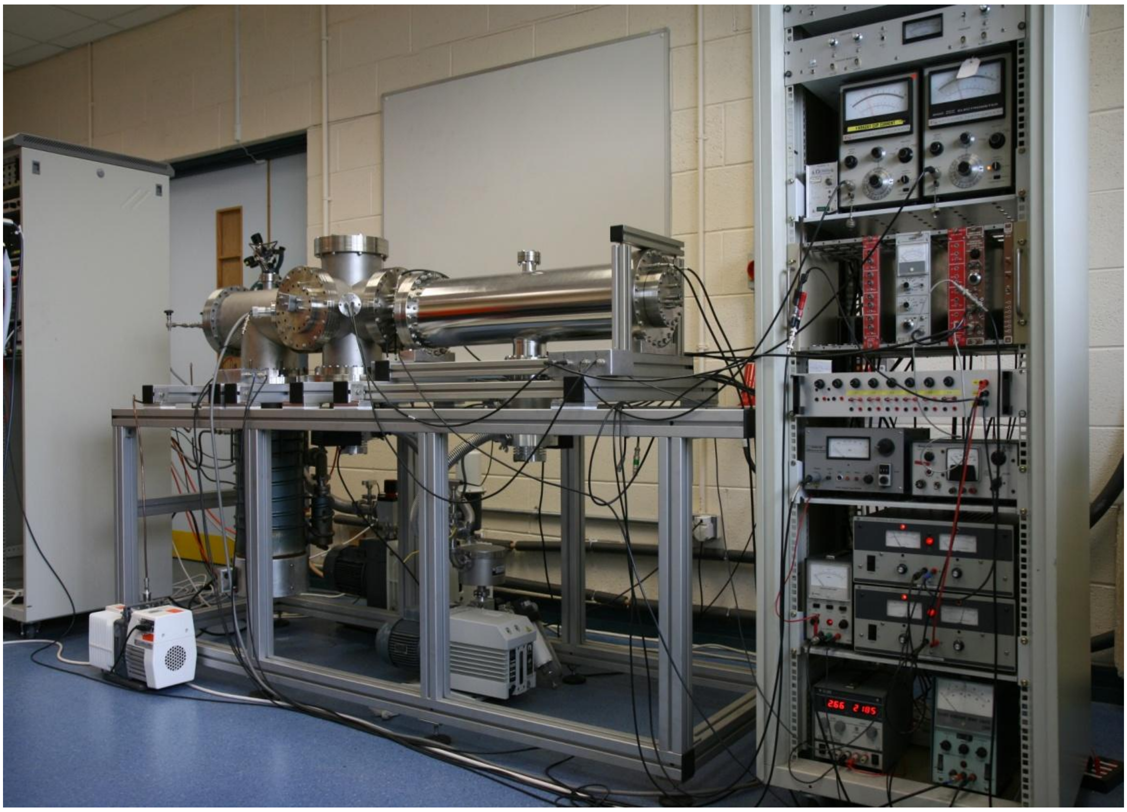

Figure 3.3. Experimental setup used for this project.

The three chambers (see figure 3.2) are: the expansion chamber where a pulsed supersonic beam of thymine is generated, the interaction chamber where the clusters are fragmented using a pulsed electron beam and the reflectron chamber which houses the reflectron time-of-flight mass spectrometer (RTOFMS) where the reaction products are detected.

Five pumps are used in specific places to keep a suitable vacuum throughout the system. In the expansion chamber, a diffusion pump coupled with a rotary vane pump is used to keep the pressure to 7.5x10^{-7} mbarr when the oven is in operation. Two turbomolecular pumps work in tandem with a single rotary vain pump to keep the vacuum in the interaction chamber and the RTOFMS at a pressure of 1.7x10^{-8} mbarr. The entire vacuum system rests upon an in-house designed and built frame, made from aluminium. In order to access the instruments inside the vacuum chambers, the frame has sliding rails which allows the vacuum chamber to be disconnected and moved apart to access the components in the interior.

For this project, either copper gaskets or rubber O-rings were used to join metal flanges together and provide a vacuum seal. Shown below in figure 3.2 is the schematic of the vacuum system used in this project.

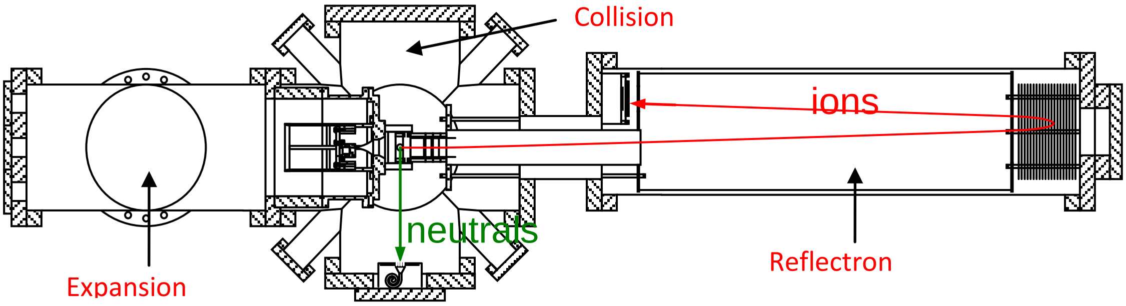

Figure 3.2. Schematic of the vacuum system used for this project

3.2 The expansion chamber

In the expansion chamber a pulsed beam of biomolecules is created using a resistively heated oven. The chamber is held under vacuum by an Edwards E09K (2800 l/s) diffusion pump backed by an Alcatel OME 40S rotary vane pump. To separate the collision chamber from the interaction chamber, an electroplated skimmer with a diameter of 1.2mm is used. Due to its cone-like shape, this fragile piece of equipment is preferable to a regular aperture because it easily deflects stray molecules and creates a forward focused beam of thymine entering the collision chamber. In order to ensure perfect alignment of the oven and the skimmer, a metal brace was designed and mounted to the expansion chamber. This metal brace is designed to ensure that the capillary of the oven will always be aligned to the entrance of the skimmer.

The biomolecular oven is mounted in the center of the expansion chamber and it houses the nucleobase that is used in the experiment. The oven consists of two parts, a copper cavity which is heated by a coaxial heating wire that is wound around the oven and a copper cover that contains an aperture where the thymine exits the oven. The temperature of the oven is generated by a 0.9 A current which is sent through the heating wire and is set by the user via an external temperature controller. Once the current is turned on, a constant stream of thymine is generated at 180 ^{o}C. To hold the oven safely in place, it is mounted on a macor plate which in turn is then attached to a hollow teflon cylinder designed to fit perfectly into the metal brace. The temperature inside the oven is measured using a thermocouple that is placed in a small hole in the copper cavity.

One of the most important aspects of the oven design was its orientation. To ensure correct alignment, the copper oven is mounted off-center on a macor plate, such that the capillary which is also off center in the oven is now centered in front of the skimmer (see figure 3.3). The difficulties of putting the oven pack into the chamber are reduced significantly thanks to design of the metal brace and the Teflon cylinder. The oven capillary will always be aligned with the skimmer regardless of how the user inserts it into the metal brace. Thymine is hydroscopic, so to remove the excess water content the oven is heated to around 100 ^{o}C. Once the pressure in the expansion chamber has dropped to approximately 1 x 10^{-7} mbarr, the oven temperature is then increased to around 180 ^{o}C, which allows the thymine to evaporate from the oven. Shown in figure 3.3 and 3.4 are the schematic of the oven, the skimmer and their mounting. Figure 3.5 is a picture of oven with thymine in powder form. The coaxial heating wire around the oven and the oven capillary are also visible.

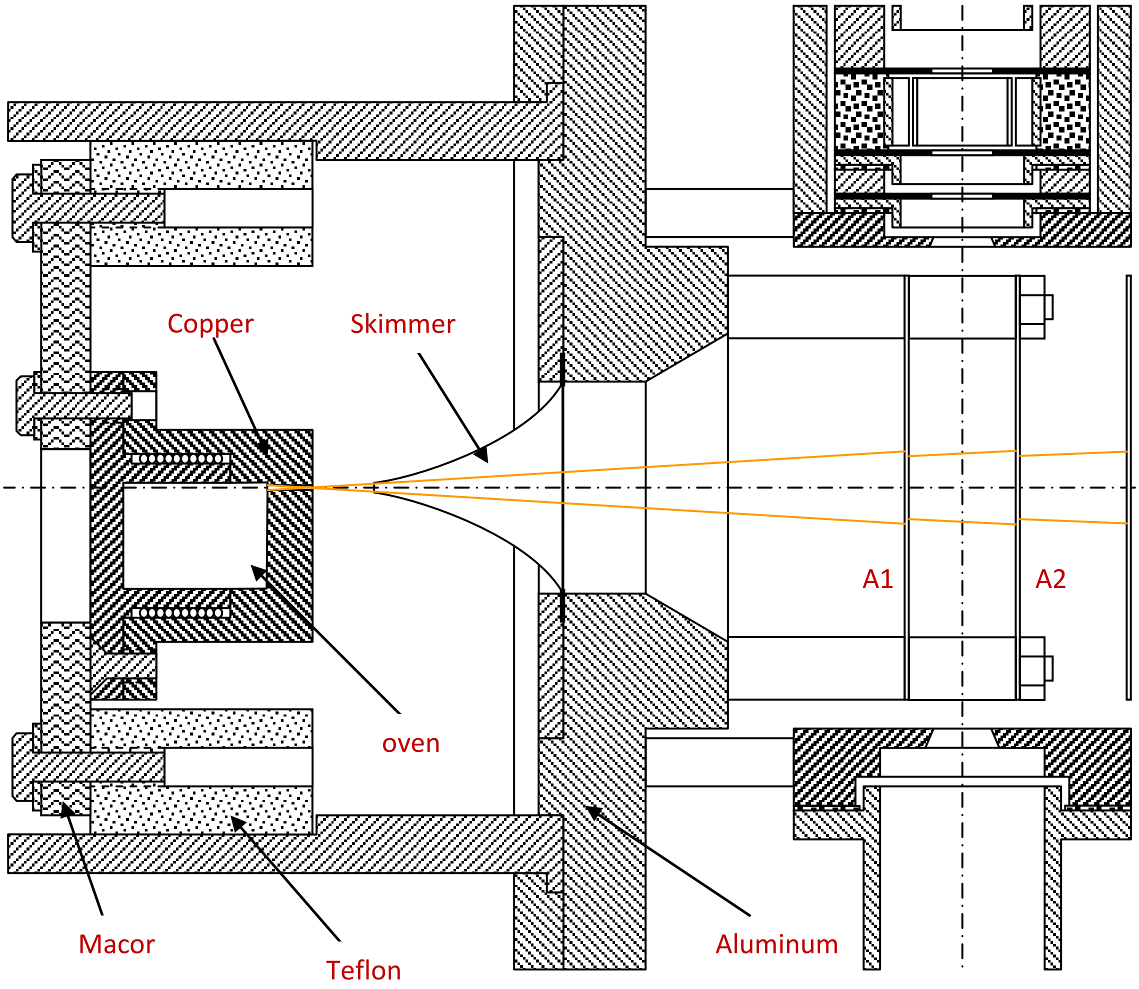

Figure 3.3. Schematic of the oven and skimmer

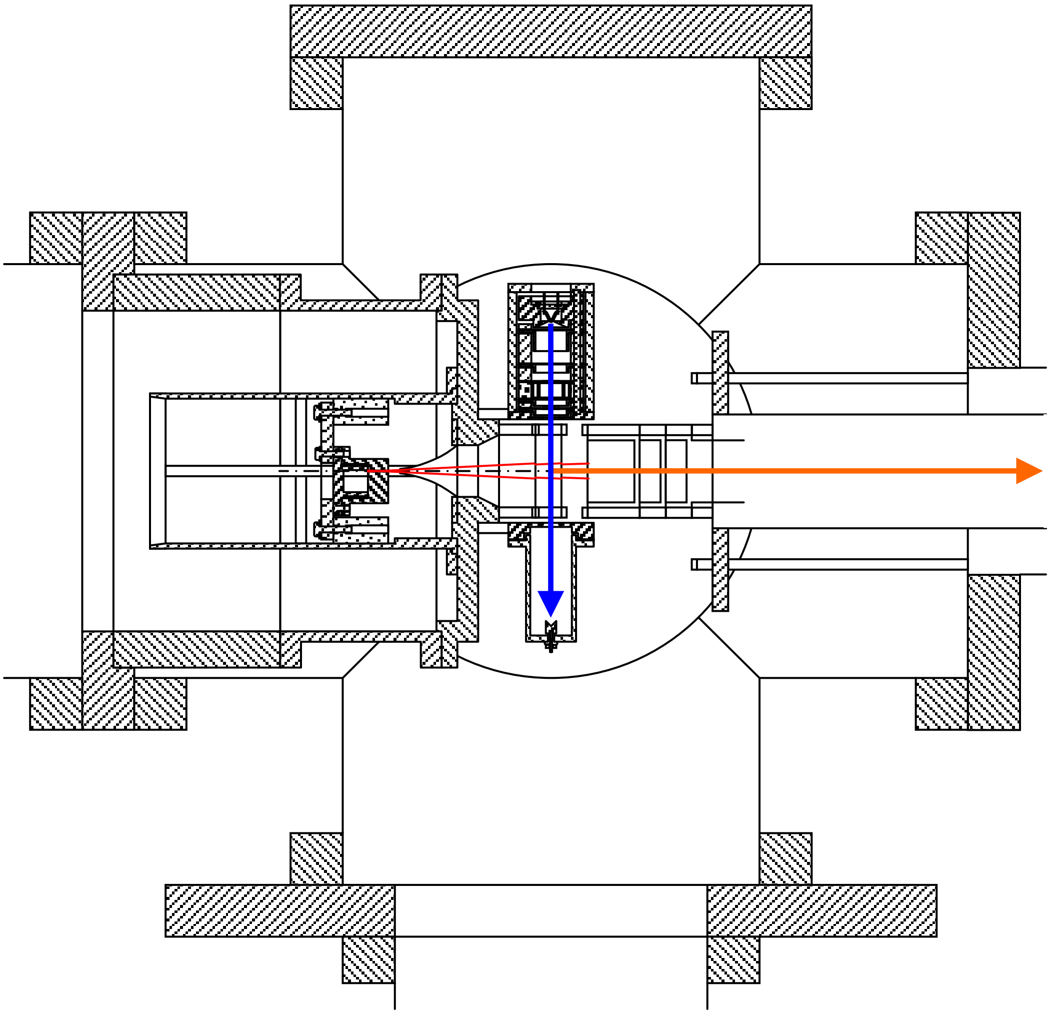

Figure 3.4. Mounting of the oven, skimmer and electron gun on the top hat extending into the collision chamber. To the right of the electron gun are the einzel lens and deflection plates which form the entrance to the RTOFMS.

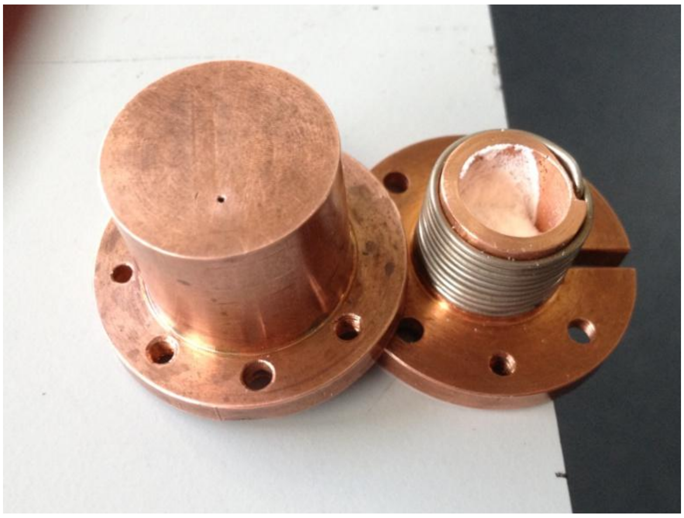

Figure 3.5. The oven with thymine powder. The coaxial heating wire and the oven capillary are visible.

3.3 The collision chamber

The second vacuum tank is called the collision chamber. The chamber is held under pressures of 1.7 x 10^{-8} mbarr by a Leybold Turbovac 361 turbomolecular pump backed by a Trivac D25B rotary vane pump. Here the molecular beam from the expansion chamber interacts with a beam of electrons that are created using an electron gun. The electron gun is mounted on a top hat arrangement 90 degrees to the molecular beam. The area where the molecular beam and the electron beam interact is called the interaction region. This region is situated between two metal plates A1 and A2 (see figure 3.3). A positive pulsed voltage of 100 V is applied to A1 with a pulsed delay of 1µs after the pulsing of the electron gun to avoid deflection of the electrons. See section 4.3 for more details on pulsing.

3.3.1 The electron gun and Faraday cup

The main piece of apparatus inside the collision chamber is the electron gun. This is used to create a pulsed beam of electrons that interact with the nucleobases, released out of the oven in the expansion chamber. To release the beam of electrons, a hot tungsten filament is supplied with a current of approximately 2A. The electrons are released by thermionic emission from the filament. To accurately focus the beam, four electrode lens elements called V1, V2, V3 and V6 were incorporated into the electron gun design. By varying the voltage at each lens, the user can adapt the focus of the beam. To allow for increased accuracy of the beam, four deflection plates X1, X2, Y1 and Y2 mounted in lens element V3 allow the electron beam to be steered. All lens elements are made from aluminium and teflon spacers are used to insulate each lens from each other. All inside surfaces of the lens elements are coated with Aquadag to help maintain the stability of the electric fields as a function of time.

The gun is also comprised of a grid electrode which is made from stainless steel. The purpose of this is to set up a weak electric field that suppresses the initial spreading of the beam being created by the filament. To achieve this, the grid is biased slightly negative with respect to the filament by an external power supply. The gun also has a filament holder which labelled grid in figure 3.7. The filament is mounted such that the tip is centered in the hole of the grid element.

To see the collimation of the electron beam, the beam is passed from the gun into the Faraday cup. The Faraday cup is made up of two separate parts, the inner cup and the outer cup. The inner cup is held at +40 V and the other cup is held at +10 V. To get a good collimation of the electron beam, the current must be minimised on the outer Faraday cup and maximised on the inner Faraday cup. Shown in figure 3.6 is the electron gun and Faraday cup setup in the Maynooth experiment. Figure 3.7 shows the schematic of the electron gun and Faraday cup.

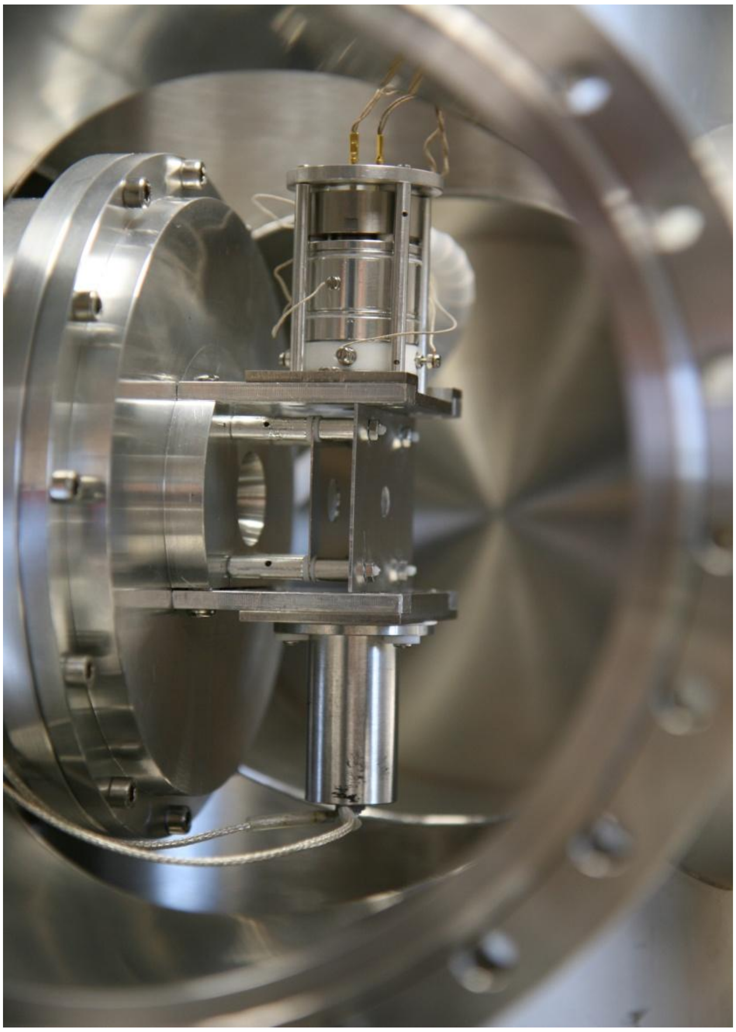

Figure 3.6. Electron gun and Faraday cup setup mounted on the top hat. The molecular beam is directed towards the right.

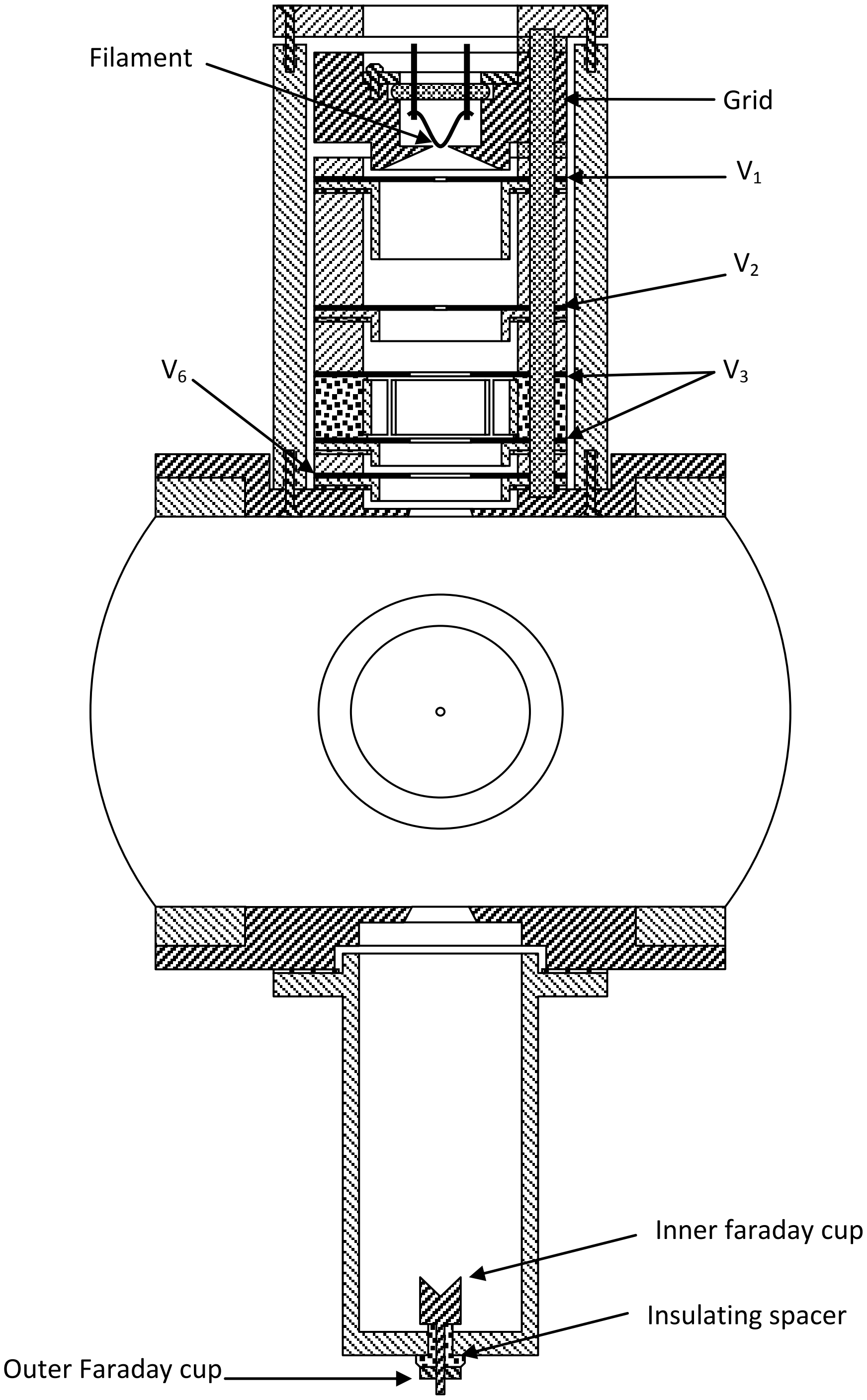

Figure 3.7. Schematic of the electron gun and Faraday cup. The molecular beam is directed out of the paper

3.3.2 Electron gun voltage box

To obtain the desired voltages for the electrode lens elements, an array of potential dividers is used. The array of potential dividers is contained inside the electron gun voltage box. For easy adjustment of the voltages, the potentiometers are mounted on the front panel of the box. The voltages at each element have to be accurately measured, so voltage test points are on the front panel also. This means the voltages can be measured using a digital voltmeter while the electron gun is operational. The voltage box is powered by a Kepco APH 500M power supply (marked 300 V in figure 3.8). This power supply was carefully chosen, because it is a high voltage, low current dc device with a voltage range of 500V but 300V is typically used and a maximum current of 40 mA. The voltage box set-up is shown in figure 3.8. As we can see from the schematic below, the box contains a series of 25 kΩ resistors, 50 kΩ variable resistors and potentiometers. The resistors were carefully chosen because they determine the upper and lower values at which the potentiometers can operate. For the deflection system in the electron gun, the power required is +/-24V DC. This is provided by two EPSD 15/200C AC-DC converters from VxI Power Limited. The two convertors provide + 24 and -24 Volts and require 230 V AC input voltage. The incident electron energy is set with a second Kepco power supply which is used in programmable mode. This marked as $V_{incident}$ in figure 3.8.

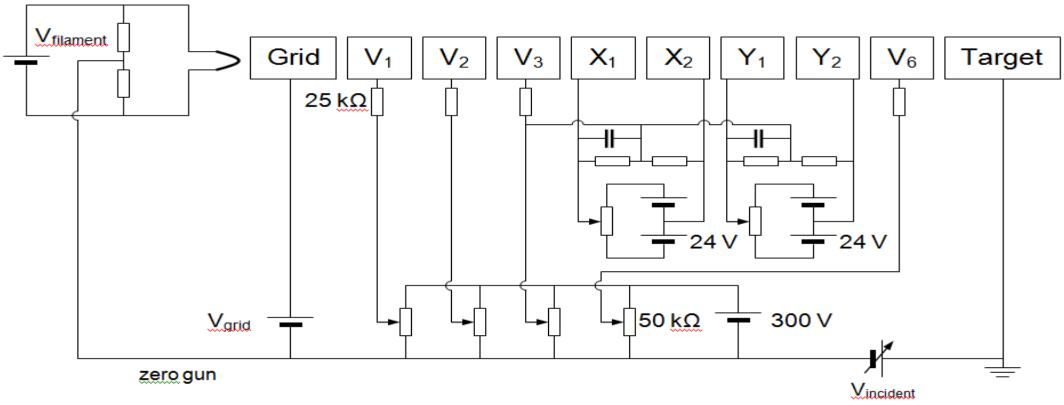

Figure 3.8. Schematic of the voltage box used to apply voltages to the lens elements of the electron gun.

3.4 The reflectron chamber

The principles of a reflectron time-of-flight mass spectrometer (RTOFMS) are discussed in section 2.2. The reflectron used in this project was manufactured by R.M. Jordan Company in California. In the current setup, ions are repelled into the time-of-flight region by the positive pulsing grid A1 shown in figure 3.3, and are then accelerated into the einzel lens. The einzel lens is used for focussing of the ions, and consists of three electrodes whereby the first and third electrodes are held at -1200 V and the middle one is set to -1400 V.

In order for the ions to reach the detector they must be deflected slightly before traversing the flight tube. To achieve this, two deflection plates XY1 and XY2 are used to steer the beam to ensure that ions eventually hit the center of the microchannel plate detector. XY1 is set to -1200 V and XY2 is set to -1140 V. To provide second order focussing of the beam, the voltages used in the reflector are VR1 = -390 V and VR2 = +87 V.

The inside of the RTOFMS has a liner which is kept at a potential of -1200 V. At the end of their flight path, the ions are detected by a microchannel plate detector (MCP) which is operated at -3800 V. This voltage is divided across a voltage divider network in the MCP detector resulting in V_{D1} = -1672 V, V_{D2} = -912 V and V_{D3} = -180 V. Where V_{D1} is applied to the front of the first plate, V_{D2} is applied to the back of the first plate and also to the front of the second plate, and V_{D3} to the back of the second plate (see figure 3.9). This is to ensure the voltage never exceeds 1000 V across any of the plates. Both plates in the MCP detector are mounted in a chevron arrangement. Shown in figure 3.10 is the MCP detector used in the reflectron chamber to detect the ions. Figure 2.3 in the previous section shows the schematic for the reflectron and MCP detector used in this project.

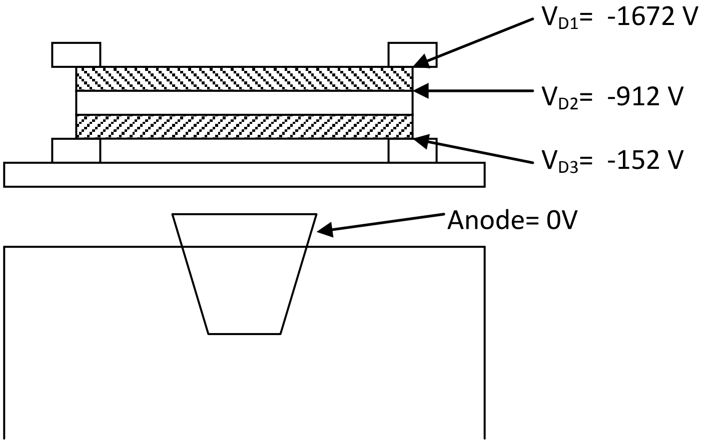

Figure 3.9. Schematic of the MCP detector used in this experiment

Figure 3.10. The MCP detector used in the reflectron chamber to detect the ions

3.5 The interlock system

To ensure the safety of the entire vacuum apparatus, an interlock box is used. This is an integral part in the project because, in the event of a power failure or a equipment malfunction the entire vacuum system including all electronics needs to shut down and not restart. This is extremely important because if the system would restart after a power failure, only the oil sealed rotary vain pumps and the diffusion pump would turn back on. This could cause the pumps to evaporate oil in to the chamber and damage the equipment. To prevent this from happening, all the main equipment and electronics needed for the vacuum system has to be interlocked with each other.

The interlock box incorporates six external trip switches. Each switch can be bypased by toggle switches on the front panel of the interlock box. In order for the interlock box to work effectively, sensors were placed in specific areas of the vaccuum system. While the system is interlocked, if one of the sensors detects a problem, the entire system will shut down and not restart. This process is due to the solid state relay devices inside the box which act as electronic switches. It is because of this, that the experiment can run for very long periods of time without the need for constant observation. The flow of cold water from the chiller into the diffusion pump needs to monitored so, a sensor is placed there. The temperature of the diffusion pump is also monitored with a sensor. To prevent the system pressure from going above a certain level which is set by the user, trip switches were also set on the ion gauges. Trip switches were also used for the two turbopump controllers to ensure the pumps stay off. Monitoring the safety of the turbopumps is extremely important because, in an emergency situation a backdraft of air could cause damage to the blades of the pumps.

When evacuating the system after a restart, all the over-rides must be activated and the start/restart push button pressed. Then, as the pressure, cooling and temperature trip points are safely crossed, the green LED is lit for each trip. When this happens each trip may be safely interlocked by switching the toggle switch from the over-ride into the interlocked position.

CHAPTER 4

Interfacing, data acquisition and data analysis software

4.1 Introduction

This chapter describes the procedures followed to acquire a mass spectrum as a function of electron impact energy and to calibrate the electron gun. The interfacing hardware and the programs needed for data acquisition are described. The main instrument for data acquisition is a FAST ComTEC multichannel scaler which is described in detail in section 4.4. In this experiment, timing is of the utmost importance for the generation and acquisition of the data in this experiment. To acquire a mass spectrum a 3 step sequence needs to occur. Immediately after the electron gun is pulsed, the pulsing of the extraction voltage is used to extract the ions out of interaction region, and multichannel scaler (MCS) is triggered. The pulsing and timing sequence of the various elements of the system are set via a digital delay generator described in section 4.2. The operation and calibration of the MCS is described in section 4.3 and the data acquisition and hardware programs used to operate various hardware devices and to record the data from the time-of-flight scans are described in section 4.5.

All of the data acquisition programs are designed in LabVIEW. LabVIEW is a graphical programming language from National Instruments that can be used for the acquisition and recording of data, the control of external electronic devices, and data analysis. LabVIEW is a type of dataflow programming where writing a program requires selecting relevant icons, placing them on a block diagram and wiring them together. There are two panels in each program, the front panel contains the user interface which displays all the relevant input and output data to the user such as controls, graphs and indicators. The second panel is called the block diagram where all the graphical code is written and sent to the front panel. LabVIEW differs from text based coding because the event execution is not in order and the data is passed to the user when it becomes available. The programs used to operate and analyse various parts of this project are explained in detail in section 4.5.

4.2 Amplifier and timing discriminator

When an ion is detected by the microchannel plate detector (MCP) the signal produced must be amplified and discriminated before the data acquisition can occur at the MCS card. The signal from the MCP passes into an ORTEC 9327 1GHz amplifier and timing discriminator. The 9327 is optimized for use with millivolt signals produced by multichannel plate detectors. The amplifier provides a 1 GHz bandwidth to minimise the noise and rise time contributions to timing jitter on detector pulses having widths as narrow as 250 ps FWHM.

The device is designed to handle pulses in the range of 0 to -30 mV. An oscilloscope is not needed to adjust the gain because the device contains an over-range LED that indicates when the pulse amplitudes have exceeded the full-scale limit of the amplifier. To eliminate the noise from the signal, the 9372 contains a discriminator with a discriminator level that is manually adjusted at the front of the device. The detection of a pulse is indicated by a flash of the output LED, however, this could not be used in this experiment because of the noise generated by the pulsing of the ion extraction and the electron gun. Instead the discriminator level was set by taking single mass spectra and monitoring the background signal between the mass peaks.

The noise produced by the pulsing of the ion extraction and the electron gun produces a large amount of spurious counts in the first few bins when the B pulse for the DG535 digital delay generator (see next section) is used as the start pulse of the MCS. For this reason, an ORTEC 416A Gate and Delay Generator was used to delay the B pulse by 1 µs.

4.3 Pulsing and timing

For this project the electron pulse, ion extraction pulse and the trigger for the MCS are created using a DG535 digital delay generator designed by Stanford Research Systems Inc. This is an extremely important device for the project because the electron pulse, ions extraction pulse and the MCS trigger all require the correct width and delay with respect to each other in order for the experimental setup to operate correctly. The DG535 is a very precise delay and pulse generator that provides four precision delays outputs (A, B, C and D) and two independent pulses (AB and CD) with 5 picosecond resolution. Trigger to output jitter is less than 50 picoseconds. Each delay can be set from 0 to 1000 seconds relative to the trigger with 5 picosecond resolution. The two pulse outputs AB and CD and their inverses are defined as pairs of delay outputs. The first delay specifies the leading edge of the pulse, while the second delay defines the trailing edge or pulse width. The pulse shapes can be TTL, ECL, NIM or VAR and the pulse out can be normal or inverted with an impedance of either 50 Ω or high.

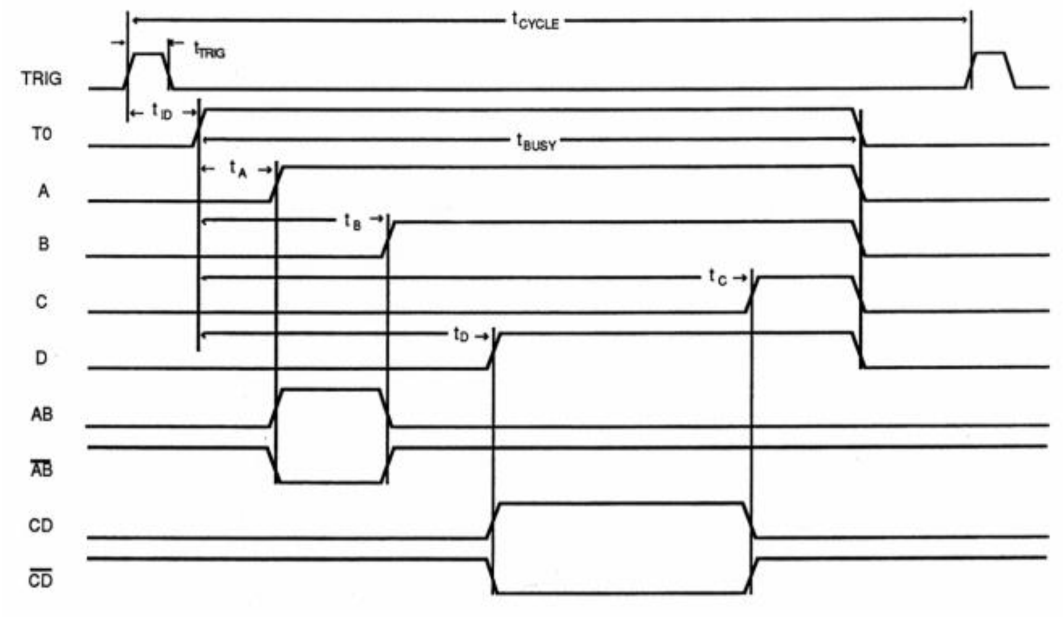

Figure 4.1. Timing cycle of the DG535 digital delay generator [42]

The T0 pulse marks the beginning of a timing cycle and is generated by either the internal rate generator or in response to an external trigger. This output is asserted approximately 85 ns following the trigger. The other outputs A, B, C and D are asserted relative to T0 after their programmed delays. All of the delay outputs return low about 800 ns after the last delay is asserted. The pulse outputs AB and CD go high for the time interval between their corresponding delay channels. [1]

The delays settings used in this project for outputs A, B, C, and D are shown below in table 4.1. For the thymine measurements in this report the repetition rate used was 8 kHz (125 µs between successive pulses) and the time-of-flight range was 62 µs.

A	= T0
B	= D + 1 µs
C	= A + 1 µs
D	= C+ 0.8 µs

Table 4.1. Delay settings used in this project for ouputs A, B, C and D

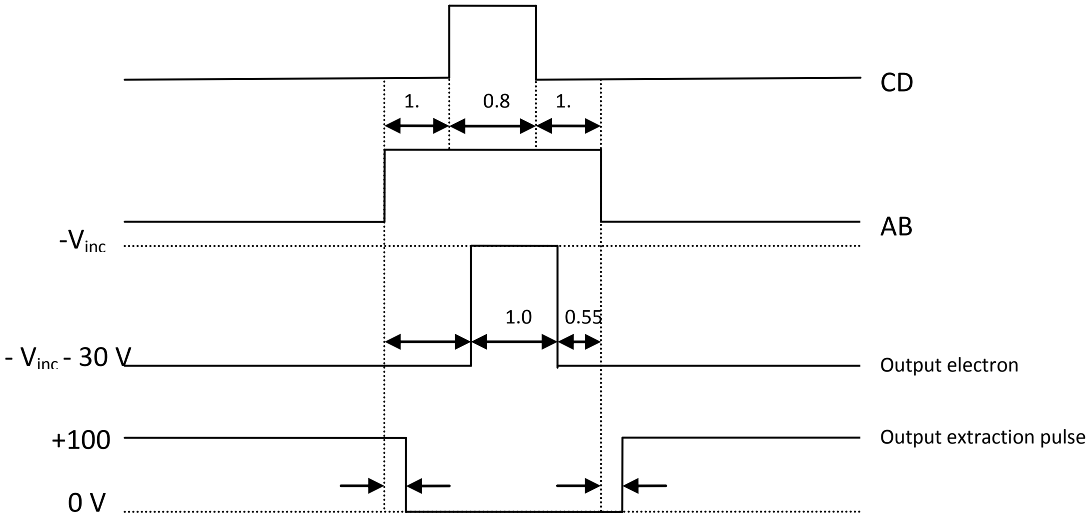

Figure 4.2. Pulse settings used in this project for ouputs AB, CD, Output electron pulse and the Output extraction pulse

Two remote pulsers are used to control the electron pulse and the extraction pulse of the electron gun. Each pulser is connected directly to the appropriate vacuum-feedthrough, and requires 12 V to power its circuit, two dc voltages which specify the low and high voltages of the output pulse, and a TTL trigger pulse which determines the timing of the output pulse. Figure 4.2 shows that both remote pulses have delays between the TTL trigger pulse and the output pulse they provide. The pulse settings used for the remote pulsers are shown in figure 4.2. The AB pulse from the digital delay generator is used to trigger the remote pulser for the ion extraction voltage on the grid. The voltage on the extraction grid must be dropped to ground from +100 V. The CD pulse is used to trigger the remote pulser for the electron gun which pulses from $–V_{inc}$ -30 V to $–V_{inc}$.

4.4 Multichannel Scaler card

The data acquisition for this project is carried out by the 7886S Multichannel scaler card by FAST ComTEC. The card is capable of accepting one event in every channel and can handle up to 2 GHz of peak count rates. It has a dynamic range of up to 2^{37} channels, which enables sweeps for 68.7 seconds with a time resolution of about 500 ps per channel (430 ps for our MCS). [43]

The card is controlled using a server program that contains a set of functions stored in a dynamics link library (DLL). Two of the parameters that can be controlled by the server program are the bin width and the time range. The bin width can be chosen in powers of 2 up to 16,384 channels (each with a dwell time of 430 ps). The range is the length of the spectrum in bins. Most of the thymine mass spectra were recorded with a binwidth of 128 channels (55.0 ns) and a range of 1122 bins (61.8 µs). The user interface software provided by FAST ComTEC is called MCDWIN and this allows the user to control the server settings and display the data in real time. For this project, the MCDWIN user interface has been replaced by LabVIEW programs which provide a more flexible user interface. The LabVIEW programs that interact with the MCS card are described in section 4.5. The MCS card contains a number inputs and outputs: STOP IN, START IN, ABORT IN, SYNC OUT, DIGITAL IN and a THRESHOLD ADJUST screw. Output B of the digital delay generator is delayed by 1 µs and connected to the START IN input and this triggers a sweep of the MCS card. The multichannel plate detector output is connected to the input of the ORTEC 9327. The NIM OUT output of the ORTEC 9327 is connected to the STOP IN of the MCS card , so that the signal from the detector is registered as a count at the relevant binning location of the MCS.

The MCS card utilizes a phase-locked loop (PLL) oscillator that is set to at least 1.8 GHz which results in an assured time resolution of less than 500 ps per channel. This frequency can vary so the time per channel must be calibrated using an external reference. To calibrate the MCS card, the DG535 digital delay generator is used to send a start and stop pulse to the MCS card. The DG535 digital delay generator provides four precisely timed outputs, which can be set with a precision of 5 ps and have a low jitter (50 ps). The LabVIEW program *getspectrum-3-5.vi* described in section 4.5.2 was used for the calibration. The delay in the pulses was varied over 55 µs in steps of 5 µs and then plotted against the corresponding bin number as shown in figure 4.3 below. As in previous calibrations a binwidth of 32 channels was used.

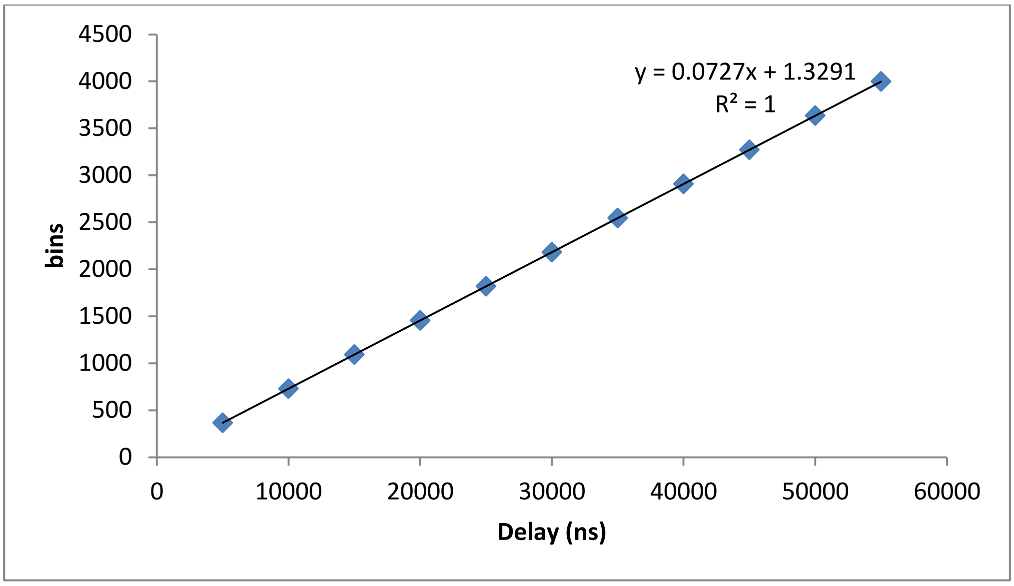

Figure 4.3. Graph to calibrate the MCS card. The delay in the pulses was varied over 55 µs in steps of 5 µs and then plotted against the corresponding bin number.

The best fit line was drawn through these points and the slope was found to be 0.0727 ± 0.0047 bins per ns, yielding a dwell time of 430.0498 ± 0.0020 ps per channel. This is in good agreement with a previous experiment by Jason Howard [44]. For the measurements on thymine a bin width of 128 channels was used, corresponding to 55.04638 ± 0.00026 ns per bin.

4.5 LabVIEW programs

4.5.1 Testing the electron gun

Two previously developed LabVIEW programs are used to set the electron impact energy ($V_{incident}$ in figure 3.8) and to test whether the electron gun produces a beam with a constant current as the electron energy is varied.

A KEPCO APH 500m power supply is used to set the electron impact energy. This is a high voltage 0-500 V, low current and precision-stabilised d-c source. It has an automatic crossover between voltage and current stabilisation mode of operation with visual front panel LED mode indicators. The power supply also has programming terminals on the back panel which are connected to a NI myDAQ data acquisition device.

NI myDAQ is a low-cost portable data acquisition (DAQ) device manufactured by National Instruments that uses NI LabVIEW-based software instruments. There are two analog input channels on NI myDAQ. These channels can be configured either as general-purpose high-impedance differential voltage input or audio input. The device also contains two analog output channels. These channels can be configured as either general-purpose voltage output or audio output. Both channels have a dedicated digital-to-analog converter (DAC), so they can update simultaneously.

To test the KEPCO power supply, a LabView program called *set-gun-V-myDAQ.v*i is used. To control the APH output voltage between 0-500 V, a control potential from 0-5 V must be applied to the input of the main voltage amplifier. The myDAQ can provide a ±10 V but it is important that the applied voltage to the Kepco power supply does not rise above 5 V ± 2%. To ensure this, a limiting function is used in the LabVIEW code to ensure the voltage does not go over 5 V. The code divides the incident voltage by 100 and displays the output voltage on the front panel. A LED indicator is also on the front panel to tell the user if the incident voltage is in range.

To test the operation of the electron gun, a LabVIEW program called *gun-test-myDAQ.vi* is used. This program measures the current from the outer Faraday cup and inner Faraday cup, calculates the total current as function of electron impact energy and displays the data on a graph via the front panel. The myDAQ device is used to set the incident voltage from the Kepco power supply and to acquire the inner Faraday cup current and outer faraday cup current as a function of electron impact energy. On the left hand side of the front panel are four numerical controls where the user can set the start voltage, end voltage, the step size and the delay. There is also an option to save the data in a text file when the program has reached the final voltage. Like the *set-gun-V-myDAQ.vi* program described above, this program displays the output voltage from the myDAQ device to the Kepco power supply, and ensures that the voltage does not go over 5 V. Shown in figure 4.4 is the front panel of gun-test-myDAQ.vi

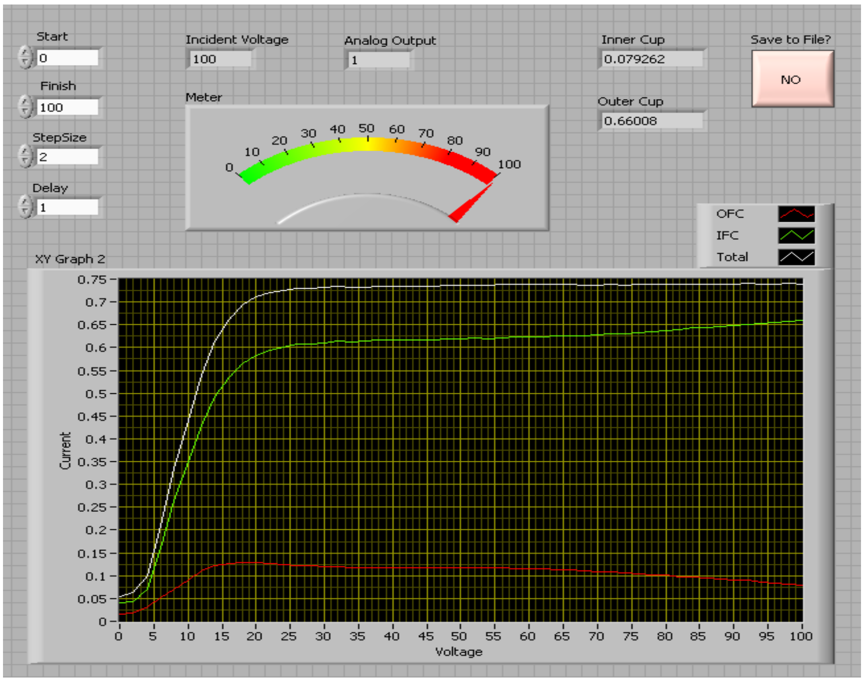
Start: 0
Finish: 100
StepSize: 2
Delay: 1
Incident Voltage: 100
Analog Output: 1
Inner Cup: 0.079262
Outer Cup: 0.66008
Save to File?: NO

Figure 4.4. Front panel of the gun-test-myDAQ.vi program used to test alignment and operation of the electron gun

4.5.2 Acquiring single mass spectra

For the acquisition of single scans of mass spectra, a program called *getspectrum-3-5.vi* is used. The primary use of this program is to acquire a single mass spectrum before doing multiple time-of-flight scans (described in next section). The program records data from the MCS and allows real-time observation of data while it is being acquired and displayed on the graph. In order for LabVIEW to interact with the MCS card, a dynamic link library file (DLL) is needed. For this project, the DLL files were provided by Dr. Marcin Gradziel and are a modified version of the code provided by FAST ComTEC. The DLL files contain C code written for communication with the MCS card and these files are accessed in LabView via the use of the Call Library Function nodes. See appendix for the C code used in the DLL files.

In this program, two different nodes are used. Both DLL's use the same C code but, they access different functions within the code itself. The first node initialises the MCS card and the second one deals with the measurement of the data. The three inputs that the second node reads in are variables *time range*, *update timeout* and *nr of sweeps* which are determined by the user on the front panel. One of the outputs is an array that is initially empty and is added upon with each sweep of the MCS and a complete time of flight spectrum is formed when all the sweeps have been completed. The second output is called *completed sweeps*, which shows the actual number of sweeps the card performed. Before running a scan, the user must decide on the correct time range and bin width by using the corresponding numerical controls on the front panel. Once the user starts the program, it can be stopped at any point and resumed using the continue push button. The save button is used to save the completed spectrum as a text file for further analysis. This program also displays the current state of the MCS card on the front panel so the user can make sure that the MCS card is operating correctly. The control structure used in this program is a standard state machine. The standard state machine is a case structure contained within a while loop. Execution of particular cases in the structure is determined by the output from the previous case by the control selector input. The order of case execution is controlled through the use of a shift register. By wiring the output from one case structure to the next case structure and wiring the input to the case selector from the left hand side shift register, operations can be ordered according to which state is executed. The front panel for *getspectrum-3-5.vi* is shown in figure 4.5. See appendix for the LabVIEW code.

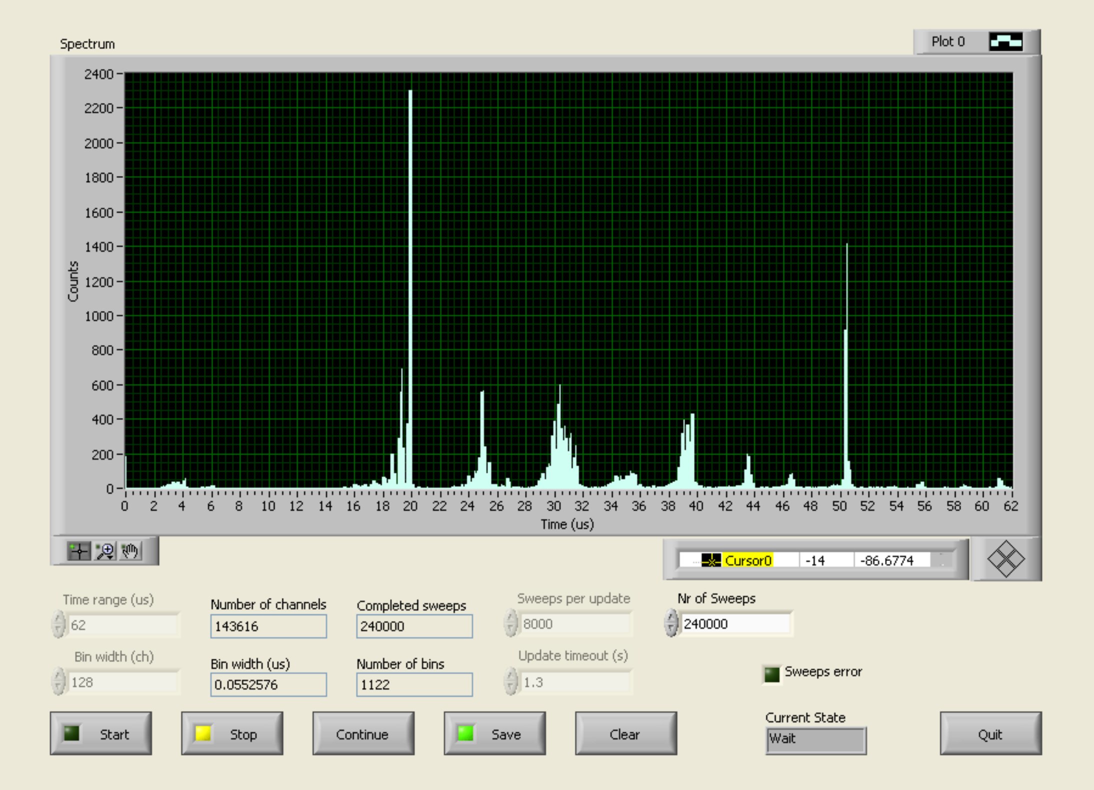

Cursor0 -14 -86.6774

Time range (us) 62

Number of channels 143616

Completed sweeps 240000

Sweeps per update 8000

Nr of Sweeps 240000

Bin width (ch) 128

Bin width (us) 0.0552576

Number of bins 1122

Update timeout (s) 1.3

Current State Wait

Figure 4.5. Front panel of *getspectrum-3-5.vi*. The spectrum shown in the front panel was obtained by 99.7 eV electron impact on cytosine.

4.5.3 Acquiring multiple mass spectra

Spectra-vs-E-v7.vi is the main program used in the acquisition of mass spectra as a function of electron impact energy. This LabVIEW program was developed from a preliminary version coded by Gerard Barrett [45], and also uses the DLL files provided by Dr. Marcin Gradziel (see previous section). This program takes mass spectra sequentially with the electron energy incremented by a step size over a certain range of electron energies. Like the program in the previous section, *Spectra-vs-E-v7.vi* gives the user complete control over the MCS settings via the front panel such as: the range or number of channels (Time range), the number of sweeps per scan (nr of sweeps), and the number of bins per channel (Bin width). The user also has control over the number of cycles, the starting and stopping impact energy and the step size. A cycle is a loop of scans through a certain range of electron impact energy. After the impact energy is increased there is a time delay (Stabilisation) to allow the electron gun to stabilise.

After completion of each cycle, the full 2 dimensional array of accumulated mass spectra as a function of electron energy is written to a file with a name specified by the user and with the cycle number appended to it. This means that after completion of an entire measurement comprising of a number of cycles, the yield of a specific mass at a specific electron energy can be inspected as a function of cycle number, to see whether there was any depletion in the intensity of the thymine beam while the measurements were in progress.

The front panel is shown in figure 4.6 with all the inputs and outputs on display. The user has three options to abort the accumulation of the data. They are finish current cycle, finish current energy or abort TOF accumulation. Choosing the abort TOF accumulation will the program instantly whereas the other two options will wait until the current cycle or energy is finished. The front panel of the program displays each mass spectra being accumulated, and the current cycle number (Cycle), sweep number (sweeps completed), step number (E nr). The four green LED lights above the graph indicate the current state of MCS.

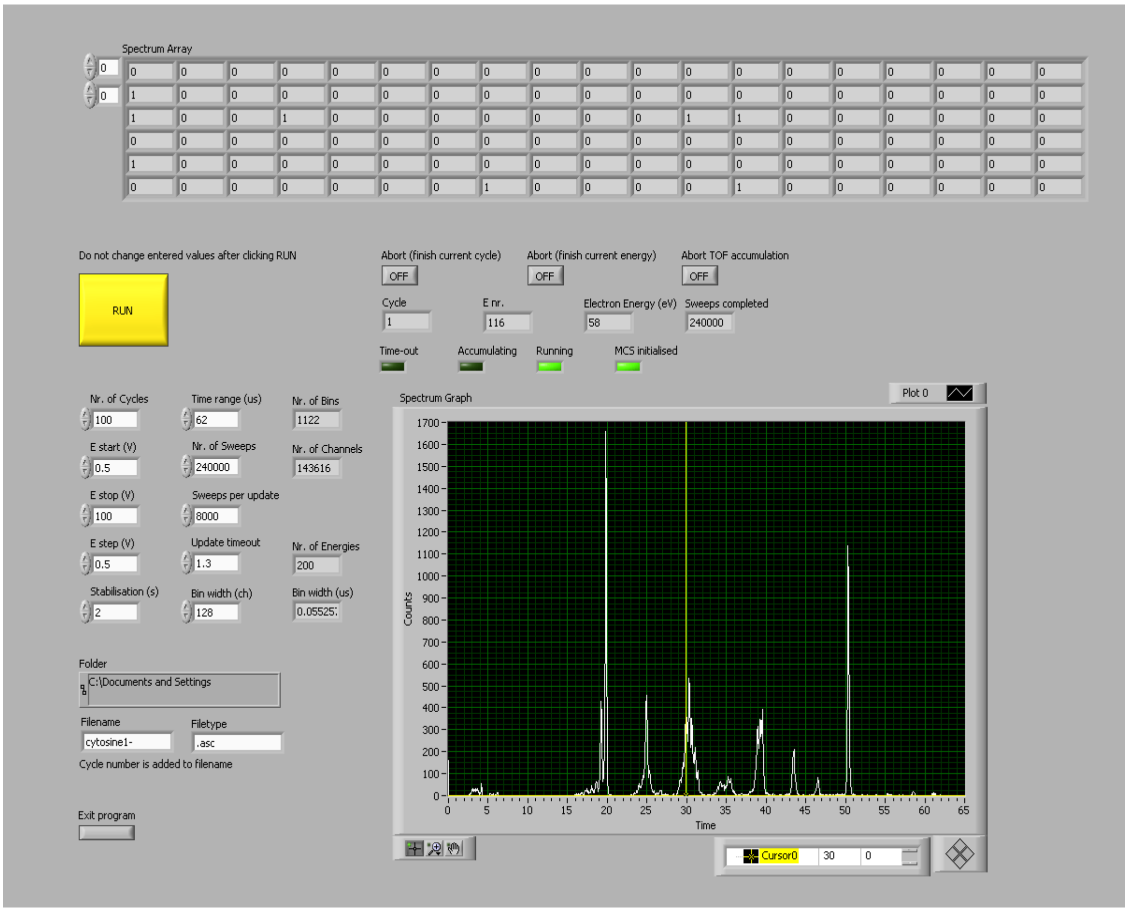

Spectrum Array

0
0

0	0	0	0	0	0	0	0	0	0	0	0	0	0	0	0	0	0	0
1	0	0	0	0	0	0	0	0	0	0	0	0	0	0	0	0	0	0
1	0	0	1	0	0	0	0	0	0	0	1	1	0	0	0	0	0	0
0	0	0	0	0	0	0	0	0	0	0	0	0	0	0	0	0	0	0
1	0	0	0	0	0	0	0	0	0	0	0	0	0	0	0	0	0	0
0	0	0	0	0	0	0	1	0	0	0	0	1	0	0	0	0	0	0

Do not change entered values after clicking RUN

Abort (finish current cycle): OFF
Abort (finish current energy): OFF
Abort TOF accumulation: OFF

Cycle: 1
E nr.: 116
Electron Energy (eV): 58
Sweeps completed: 240000

Nr. of Cycles: 100
Time range (us): 62
Nr. of Bins: 1122
E start (V): 0.5
Nr. of Sweeps: 240000
Nr. of Channels: 143616
E stop (V): 100
Sweeps per update: 8000
E step (V): 0.5
Update timeout: 1.3
Nr. of Energies: 200
Stabilisation (s): 2
Bin width (ch): 128
Bin width (us): 0.05525:

Folder: C:\Documents and Settings
Filename: cytosine1-
Filetype: .asc
Cycle number is added to filename

Cursor0: 30, 0

Figure 4.6. Front panel of *Spectra-vs-E-v7.vi*. The spectra shown is for 58 eV electron impact on cytosine.

4.5.4 Gaussian Peak fitting

To obtain an accurate peak area for all the fragments over a range of 0-99.7 eV, a program called *multigauss test.vi* was created as part of this project. This is an important program for this project because an accurate determination of the peak area of each peak mass is needed for the creation of excitation functions. To fit a series of adjacent mass peaks, the Levenberg-Marquardt algorithm vi is used in the program. The Levenberg-Marquardt algorithm determines the set of parameters that best fit the set of input data points (***x***, *y*) as expressed by a nonlinear function *y* = ***f*(*x*,*a*)**, where *a* is the set of parameters.

The algorithm needs a model function. For this project, each sequence of adjacent peaks was fit using a sequence of normalised Gaussian functions given by:

$$f(x) = \sum_{i=1}^{n} \frac{C_i}{a\sqrt{\pi}} \exp\left(-\left(\frac{x-p_i}{a}\right)^2\right) + b$$

where *C* is peak area, p_i is position of peak *i, a* is the peak width (assumed equal for the adjacent peaks) and *b* is the background.

To insert the Gaussian function into the LabVIEW program, a model string was used. This string allows the user to describe the model equation, define parameters and edit the equation to suit the fit of the data. The model string used for the fitting is shown in figure 4.7. Here the Gaussian function is repeated six times for the peaks c1-c6 and the peak position *p* and peak width *a* are determined by the user on the front panel. Depending on the fit results, *p* and *a* can be either variable or fixed. To ensure the area under the curve is 1, a normalisation factor of $\frac{1}{a\sqrt{\pi}}$ was inserted into the model string. The input data for this program is extracted from the output file of the *Spectra-vs-E-v7.vi* program. The user decides on the bin range to be fitted, copies that range from the output file of the *Spectra-vs-E-v7.vi* program and saves the data as a text file. This program fits the data with bin range on the x-axis and counts collected on the y-axis.

In order to avoid problems with conversion of the fitting while stepping through the data as a function of electron impact, a number of precautions had to be taken. Separate vi's were made for each group of peaks extracted from the full data set. In each vi the model string was changed accordingly. Figure 4.7 shows the model string for the 51 u to 56 u peaks of thymine. It is assumed that the width *a* of all peaks are the same, and that the distances between the peaks are constant. The numbers contained in the model string in figure 4.7 show the distances from the 55 u peak (at position *p*) in units of bins, obtained from the mass calibration described in section 5.3. Based on inspection of the mass spectra, the background was set to 1.

While fitting groups of peaks with decreasing electron energy, it was found in a number of cases that for low energy the fits would not converge any more. In these cases the number of peaks would be reduced if possible, and the width *a* would be fixed to the average value obtained at higher electron energies.

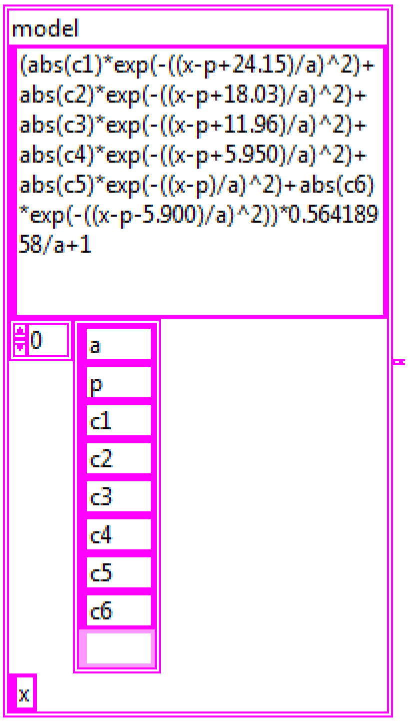

model

```
(abs(c1)*exp(-((x-p+24.15)/a)^2)+
abs(c2)*exp(-((x-p+18.03)/a)^2)+
abs(c3)*exp(-((x-p+11.96)/a)^2)+
abs(c4)*exp(-((x-p+5.950)/a)^2)+
abs(c5)*exp(-((x-p)/a)^2)+abs(c6)
*exp(-((x-p-5.900)/a)^2))*0.564189
58/a+1
```

Figure 4.7. Model string containing the set of normalised gaussians used to fit the 51 u to 56 u peaks of thymine.

The front panel of *multigauss test.vi* is shown below in figure 4.8. The initial parameters array is where the user must input the estimates for the area of each peak, the position of the peak with the highest mass and the peak width. The size of the array will change depending on the number of peaks to be fitted and if *a* and *p* are made constant in the formula string. The best fit parameters array displays the best fit values obtained at each energy, which is then subseqentially stored in an array that contains all the best fit parameters when the program completes the 200 fits. In this project we used 200 fits because we used an energy range of 0-99.7 eV in steps of 0.5 eV. The load push button is used to load the text file containing the peak data into the program. The user can then choose how many rows of data to fit via the *Data Entry Limits: Maximum* and the *Data Entry Limits: Minimum* numerical control. If the user wants to fit the peaks in the 80-99.7 eV range, the maximum value would be 200 and the minimum value would be 160 because our mass spectra was created with 5 eV steps. The program will then load the full text file and only choose the data between the minimum and maximum values.

A time delay was inserted into the front panel in order to slow the fit process so that the fitting process can be inspected. This is an important addition because the program will sometimes fail to fit the peaks at low energies, so slowing the program down to see when this occurs will help decide on the minimum and maximum limits for that data set. The three output arrays, bin number, contents and error at the top of the front panel are used for error checking the data set that needs to be fitted. Shown in table 4.2 are the mass ranges that were fitted using this program and the corresponding bin and the time range for each of the mass groups.

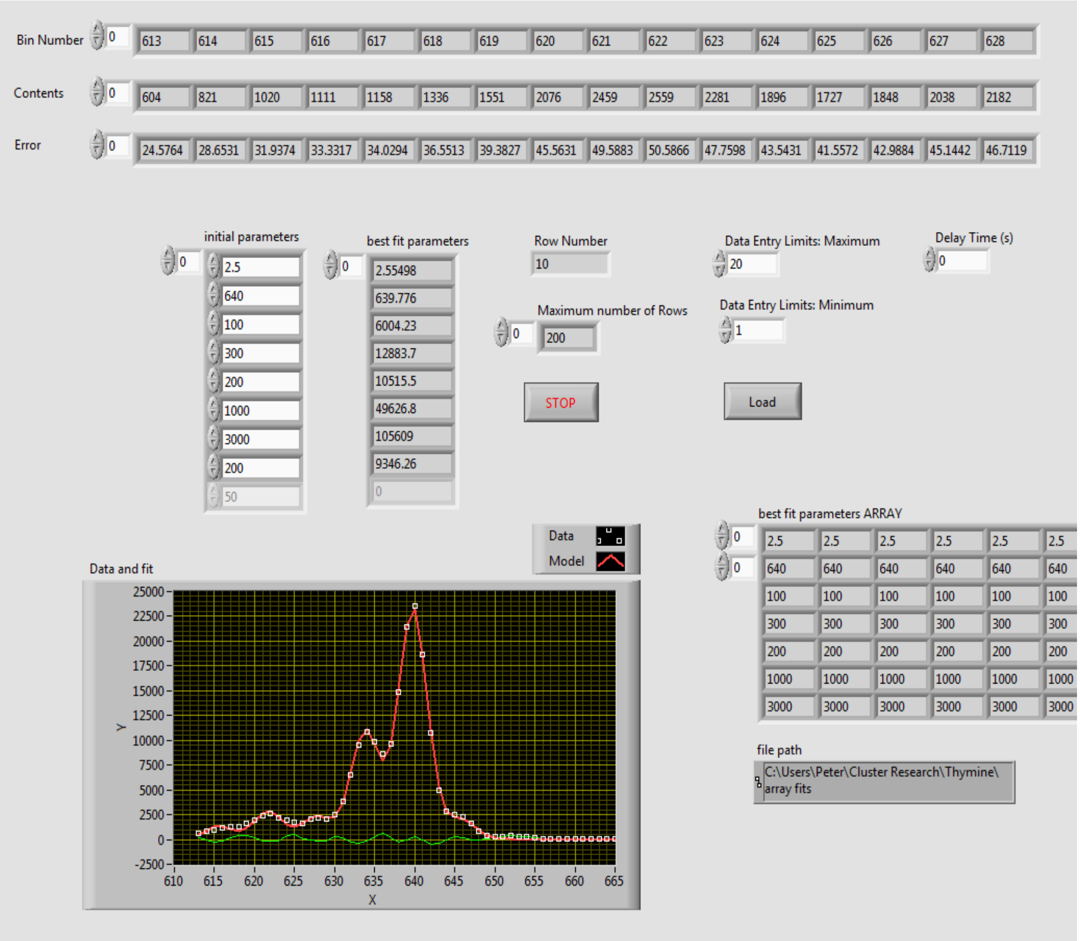

Bin Number	0	613	614	615	616	617	618	619	620	621	622	623	624	625	626	627	628
Contents	0	604	821	1020	1111	1158	1336	1551	2076	2459	2559	2281	1896	1727	1848	2038	2182
Error	0	24.5764	28.6531	31.9374	33.3317	34.0294	36.5513	39.3827	45.5631	49.5883	50.5866	47.7598	43.5431	41.5572	42.9884	45.1442	46.7119

initial parameters	best fit parameters
0	0
2.5	2.55498
640	639.776
100	6004.23
300	12883.7
200	10515.5
1000	49626.8
3000	105609
200	9346.26
50	0

Row Number 10

Maximum number of Rows 0 200

Data Entry Limits: Maximum 20

Data Entry Limits: Minimum 1

Delay Time (s) 0

best fit parameters ARRAY

0	2.5	2.5	2.5	2.5	2.5	2.5
0	640	640	640	640	640	640
	100	100	100	100	100	100
	300	300	300	300	300	300
	200	200	200	200	200	200
	1000	1000	1000	1000	1000	1000
	3000	3000	3000	3000	3000	3000

file path C:\Users\Peter\Cluster Research\Thymine\array fits

Figure 4.8. Front panel of *multigauss test.vi.* The spectrum shows a fit of the 51-56 u peaks of thymine at 90 eV.

u range	bin range	TOF range (us)
16 - 18	335 - 370	18.440 - 20.147
25 - 29	428 - 465	23.559 - 25.376
35 - 46	515 - 583	28.348 - 32.092
51 - 56	613 - 665	33.743 - 36.606
70 - 71	720 - 735	39.633 - 40.459
82 - 84	781 - 798	42.991 - 43.927
97	845 - 862	46.514 - 47.450
124 - 127	963 - 985	53.009 - 54.220

Table 4.2. The thymine mass ranges that were fitted using this program and their corresponding bin and time range

CHAPTER 5

Test measurements with thymine

The purpose of this chapter is to present the various test that were conducted when thymine was in the oven, including the calibration of the electron gun and the mass spectra. An analysis of the water peaks used to convert the incident voltage scale to incident energy scale is also included. During measurements it was found that the intensity of the thymine beam was depleted, and this is also discussed in this chapter.

5.1 Comparison of LabVIEW programs to MCS

To ensure the LabVIEW programs were not missing counts coming from the microchannel plate detector, two tests were carried out with the multichannel scaler card. In the first test the MCDWIN program used to control the MCS card is compared to the LabVIEW program *getspectrum3.5.vi*. Both programs are described in depth in section 4.3 and 4.5. The parameters of the MCDWIN program card were: range of 1024 bins, 4,302,156 sweeps and a bin width of 128. The *getspectrum3.5.vi* parameters were: range of 1122 bins, 5,000,000 sweeps and a bin width of 128. An Excel plot was created from the resulting data files and is shown in figure 5.1. The LabVIEW data points compare well with those of MCDWIN and, only a small multiplication factor (i.e. ratio of number of sweeps) is needed to align the data points in MCDWIN with the LabVIEW data. For the second test, the *getspectrum3.5.vi* program was used twice with adenine instead of thymine, at a pulse rate of 8 kHz and 400 Hz with 720,000 sweeps. The resulting graph is shown in figure 5.2 and both mass spectra are in excellent agreement.

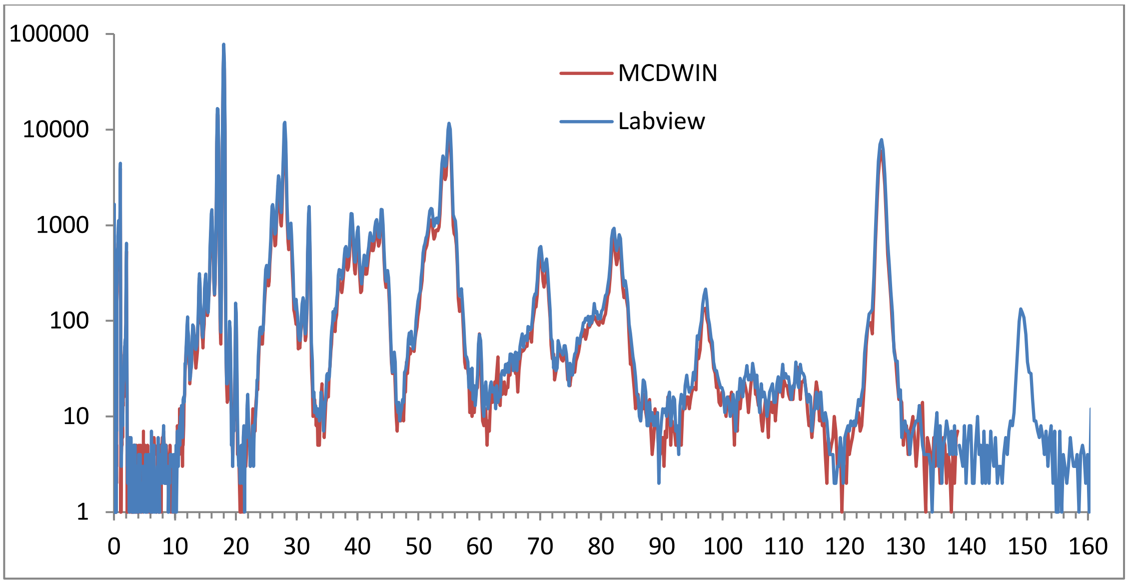

Figure 5.1. Test of MCDWIN and *getspectrum3.5.vi* with thymine

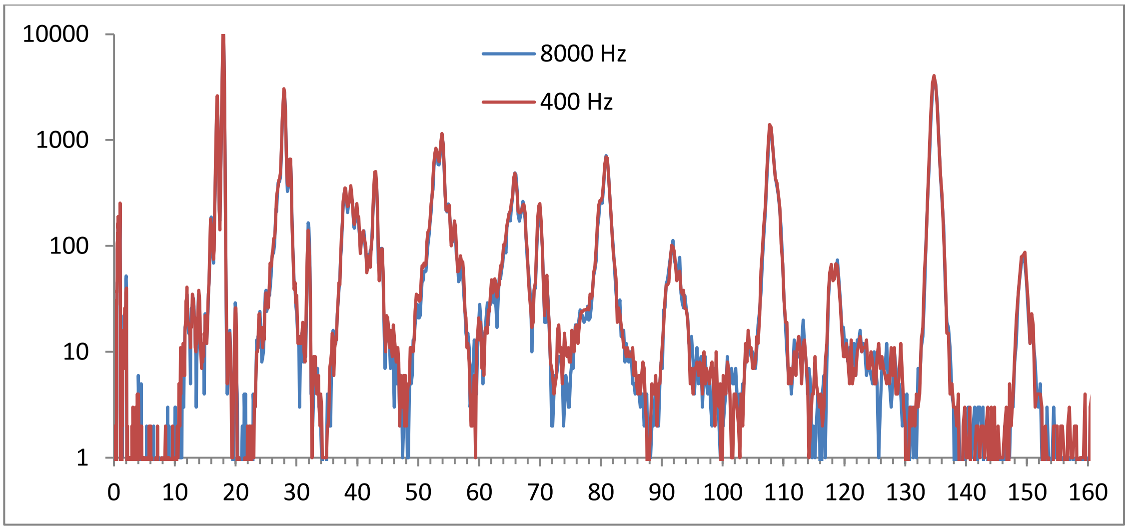

Figure 5.2. Test of *getspectrum3.5.vi* with adenine

5.2 Calibration of Electron Gun

An important test to undertake before taking experimental measurements of excitation functions is to make sure the electron gun has a constant current when the electron energy is changed. To test the electron gun, two LabVIEW programs are used. The first program is *set-gun-V-mydaq.vi* and the purpose of this is to set the acceleration voltage and electron energy of the gun. The second program is called *gun-test-mydaq*.vi, both of these programs are described in detail in section 4.5. Figure 5.3 shows the optimum setting for the electron gun which was found using the gun-test-mydaq.vi program.

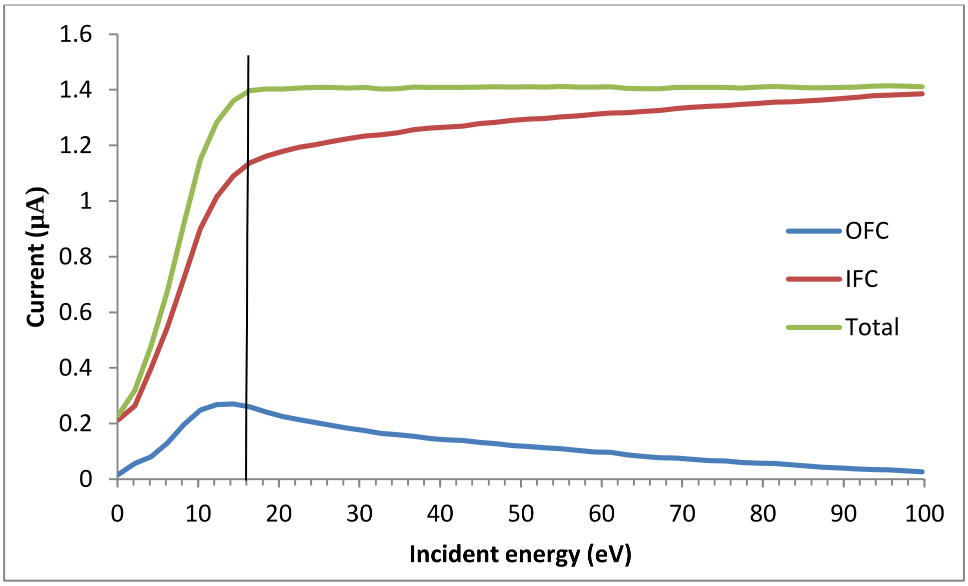

Figure 5.3. Optimum setting for the pulsed electron gun.

Table 5.1 below shows the optimum voltage and current settings for the pulsed electron gun used to take the experimental measurements for this project. The incident voltage scale (V_{inc}) has been converted to incident energy (eV) using the calibration method described in section 5.4. As we can see from the above graph, the electron gun shows constant current down as far as approximately 16 eV after which the current begins to deteriorate. At 9 eV we still get an estimated 60% of current which means we should clearly see the onset of the thymine parent ion peak (126 u) at 8.8 eV. The IFC current was 1.385 µA and the OFC current was 0.026 µA at 99.7 eV.

Setting	**V (pulsed)**
V_{filament}	3.01
I_{filament}	2.246
V_{Grid}	-0.0064
V_1	46.1
V_2	290.6
V_3	84.3
$V_{x1/x2}$	-4.60/4.60
$V_{y1/y2}$	-10.9/10.9
V_6	12.4

Table 5.1. Current and voltage settings used for the electron gun

5.3 Calibration of Mass Spectra

In order to calibrate the mass spectrum for correct analyses, the time of flight scale must first be converted to mass per charge ratio (m/q). To convert the scale we must first find the constants of calibration C and D using the following formula which is described in chapter 2.

$$\frac{m}{q} = (Ct + D)^2 \tag{1}$$

Figure 5.4 shows the thymine mass spectrum at 70 eV with the time scale on the x-axis. Eight prominent peaks in the spectrum were chosen, the square root of their mass was plot against the corresponding time and a straight line was fit to the data as shown in figure 5.5. The value for C was calculated to be 0.206677 ± 0.000027 and D was found to be 0.1388 ± 0.0011.

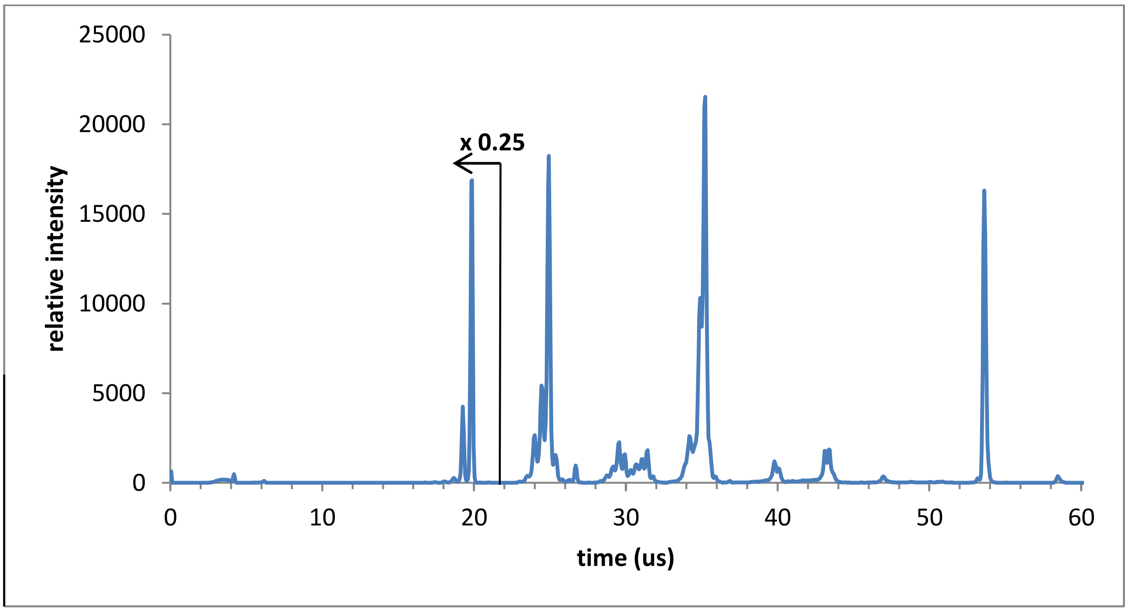

Figure 5.4. Thymine mass spectra at 70 eV with a time of flight scales on the x-axis

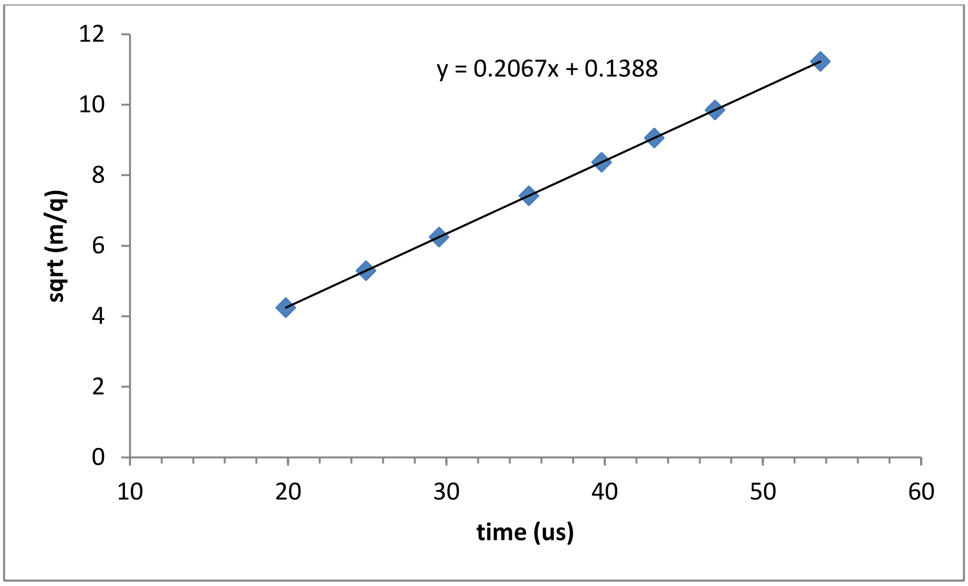

Figure 5.5. Plot to find the calibration constants *C* and *D*

The time scale was converted to mass/charge by using (1) and the constants of calibration *C* and *D*. A plot of *m/q* versus relative intensity is shown in figure 5.6. For a detailed discussion on which fragments are visible, refer to section 1.5.

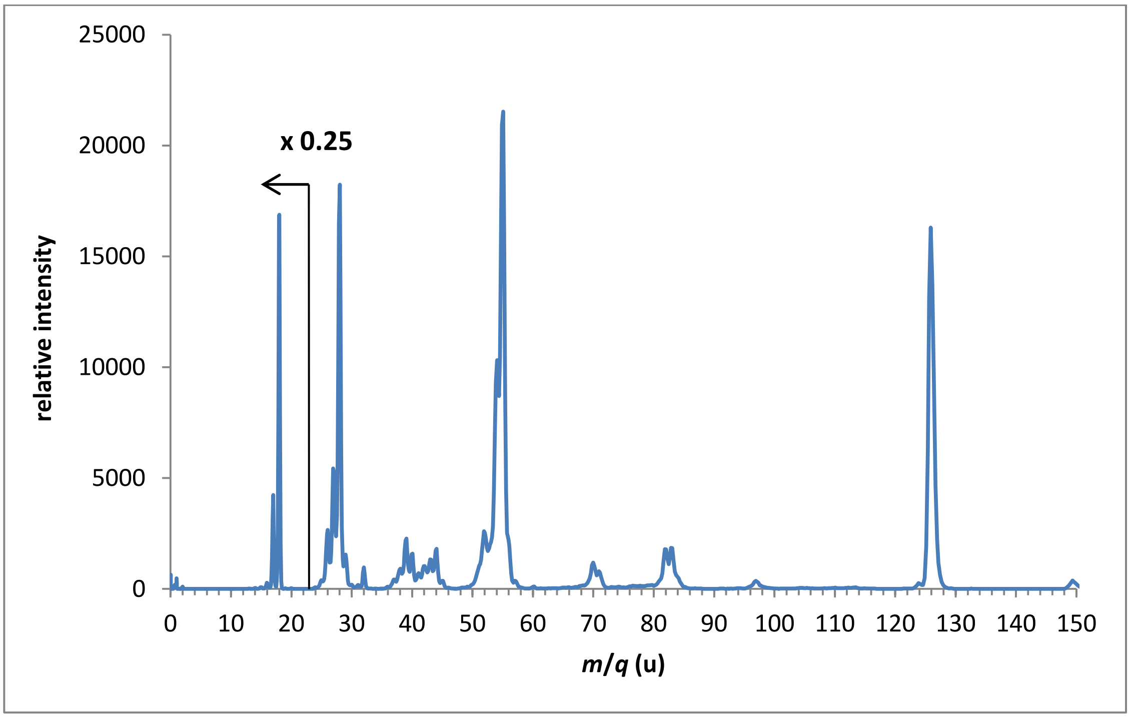

Figure 5.6. Thymine mass spectra at 70 eV with *m/q* on the x-axis

5.4 Analysis of water peaks

For the study of the water peaks obtained in this project, the data presented in the review paper by Y. Itikawa and N. Mason [46] is used for comparison. This paper contains a compilation of all the major cross section data for electron collisions with water molecules. For the ionization cross section of the water molecules, this paper provides the relevant data from Straub *et al* [47] who used a parallel plate apparatus with a time of flight mass spectrometer to obtain the data. The data obtained by Straub *et al* has been slightly corrected by Lindsay and Mangan [48] due to a recalibration of their apparatus.

The excitation functions for the 16 u, 17 u and 18 u water peaks were determined using the peak fitting routine described in section 4.5.4. For each excitation function the onset was determined by drawing a straight line segment through the linear portion of the rising part of the excitation function. Table 5.2 shows the observed onset voltage found for the water peaks compared to onset energy of Itikawa and Mason. The onset voltage here refers to the voltage of the Kepco power supply which determines the electron impact energy (see section 3.3.2).

	Observed onset (V)	Onset I & M (eV)
18 u	16.1	12.621 ± 0.002
17 u	21.6	18.116 ± 0.003
16 u	(21.0)	19 ± 0.2

Table 5.2. Observed onsets for water peaks compared to Itikawa and Mason [46]

This data indicates that in our experiment the incident electron energy is related to the voltage by $E_i = V_i - 3.5$, where E_i is incident energy, V_i is the incident voltage of the band 18 u onsets and the data from Itikawa and Mason. (The 16 u onset deviates somewhat, see discussion below).

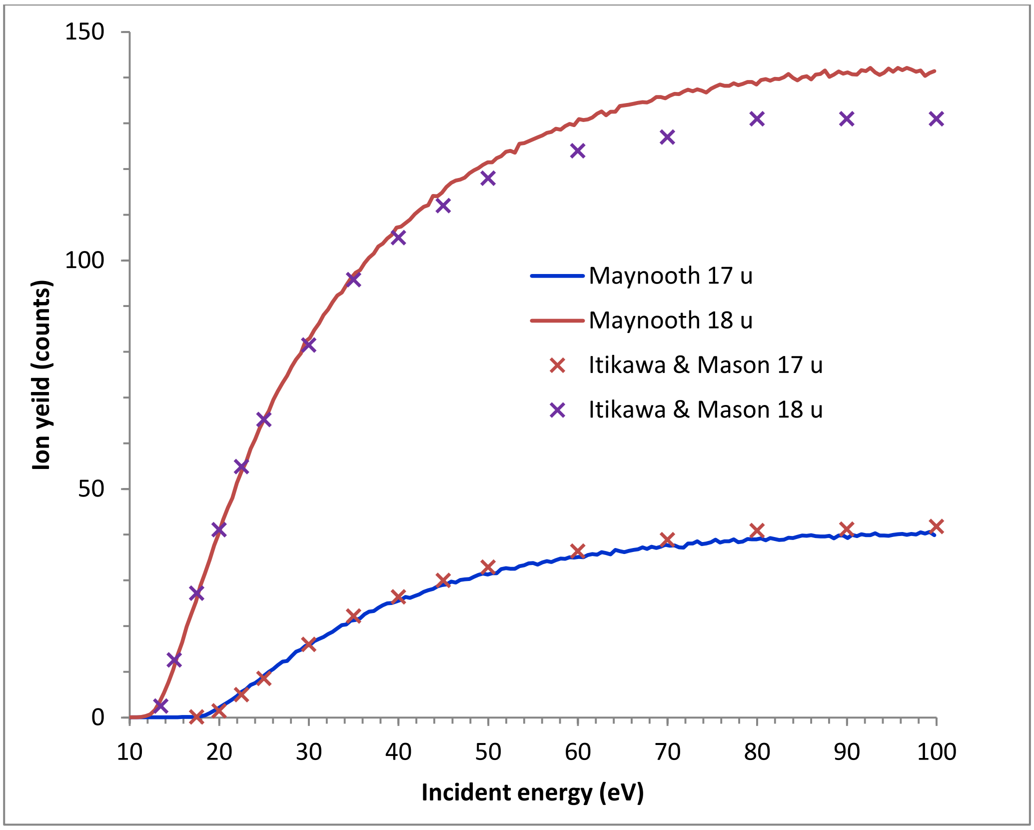

Figure 5.7. Excitation functions of 17 u and 18 u compared to Itikawa & Mason [46]

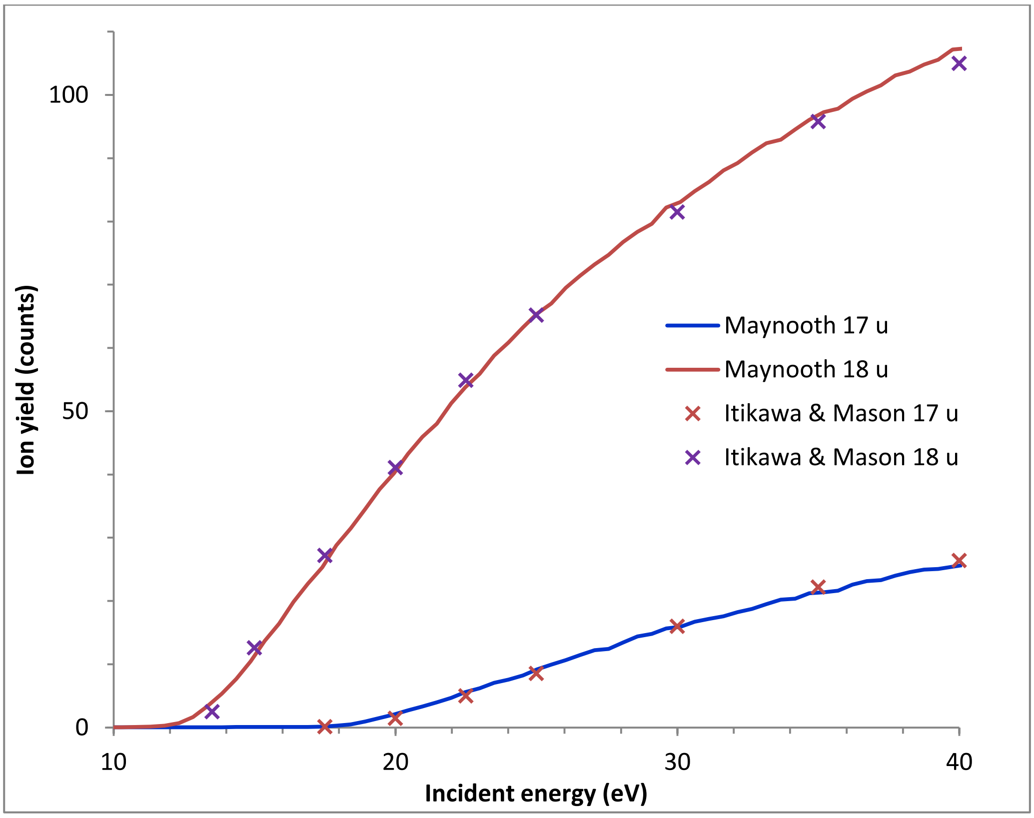

Figure 5.8. Excitation functions for 17 u and 18 u in the range of 10-40 eV.

When this energy calibration was applied to the measured excitation functions, it was found that the shift of –3.5 V was slightly too high, and that a better agreement was obtained by reducing the shift to –3.1 V. The excitation functions obtained using this energy calibration for the horizontal scale are shown in figures 5.7 and 5.8. Both graphs compare the excitation functions for 18 u (H_20^+) and 17 u (OH^+) to the data from Itikawa and Mason. Our experimental data was normalised to the cross sections of Itikawa and Mason at 30 eV.

The 16 u excitation function compares less well with the Itikawa & Mason data and is not shown here. This could be due to contribution from the 16 u fragment of thymine. For this reason, and also because of the 16 u onset from Itikawa & Mason has the largest uncertainty, the average of the differences of our 17 and 18 u onsets with the Itikawa & Mason was taken as the calibration.

The residual water in the Maynooth apparatus could come from two sources in the experiment. If the water is coming from the expansion chamber, the skimmer will prevent the majority of the water molecules from entering the collisions chamber. The most probable explanation is that the water is coming from the walls of the collision chamber so that the water ions will be generated over the entire section between the electron gun and the Faraday cup.

Another possible source of water is the thymine in the oven. Thymine is hydroscopic so there could be water contained in the thymine powder that is released when the oven is heated. This contribution is assumed to be small because no significant depletion was observed in the water peaks while the thymine was depleting (see further discussion in section 5.5.2), and there was no great variation in yield when the oven temperature was increased (see next section).

Assuming that the water is mostly coming from the walls of the vacuum chamber, 16 u, 17 u and 18 u ions would be generated in the section of the electron beam between the exit of the electron gun and the entrance to the Faraday cup. Ions passing through the aperture A2 (see figure 3.3) will enter the RTOFMS, but ions passing near the edge of the aperture may not hit the MCP detector, which could be the reason for the small deviation of the excitation functions from the published cross sections in figure 5.7.

5.5 Oven Tests

5.5.1 Oven temperature

Using the *getspectrum3.5.vi* program described in chapter 4, a test was conducted to verify the temperature needed to generate a steady stream of thymine from the oven. A current of 0.9 A was used to increase the oven temperature to a maximum of 180 ^{o}C. While the oven temperature was increasing, a series of mass spectra were obtained at regular intervals. For each mass spectra shown, the temperature increased by about 2.5 ^{o}C during accumulation until 180 ^{o}C was reached.

The water peaks are somewhat higher than anticipated. There is a presence of the water peaks at lower temperatures and a lack of depletion as the temperature is increased shows that they are largely due to the background. The expansion chamber was heated to about 80 ^{o}C but this did not improve the situation. Heating of the entire vacuum chamber will be implemented in the near future. It is not expected that the presence of water in the vacuum system has had any effect on the mass spectra obtained with thymine. There is no indication of any signal at 144 u due to thymine with a single water molecule attached. Every time after refilling the oven, all efforts were made to ensure the walls of the expansion chamber were clean before closing the chamber by using clean tissues and methanol.

A small amount of remnant air is present in the chamber as is indicated by 32 u peak which is not a thymine fragment (see section 6.1). At 160 ^{o}C, all the main groups of peaks are present including the thymine parent ion at 126u. In the 180 ^{o}C spectrum, all of the peaks are at their highest intensity and a steady stream of thymine is now available. For the duration of the project, the oven was set to 180 ^{o}C. It is noted that the 35 u, 36 u and 38 u peaks are significantly higher for 140 ^{o}C. We are not sure why this is, however our mass spectrum taken at 180 ^{o}C is in good agreement with other measurements, see figure 6.1 in section 6.2.

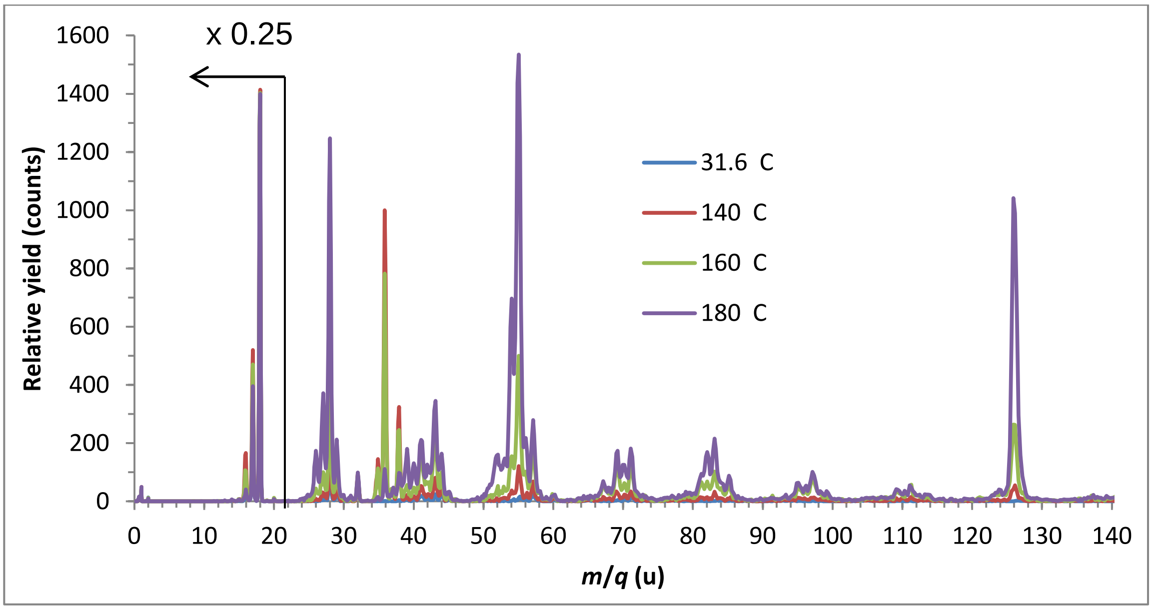

Figure 5.9. Appearance of thymine from the oven as the temperature is increased (at 99.7 eV).

In initial tests, the oven was heated to 100 °C for one or two days but it was realised that this did not reduce the background peaks in the spectra. This also shortened the time over which the thymine beam depleted (see next section). The measurements presented in this report were taken without pre-heating the oven to 100 °C and without heating the expansion chamber.

5.5.2 Oven Depletion

In all measurements on thymine done during the course of this project, it was observed that the intensity of the thymine beam depleted in the course of 6 to 16 hours, even though there was enough thymine left in the oven. There was no indication of blockage of the oven capillary. This depletion was not observed in measurements with other nucleobases.

A test was conducted to see if the oven depletion had an effect on the full spectrum over a range of cycles. For this test, cycle 1, 9 and 17 were chosen and plot of relative intensity versus *m/q* was created and is shown in figure 5.10. For increased accuracy, the relative intensity axis was set to logarithmic scale and we can see that cycle 1, 9 and 17 have excellent agreement with each other.

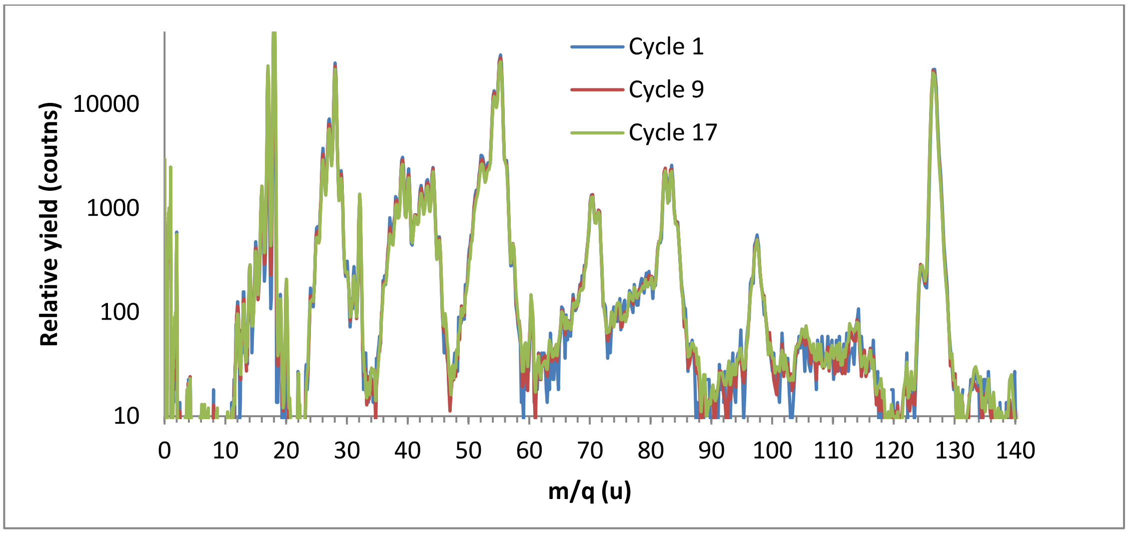

Figure 5.10. Depletion test for cycles 1, 9 and 17

The data that is being analysed in this project was taken over 24 cycles. The signal accumulated after completion of cycle 14 is used for analyses in chapter 6. During the final cycles it became apparent that the source was starting to deplete and it eventually depleted entirely during cycle 24.

A correction factor was developed to correct for the depletion in the data. To create the correction factor it is assumed that the total source density is given by:

$$\rho(t) = s - \frac{d}{T}t \qquad (2)$$

where *s* = initial source density, *d* = depletion of source density over 1 cycle and *t* = time and *T* = duration of one cycle

From eq. (2) table 5.3 was created, containing the source density at the start, end and the cumulative signal at the start and end of cycle 1 to n. From the fit data in Excel we obtain *d*= 253.62 and *s* = 7096.0.

	source density		cumulative signal	
cycle	at start	at end	at start	at end
1	s	s-d	s	s-d
2	s-d	s-2d	2s-d	2s-3d
3	s-2d	s-3d	3s-3d	3s-6d
4	s-3d	s-4d	4s-6d	4s-10d
5	s-4d	s-5d	5s-10d	5s-15d
n	s-nd	s-nd	$ns-\frac{1}{2}(n)(n-1)d$	$ns-\frac{1}{2}(n)(n+1)d$

Table 5.3. The source density at the start, end and the cumulative signal at the start and end of cycle 1 to n

To observe the depletion, the thymine parent ion (126 u) was used. For increased accuracy, the corresponding bins from 124 to 129 u were summed and a graph of cycles 1 to 15 as function of sum of bins were created and a polynomial trendline was included (figure 5.11).

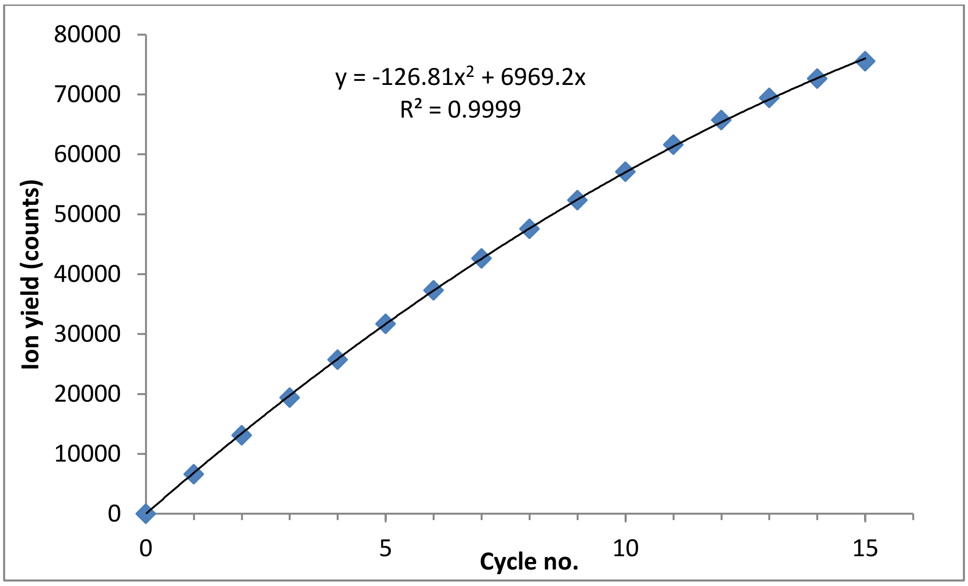

Figure 5.11. Graph of the cumulative yield of the thymine parent ion (see text) as a function of cycle at 99.7 eV, including a polynomial trendline.

At the end of *n* cycles the cumulative signal is (table 5.3):

$$ns - \frac{1}{2}d\,(n^2 + n) = -126.81\,n^2 + 6969.2\,n$$

and by comparison of the fit in figure 5.11 we obtain *d* = 253.62, *s* = 7096.0.

To calculate the correction factor, the cumulative signal at the start and the end after completion of cycle 14 were used. Using the equation in table 5.3 with the values of *d* and *s* for the fit we find that the cumulative signal at the start of cycle 14 is 14*s* - 91*d* = 76266.4 and the cumulative signal at the end of cycle 14 is 14*s* - 105*d* = 72716.0. The ratio of these two numbers is 1.0488. This implies that the correction factor for the excitation functions is 1 at the start at 0.5 V (-1.41 eV) and 1.0488 at the end at 100 V (99.74 eV), and increases linearly with electron impact energy. Figure 5.12 shows the observed depletion in the thymine parent ion over 24 cycles compared to the model equation (2).

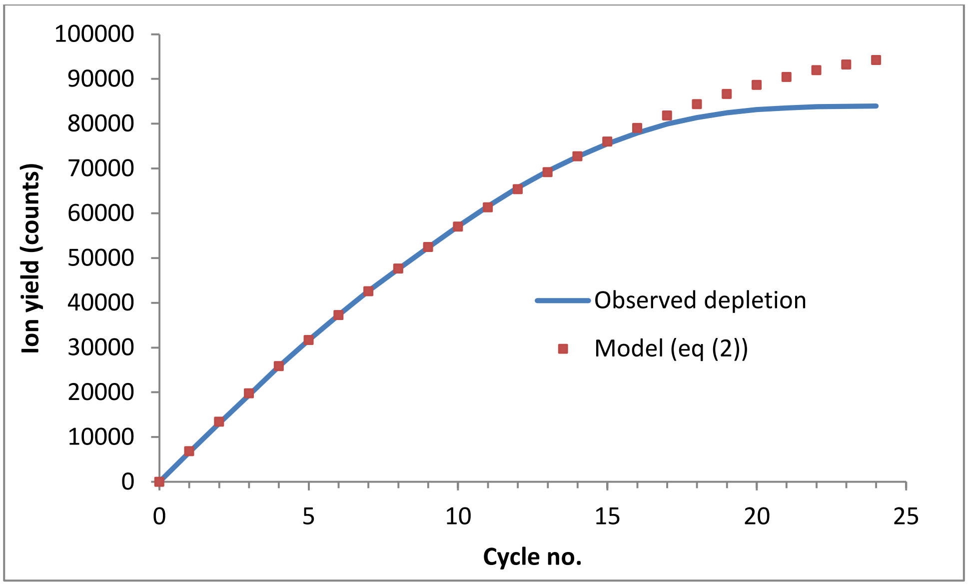

Figure 5.12. A graph of thymine + yield versus cycles compared with model equation (2)

To see the effects of the correction factor on our data, a graph was created comparing the uncorrected excitation functions with the corrected excitation functions for the 126 u peak and the 55 u peak shown in figure 5.13.

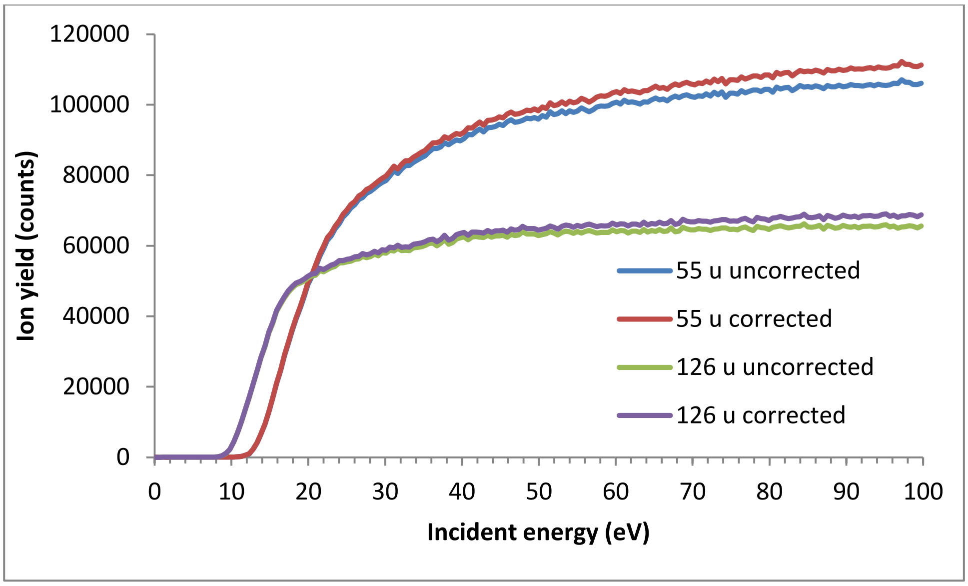

Figure 5.13. Comparison of the uncorrected and corrected excitation functions for the 55 u peak and 126 u peak.

CHAPTER 6

Electron impact fragmentation of thymine

6.1 Introduction

All thymine spectra and excitation functions presented in this chapter have been obtained from a single measurement carried out in December 2012 over nearly 2 days. In this measurement the incident electron energy was varied from -1.41 to 99.7 eV (after calibration) in 0.5 eV steps. As discussed in the previous chapter, 24 cycles were collected, but only the data saved after completion of cycle 14 has been used. This covers a 24 hour data collection period. Because all excitation functions have been generated from this single data set and assuming that the detection efficiency of the RTOFMS is mass independent, the yield of all fragments are on the same relative scale and are comparable. All data have been corrected for the source depletion described in section 5.5.2, and the excitation functions and onsets have been determined in the same way as those for the water features discussed in section 5.4.

Figure 6.1 shows our thymine mass spectrum at 70 eV.

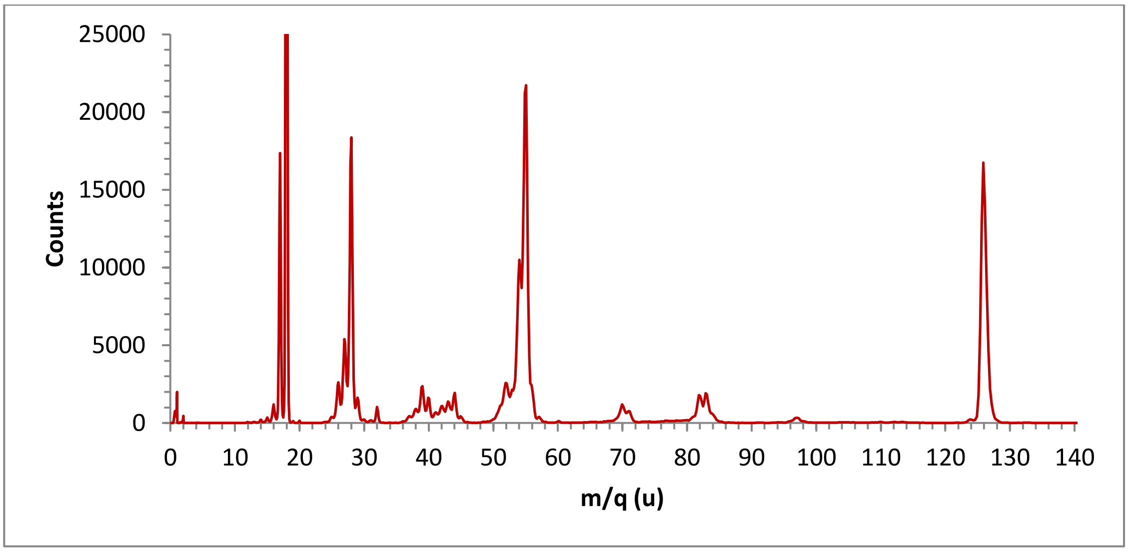

Figure 6.1. Our thymine mass spectrum at 70 eV.

6.2 Relative yield comparison

In figure 6.2, the relative intensities of the peaks (fitted peak areas) in our thymine mass spectrum at 70 eV are compared with those of NIST [49], Rice *et al* [50] and Jochims *et al* [51]. The Rice *et al* data is measured with 70 eV electron impact and the Jochims *et al* data is measured with 20 eV photon impact. In all cases, the 55 u peak has the highest intensity in the spectrum so the intensity of the other peaks in the spectrum were set relative to the 55 u peak. The relative intensity of our peaks agrees quite well with the Rice *et al* and Jochims *et al* data. In all cases except for NIST, the parent ion peak at 126 u is about half the intensity of the 55 u peak. It is not clear what the electron energy is for the NIST data. Comparing the 126 u/ 55 u ratio with our data suggests that the NIST data is for an electron energy of about 20 eV, but at this energy a number of the other peaks in our mass spectrum have a much lower abundance so this energy is incorrect.

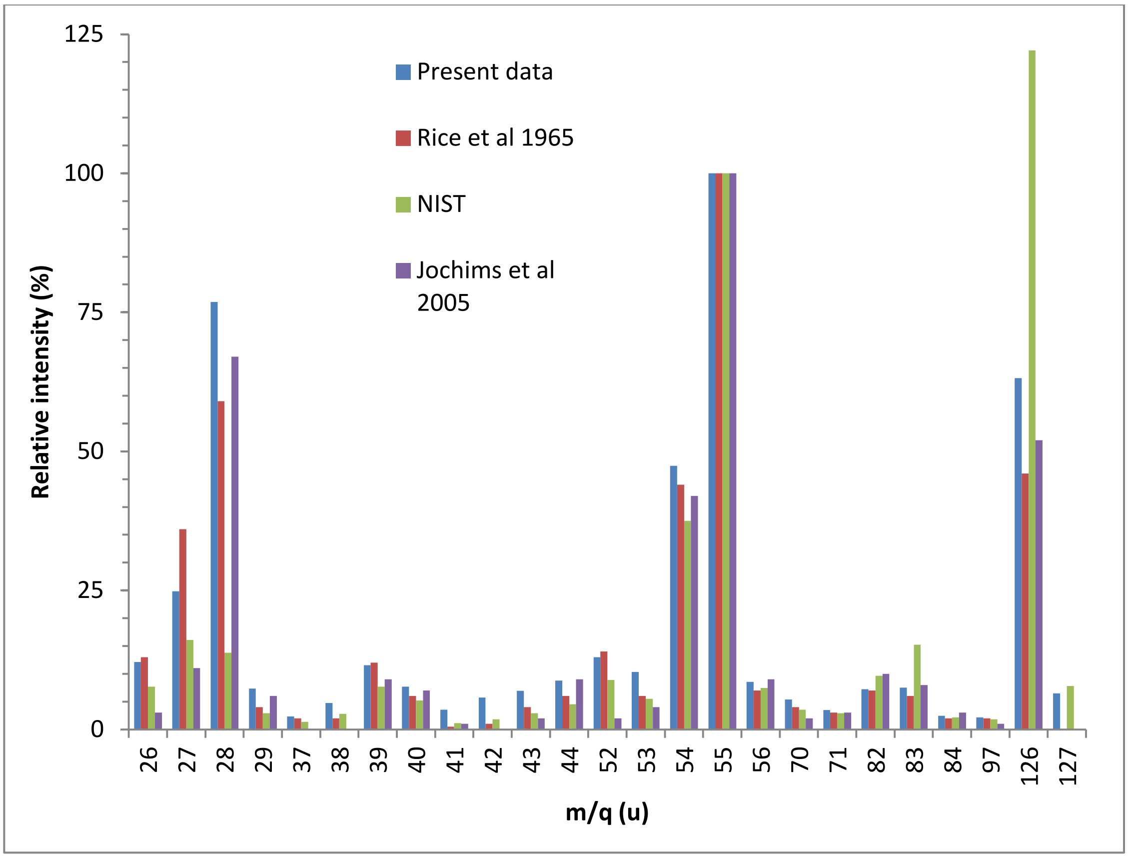

Figure 6.2. Relative intensity of our spectrum at 70 eV compared to NIST [49], Rice *et al* (70 eV electron impact) [50] and Jochims *et al* (20 eV proton impact) [51]

6.3 Identification of the thymine peaks

Shown in table 6.1 are the fragments that were indentified in our spectrum compared to NIST [49], Imhoff *et al* [52] and Jochims *et al* [51] data. The peak assignment for each fragment is also included. (w) in the table denotes a weak fragment in the spectrum (less than 5% of the relative yield of the 55 u peak). From the mass spectrum at 70 eV shown in figure 6.1, the main thymine fragments and their peak assignments have been identified and compared to other results.

The main thymine parent ion at 126 u is clearly visible, and there is a presence of a very weak peak at 127 u due to protonated thymine in the tail of the parent ion. The 127 u peak is also weakly present in the mass spectra presented by Rice *et al* [50] and Imhoff *et al* [52]. The parent ion loses 2H to produce the very weak peak at 124 u ($C_5H_4N_2O_2^+$).

NIST suggest the presence of a group of very weak peaks at 108–111 u but they are not visible in the Maynooth spectrum. This clearly indicates that ionisation accompanied by the loss of a single O atom or loss of the CH_3 group (if it occurs) leads to further fragmentation. The parent ion looses NH_2CN [51] to produce the weak 97 u fragment. NIST suggests the formation of fragments in the 95–97 u range but only the 97 u fragment is clearly visible in the Maynooth data.

Loss of the HCNO group gives rise to the 83 u fragment ($C_4H_5NO^+$) which according to Jochims *et al* [51] is formed via Retro-Diels-Alder (RDA) reaction from the thymine parent cation (see figure 1.5). This reaction involves the rupture of two bonds, N3-C4 and C2-N1 in the parent ion (see figure 1.5). In the Maynooth spectrum, two weak fragments at 82 u ($C_4H_4NO^+$) and 84 u ($C_4H_6NO^+$) were also identified.

In the group 70-73 u identified by NIST, only the fragments at 70 u ($C_2H_2N_2O^+$) and 71 u ($C_2HNO_2^+$) could be identified in our spectrum. Tabet *et al* [53] and Jochims *et al* [51] found the same two fragments in their spectra. The 83 u fragment loses a CO molecule to produce the 55 u ($C_3H_5N^+$) ion. The 55 u fragment is the most abundant peak in our spectra. In the group 50-57 u suggested by NIST, two very strong peaks at 54 u ($C_3H_4N^+$) and 53 u ($C_3H_3N^+$) were also identified alongside the 51 u, 52 u and the 56 u fragments.

All of the fragments in the 40-45 u group were identified in the Maynooth spectra, with the 45 u fragment being particularly weak. All fragments in the 36-39 group were identified in our spectra with the 36 u (C_3^+) being the only weak fragment in the group.

In the 24-30 u group stated by NIST, only the 26 u ($C_2H_2^+$), 27 u ($C_2H_3^+$), 28 u (CH_2N^+), 29 u (COH^+) fragments are present in the our spectrum.

The final group of fragments stated by NIST is the 12-18 u group. Figure 6.1 above shows that the 12-18 u group is very weak in the NIST data. As discussed earlier the 16-18 u peaks are due to water vapour in our vacuum system. Our mass spectra indicate a very weak presence of 12-15 u fragments.

Groups	NIST	Maynooth	Imhoff *et al* [52]	Jochims *et al* [51]	Peak assignments
	electrons	electrons	electron	20 eV photons	
124 - 127	128		128		
	127	127	127		
	126	126	126	126	$C_5H_6N_2O_2^+$
	125		125	125 (w)	$C_5H_5N_2O_2^+$
	124	124 (w)	124		$C_5H_4N_2O_2^+$
108 - 111	111				
	110				
	109				
	108				
95 - 99	99				
	98	(trace)			
	97	97 (w)	97	97 (w)	$C_4H_3NO_2^+$
	96	(trace)			
	95				
80 - 85	85				
	84	84 (w)	84	84 (w)	$C_4H_6NO^+$
	83	83	83	83	$C_4H_5NO^+$
	82	82	82	82	$C_4H_4NO^+$
	81	(trace)	81		
	80		80		
67 - 79	79				
	73				
	72				
	71	71	71	71 (w)	$C_2HNO_2^+$
	70	70	70	70 (w)	$C_2H_2N_2O^+$
	69	(trace)			
	68				
	67				

	NIST	Maynooth	Imhoff *et al*	Jochims *et al*	Peak
50 - 60	60	(trace)			
	57	(trace)			
	56	56	56	56	$C_3H_4O^+$
	55	55	55	55	$C_3H_5N^+$
	54	54	54	54	$C_3H_4N^+$
	53	53	53	53 (w)	$C_3H_3N^+$
	52	52	52	52 (w)	$C_3H_2N^+$
	51	51(w)			C_3HN^+
	50	(trace)			
36 - 45	45	45(w)	45	45 (w)	
	44	44	44	44	CH_2NO^+
	43	43 (w)	43	43 (w)	$CHNO^+$
	42	42 (w)	42		CNO^+, $CN_2H_2^+$
	41	41 (w)	41	41 (w)	$C_2H_3N^+$, CHN_2^+
	40	40	40	40	$C_3H_4^+$, CN_2^+
	39	39	39	39	$C_3H_3^+$
	38	38 (w)	38		$C_3H_2^+$
	37	37 (w)	37		C_3H^+
	36	36 (w)			C_3^+
24 - 30	30	(trace)			
	29	29 (w)	29	29	COH^+
	28	28	28	28	CO^+, CH_2N^+
	27	27	27	27	$C_2H_3^+$
	26	26	26	26 (w)	$C_2H_2^+$
	25	(trace)	25		C_2H^+
	24	(trace)			
12-18	18	n/a	18		H_2O^+
	17	n/a	17		OH^+
	16	n/a	16		CH_4^+, O^+
	15	(trace)	15		CH_3^+, NH^+
	14	(trace)	14		N^+, CH_2^+
	13	(trace)	13		CH^+
	12	(trace)	12		C^+

Table 6.1. Identification of each fragment found in the Maynooth spectrum compared to NIST [49], Imhoff *et al* [52] and Jochims *et al* [51] data. Peak assignments largely based on Imhoff *et al* and Jochims *et al*, are also included in the table.

6.4 Thymine excitation functions

6.4.1 The 26-29 u group.

Figure 6.3 shows the 26-29 u group of peaks from the cycle 14 mass spectrum at 99.7 eV. The excitation functions for this group are shown in figure 6.4. Due to the low yield of the 29 u and 27 u peaks in comparison to the other peaks in the group, a multiplication factor was used. There is a background contribution to the 28 u yield, which is further discussed in section 6.8.

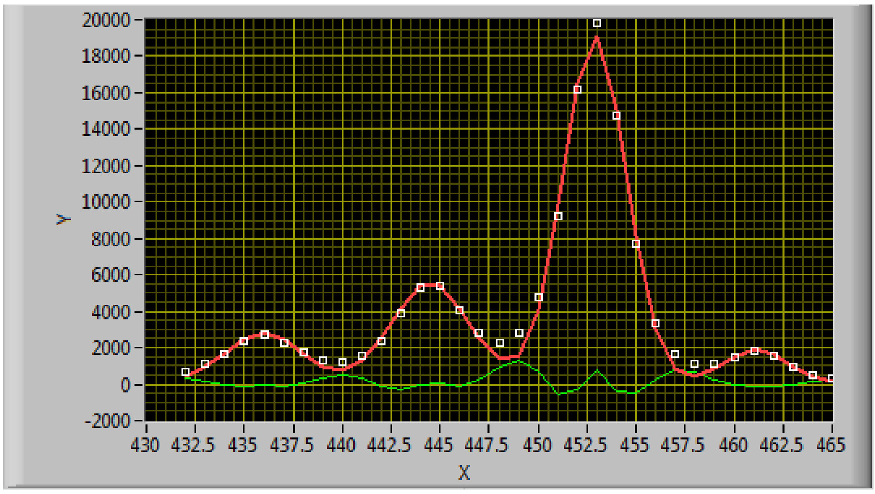

Figure 6.3. The 25-29 u group of peaks and their fits at 99.7 eV electron energy. The green plot represents residuals of the fit for this group and all the following groups in the spectrum.

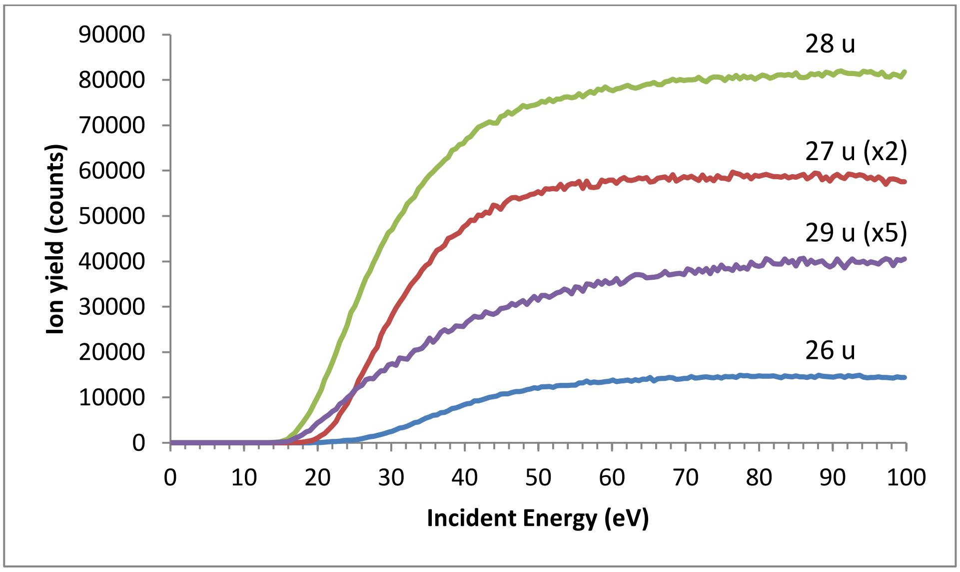

Figure 6.4. Excitation functions of the 25-29 u group.

Due to good convergeanace of the fits at low energies, no fits with a reduced number of peaks were needed. An interesting point to note is all peaks in the group exhibit different excitation shapes with varied appearance energies regardless of peak proximity in the group. The appearance energies of the main peaks will be briefly discussed in section 6.6.

6.4.2 The 36-40 u group.

Figure 6.5 shows the 36-40 u group from the 99.7 eV mass spectrum. This group is part of the bigger 36-45 u group but to ensure accuracy in the fitting this group has been split in two. The excitation functions for 36-40 u group are shown in figure 6.6.

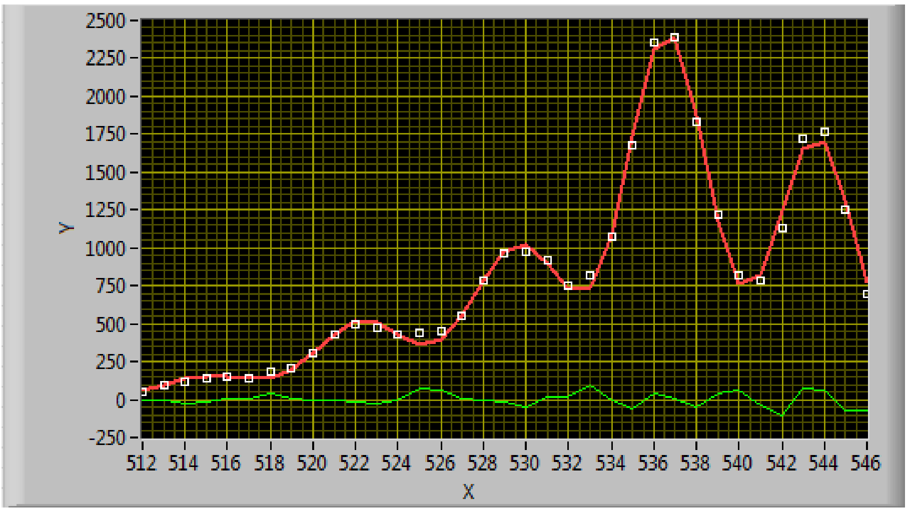

Figure 6.5: The 36-40 u group of peaks and their fits at 99.7 eV electron energy.

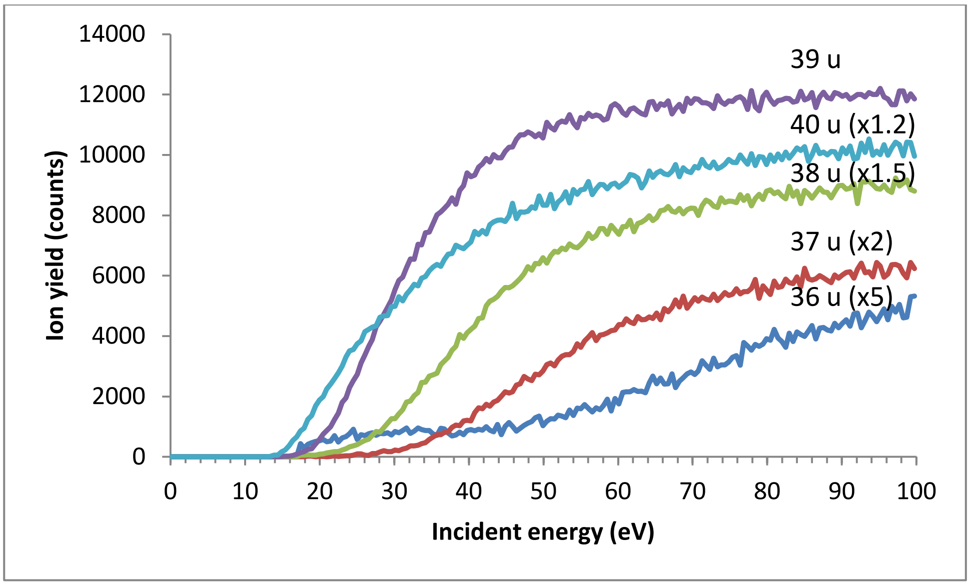

Figure 6.6: Excitation functions of the 36-40 u group.

The excitation functions in this group have a fairly low yield compared to the 25-29 u set of peaks, and the peaks 36 u, 37 u, 38 u, and 40 u have a multiplication factor included in the data. Like the 25-29 u group, the shapes of the excitation functions and appearance energies are different. The excitation function for 36 u and 37 u indicate that additional fragmentation processes contribute to the yields above 55 eV and 33 eV, respectively. In the range of 13.3−16.9 eV only the 39 u and 40 u peaks were fitted with a fixed width (of 2.1 bins) based on fitted widths directly above 16.9 eV.

6.4.3 The 41-45 u group.

Like the 35-40 u group, the 41-45 u group shown in figure 6.7 has a low yield. The excitation functions for this group are shown in figure 6.8. The 43 u and 44 u excitation functions exhibit a similar shape, and the appearance energy of all the peaks is very similar. In the range of 11.8−17.4 eV only the 42, 43, 44 and 45 u peaks were fitted with a variable width.

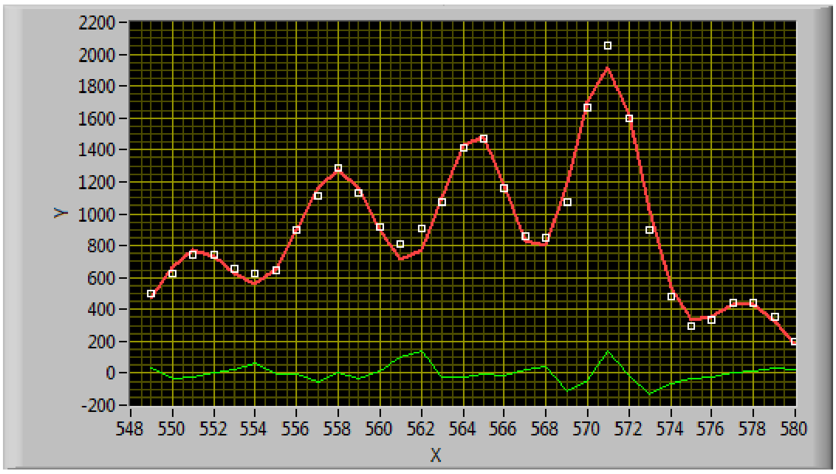

Figure 6.7. The 41-45 u group of peaks and their fits at 99.7 eV electron energy.

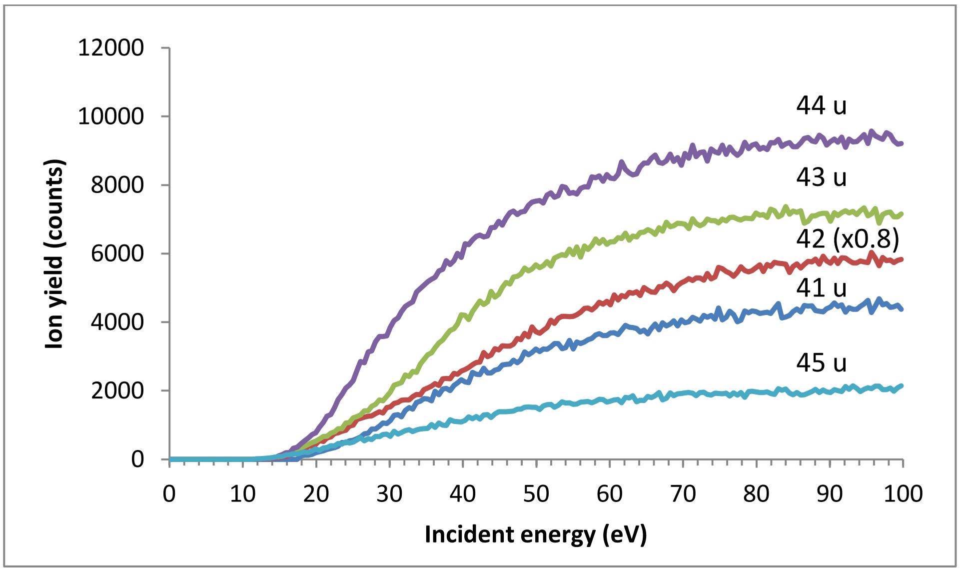

Figure 6.8. Excitation functions of the 41-45 u group.

6.4.4 The 51-56 u group.

The 55 u peak shown in figure 6.9 has the highest yield in our mass spectra. All other peaks in the group have a multiplication factor added to the data for comparison purposes. The 54 u and 55 u excitation functions have similar shapes, but the 55 u excitation function has a lower onset. Below 10.8 eV only the 54 u and 55 u peaks were fitted with a fixed peak width of 2.6 bins based on fitted widths directly above 10.8 eV.

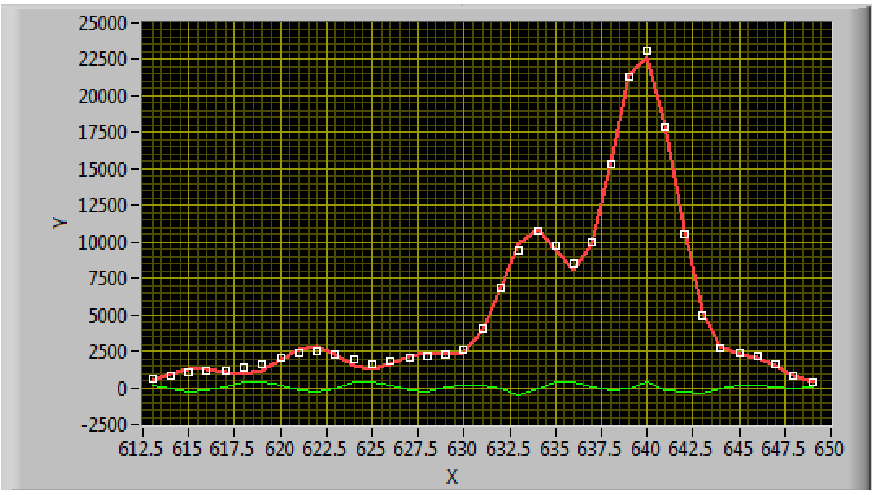

Figure 6.9. The 51-56 u group of peaks and their fits at 99.7 eV electron energy.

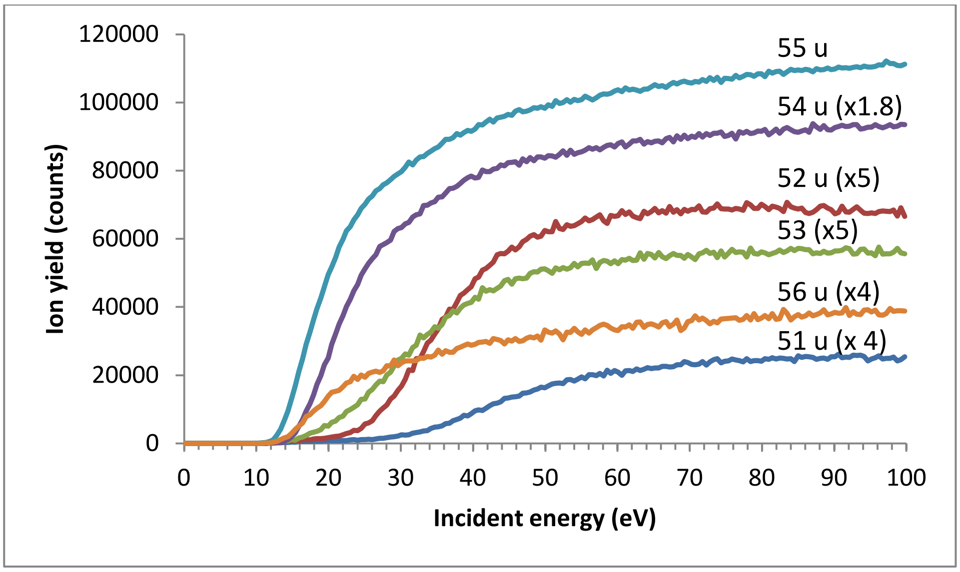

Figure 6.10. Excitation functions of the 51-56 u group.

The excitation functions in figure 6.10 have different appearance energies. The 51 u and 52 u excitation functions indicate that additional fragmentation processes may contribute to the ion yields above about 35 eV and 25 eV, respectively.

6.4.5 The 70-71 u group and the 82-84 u group.

The excitation functions in figure 6.11 and figure 6.12 contain those of the 70-71 u group and the 82-84 u group respectively. The 83 and 84 u excitation functions have similar appearance energies. Both groups of peaks showed good convergence for low electron energies so no fits with a reduced number of peaks were needed.

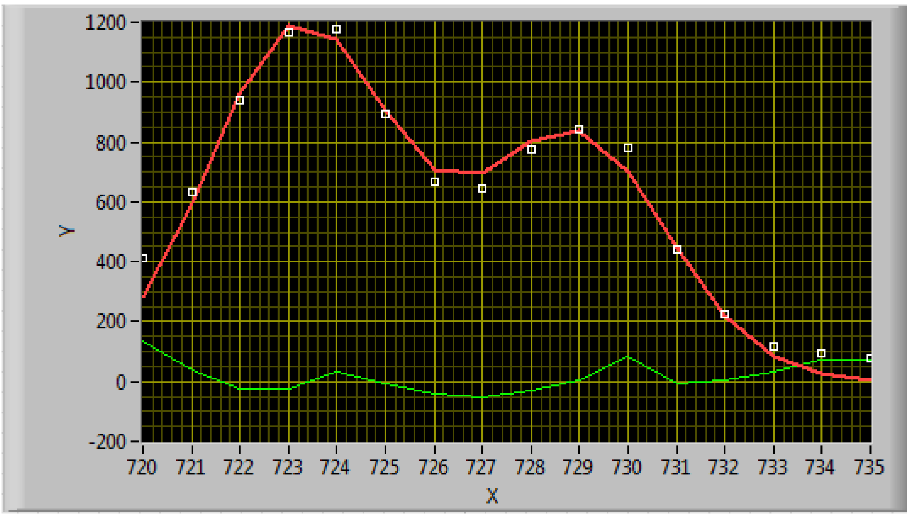

Figure 6.11. The 70-71 u group of peaks and their fits at 99.7 eV electron energy.

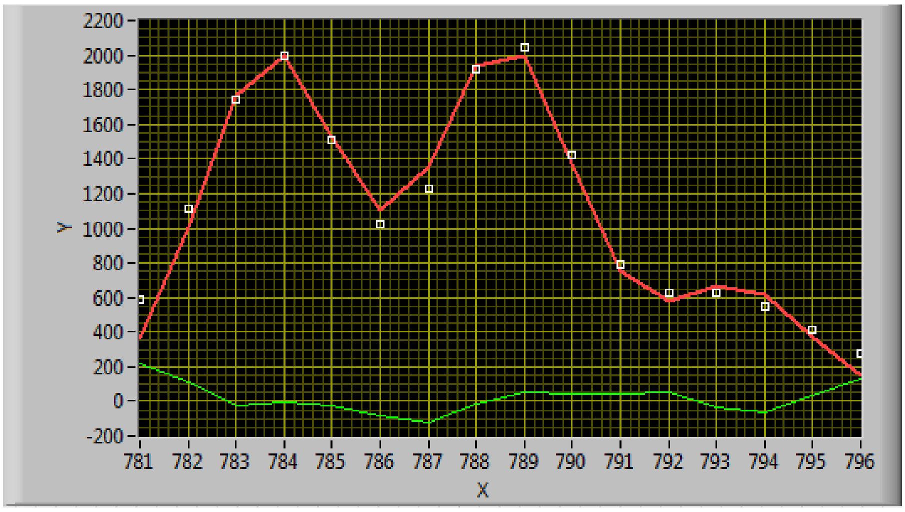

Figure 6.12. The 82-84 u group of peaks and their fits at 99.7 eV electron energy.

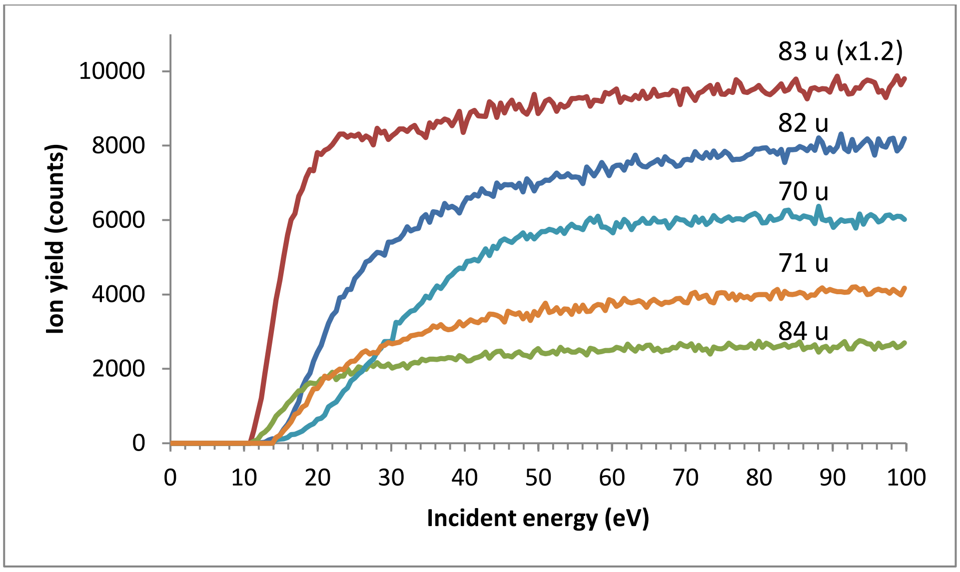

Figure 6.13. Excitation functions of the 70-71 u and the 82-84 u group of peaks.

6.4.6 The 97 u and 124-127 u group.

Figure 6.14 shows the 124-127 u group from the Maynooth mass spectrum. The 124 u and the 127 u peaks have a very low yield in comparison to the thymine parent ion, so a large multiplication factor has been added to these peaks in figure 6.15. The shape of the 127 u excitation function suggests that two processes with different appearance energies (at 10.5 eV and 30 eV) contribute to the formation of protonated thymine. The fits of the 124-127 u group of peaks converged well, but the low yield of the 127 u peak directly adjacent to the high yield 126 u peak may add some uncertainty to the precise shape of the 127 u excitation function. Below 8.8 eV only the 126 u peak was fitted.

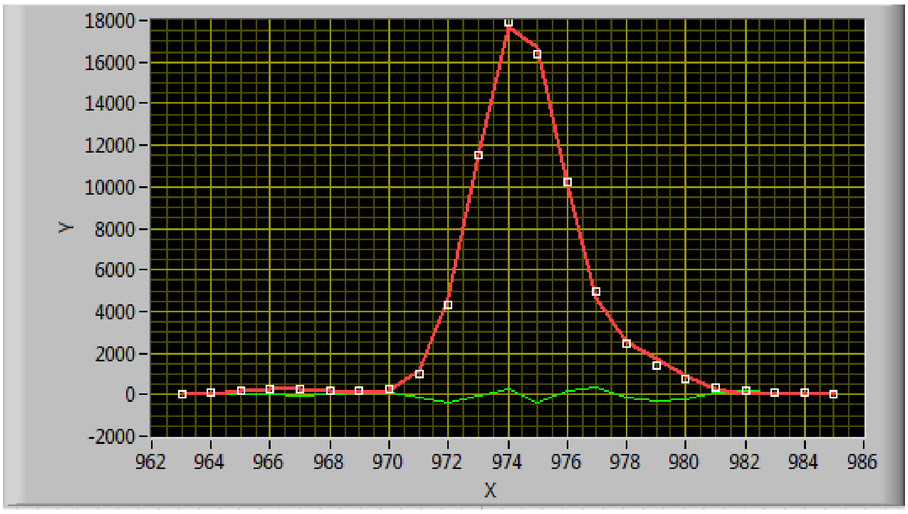

Figure 6.14. The 124-127 u group of peaks and their fits at 99.7 eV electron energy.

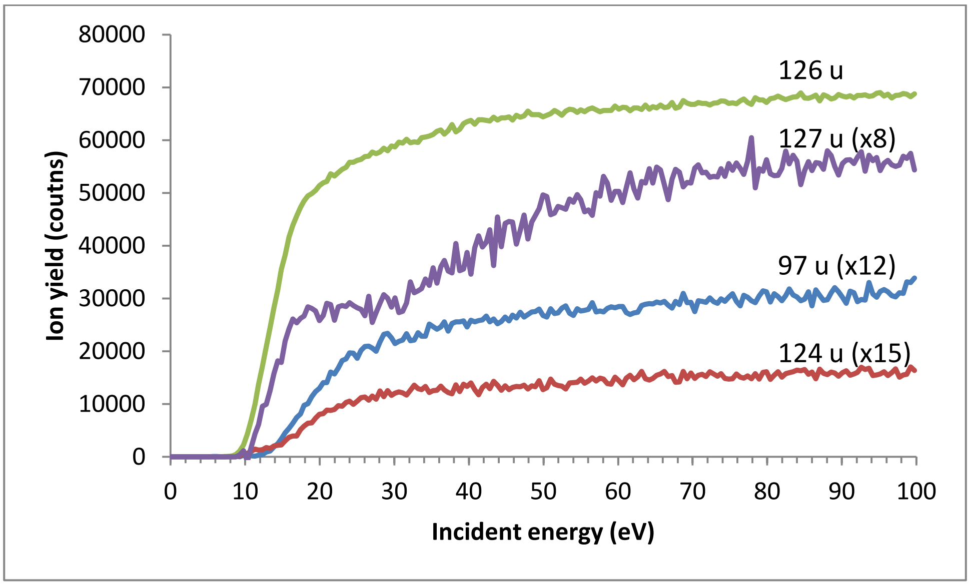

Figure 6.15. Excitation functions for the 124-127 u group and the 97 u peak.

Figure 6.16 shows a comparison between the gaussian peak fitting results and the peak yields at 70 eV for the 124-127 u group as a function of bins.

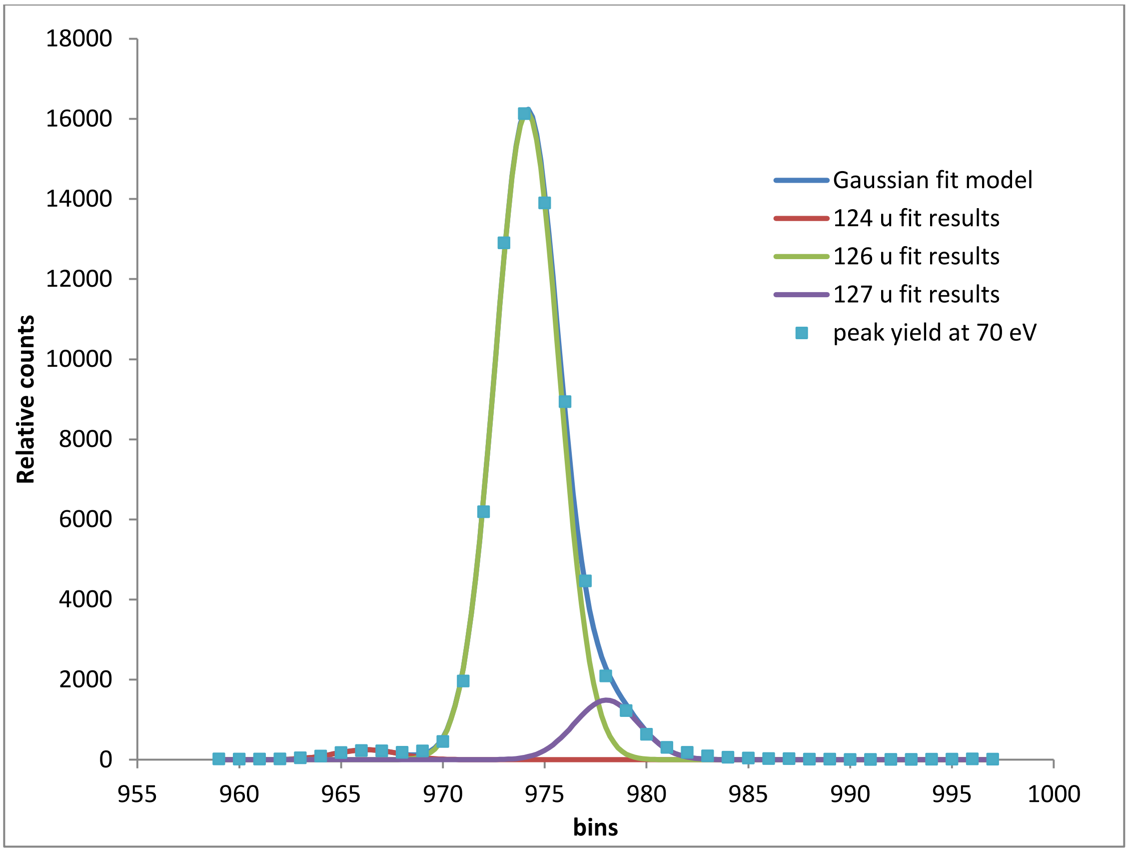

Figure 6.16. Comparison between the gaussian peak fitting results and the peak yields at 70 eV for the 124-127 u group.

6.5 Appearance energies

The appearance energies of all the fragments identified in the Maynooth spectrum were determined from the excitations functions shown in section 6.5. In table 6.2 the appearance energy for each fragment in our mass spectra are compared to the appearance energies determined by Jochims *et al* [51]. The uncertainty in each determination is also included in the table.

m/q	Maynooth data 70 eV electrons	Uncertainty	Jochims et al 20 eV photons	Uncertainty
26	18.5	0.3		
27	17.5	0.3		
28	14.0	0.3	13.6	0.1
29	14.0	1.0		
36	17.0	1.0		
37	28.0	1.0		
38	21.0	0.3		
39	16.5	0.3	14.4	0.1
40	14.3	0.3		
41	18.0	0.3		
42	14.0	0.3		
43	13.8	0.3	11.9	0.1
44	14.3	0.3		
45	12.8	0.3		
51	12.0	0.3		
52	12.0	1.0		
53	15.0	1.0		
54	13.8	0.3	≈12.9	
55	12.0	0.3	11.7	0.1
56	12.3	0.3		
70	14.3	0.3		
71	14.3	0.3		
82	13.3	0.3	13.20	0.05
83	11.0	0.3	10.70	0.05
84	12.0	0.3		
97	13.0	1.0		
124	15.0	1.0		
126	8.8	0.3	8.82	0.03
127	10.5	0.3		

Table 6.2. Appearance energy determination for the Maynooth thymine fragments compared to Jochims *et al* [51].

An appearance energy is the electron impact energy at which a fragment appears in the mass spectrum. These are important because they give an indication of the fragmentation sequence as the incident energy increases.

Apart from the 126 u appearance energy, the only published appearance energies for positive ionised fragments for thymine are by Jochims *et al* [51]. In this section we compare our excitation functions with those of Jochims *et al* to see whether the appearance energies agree. Because the projectiles are not the same we do not expect any close resemblance between the shapes of the excitation functions obtained by us with electron impact and those of Jochims *et al* obtained by photon impact. The curves from Jochims *et al* have been read from the graphs in their paper. In all cases we have multiplied our excitation function with a factor chosen in order to obtain the best agreement close to the appearance energy.

The appearance energy for the Maynooth thymine parent ion shown in figure 6.17 was found to be 8.8 ± 0.3 eV, which compares well with the value of 8.82 ± 0.03 eV obtained by Jochims *et al* [51]. Table 4 in Jochims *et al* [51] lists several other values obtained by other groups for the ionisation energy of thymine.

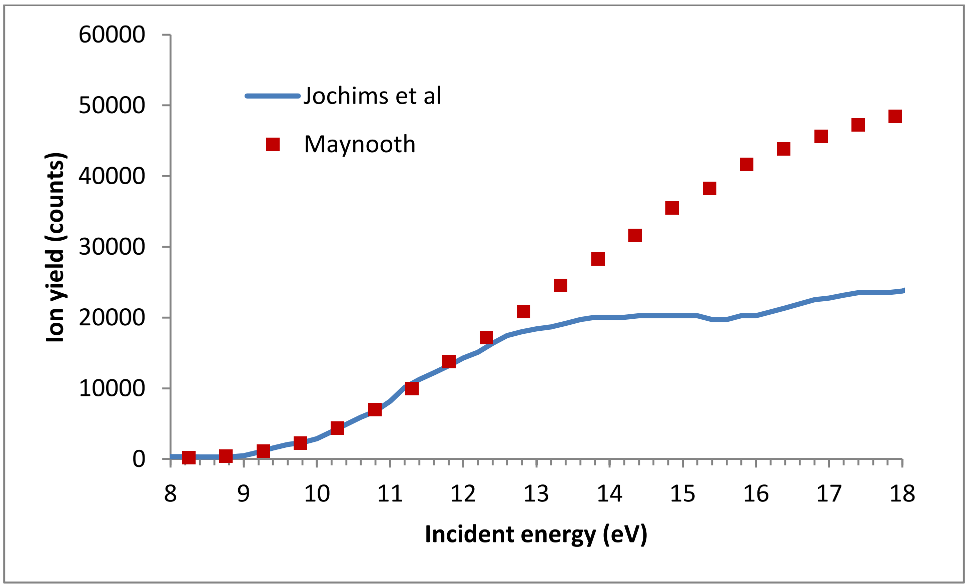

Figure 6.17. Comparison of the 126 u excitation function in the low energy region.

After 126 u, the first fragment to appear in the spectrum is the 83 u fragment, for which the excitation function is shown in figure 6.18, with an appearance energy determination of 11.0 ± 0.3 eV compared to that of 10.7 ± 0.05 eV in the Jochims *et al* spectrum. This fragment forms when the thymine parent ion loses HCNO: [50]

$$C_5H_6N_2O_2^+ \text{ (126u)} \rightarrow C_4H_5NO^+ \text{ (83 u)} + HNCO \text{ (43u)}$$

The 83 u fragment loses CO to form the 55 u fragment ion for which the excitation function is shown in figure 6.19 with an onset of 12.0 ± 0.3 eV compared to Jochims *et al* determination of 11.7 ± 0.1 eV.

$$C_4H_5NO^+ \text{ (83 u)} \rightarrow C_3H_5N^+ \text{ (55 u)} + CO \text{ (28 u)}$$

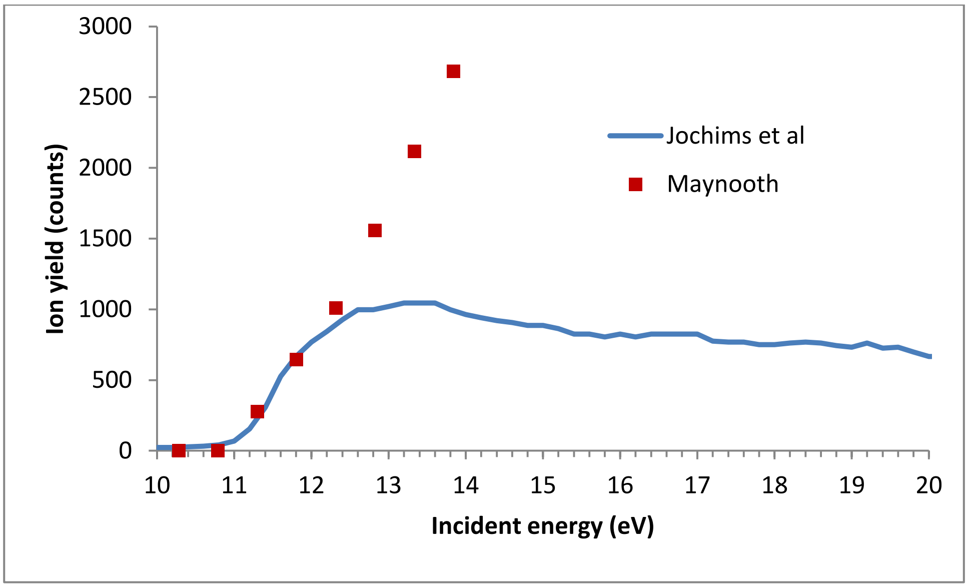

Figure 6.18. Comparison of the 83 u excitation function in the low energy region.

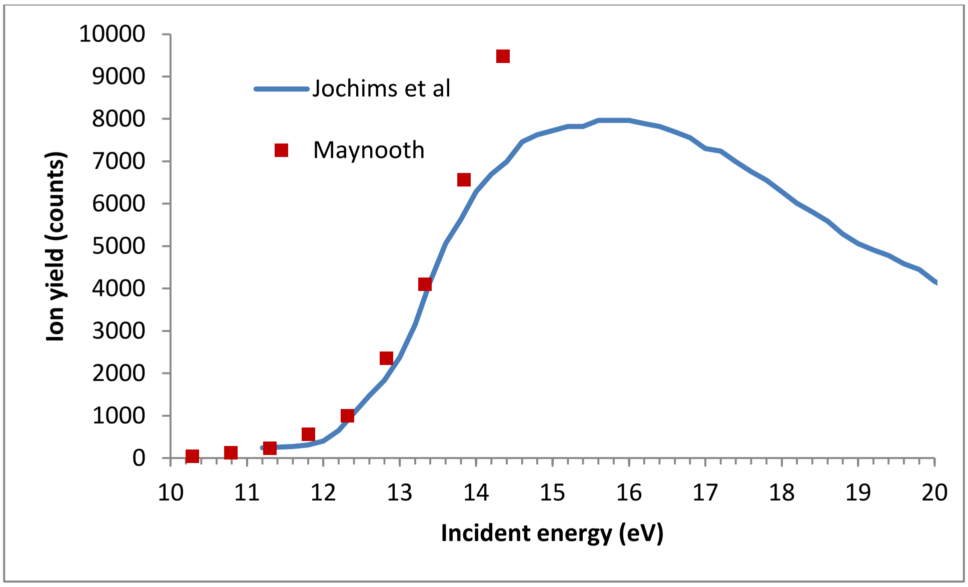

Figure 6.19. Comparison of the 55 u excitation function in the low energy region.

The 83 u fragment ion also loses a hydrogen atom to produce the 82 u fragment. This has a measured appearance energy of 13.3 ± 0.3 eV compared to Jochims *et al* value of 13.20 ± 0.05 eV shown in figure 6.20. The 54 u fragment shown in figure 6.21 has an appearance energy of 13.8 ± 0.3 eV compared to that of ≈12.9 eV from Jochims *et al*. There are two possibilities for the formation of this fragment. The 82 u fragment could lose a CO group or the 55 u fragment could lose a hydrogen atom. [51]

$$C_4H_4NO^+ \text{ (82 u)} \rightarrow C_3H_4N^+ \text{ (54 u)} \rightarrow CO \text{ (28 u)}$$

Both pathways are a possibility in the Maynooth data because the 82 u and 55 u fragments both have a lower appearance energy than the 54 u fragment. In Jochims *et al* data, the only possible pathway is via the 55 u fragment.

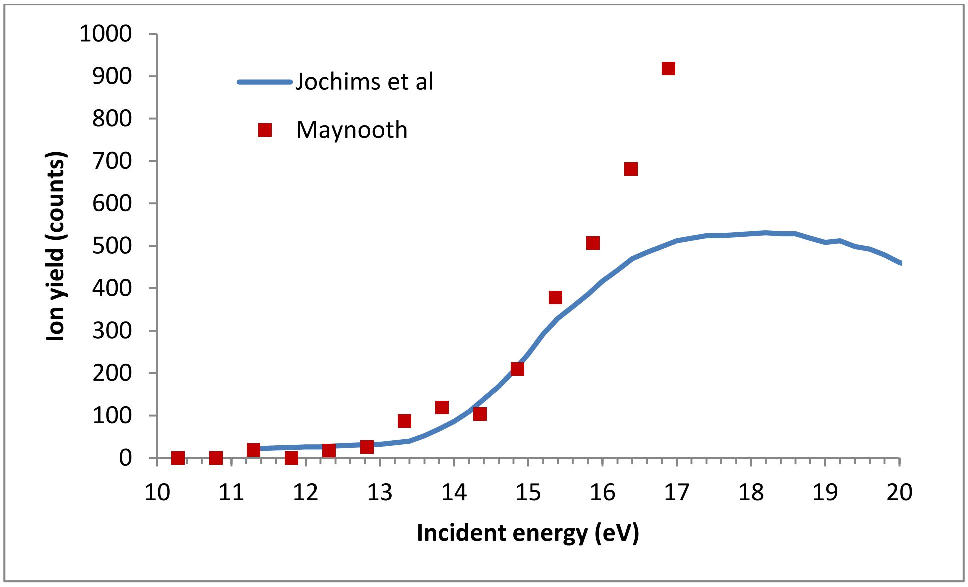

Figure 6.20. Comparison of the 82 u excitation function in the low energy region.

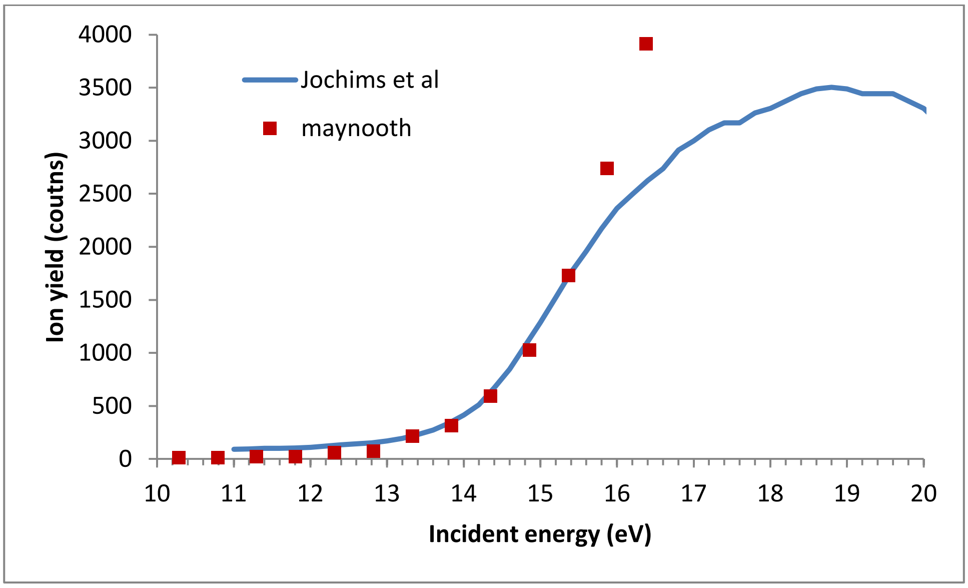

Figure 6.21. Comparison of the 54 u excitation function in the low energy region.

The 28 u fragment shown in figure 6.22 which forms when the 54 u fragment loses C_2H_2. This fragment was found to have an appearance energy of 14 ± 1 eV compared to Jochims *et al* value of 13.6 ± 0.1 eV.

$$C_3H_4N^+ \text{ (54 u)} \rightarrow HCNH^+ \text{ (28 u)} + C_2H_2 \text{ (26 u)}$$

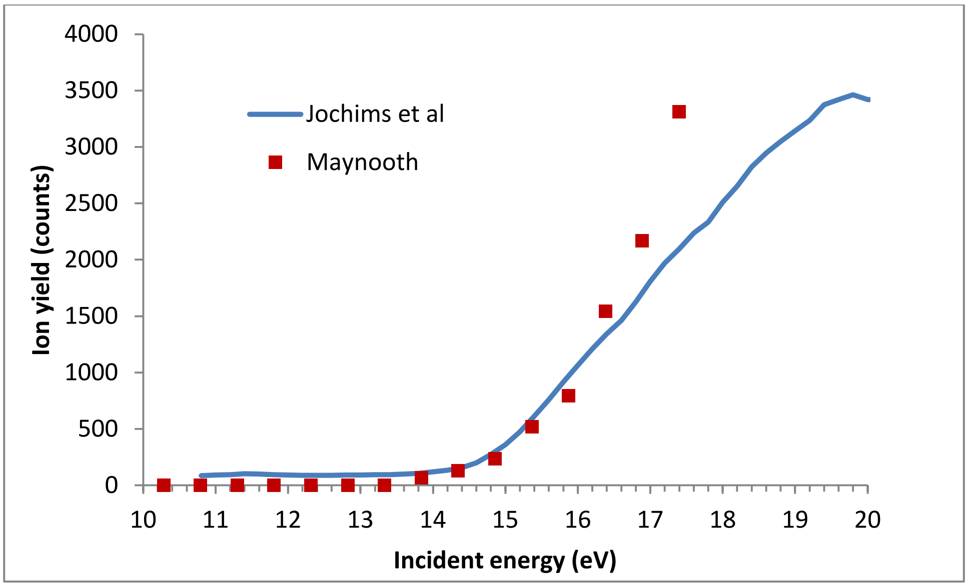

Figure 6.22. Comparison of the 28 u excitation function in the low energy region.

The 39 u fragment shown in figure 6.23 has an appearance energy of 16.5 ± 0.3 eV, this is somewhat higher than the value of 14.4 ± 0.1 eV obtained by Jochims *et al* [51]. The possible formation of the 39 u fragment ($C_3H_3^+$) is the loss of a hydrogen atom from the 40 u fragment. The higher appearance energy of the 39 u fragment proves that this could be the most likely fragmentation pathway.

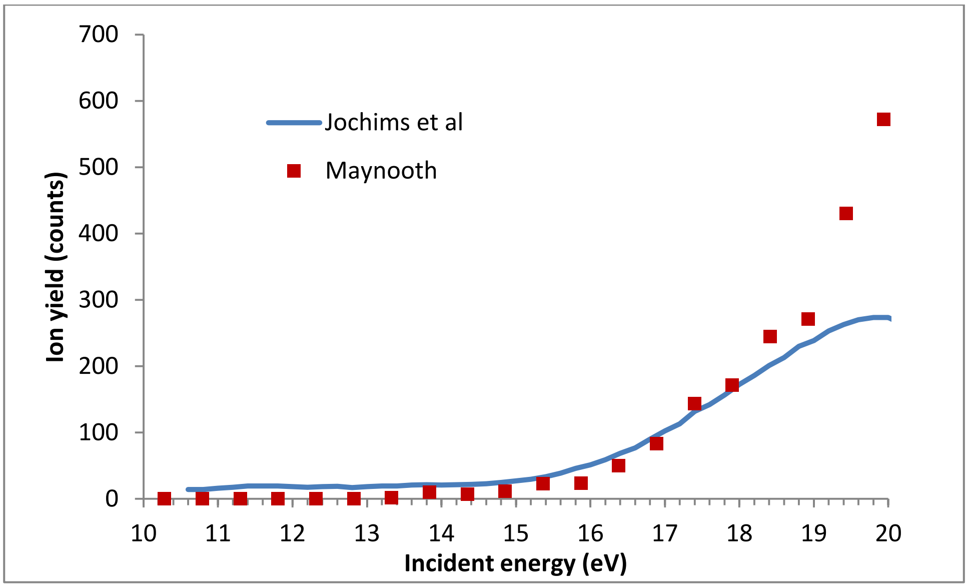

Figure 6.23. Comparison of the 39 u excitation function in the low energy region.

6.6 Total ionisation cross sections

Shown in figure 6.23 is the total ionisation cross section obtained from our data set compared to Shafranyosh *et al* [54], Vinodkumar *et al* [55] and Mozejko & Sanche [56]. We present two total ionisation cross sections in figure 6.24: the sum of all our excitation functions ("sum of fits") and the sum of all the counts in our mass spectra ("sum of bins") both excluding the contributions of masses 18 u and lower. Our "sum of fits" data set was normalised to the data of Vinodkumar *et al* at 100 eV, using a factor of 3.5 x 10^{-5}. The same factor was used for our "sum of bins" data. The good agreement of the normalised curves with both theoretical models suggest that all our excitation functions can be normalised by using the same factor to obtain ionisation cross sections for each of the ionised fragments.

Our data is in very good agreement with the theoretical models from Vinodkumar *et al* and Mozejko & Sanche but our data does not agree with the experimental results from Shafranyosh *et al*. The two ionisation cross sections extracted from our data set agree quite well with each other.

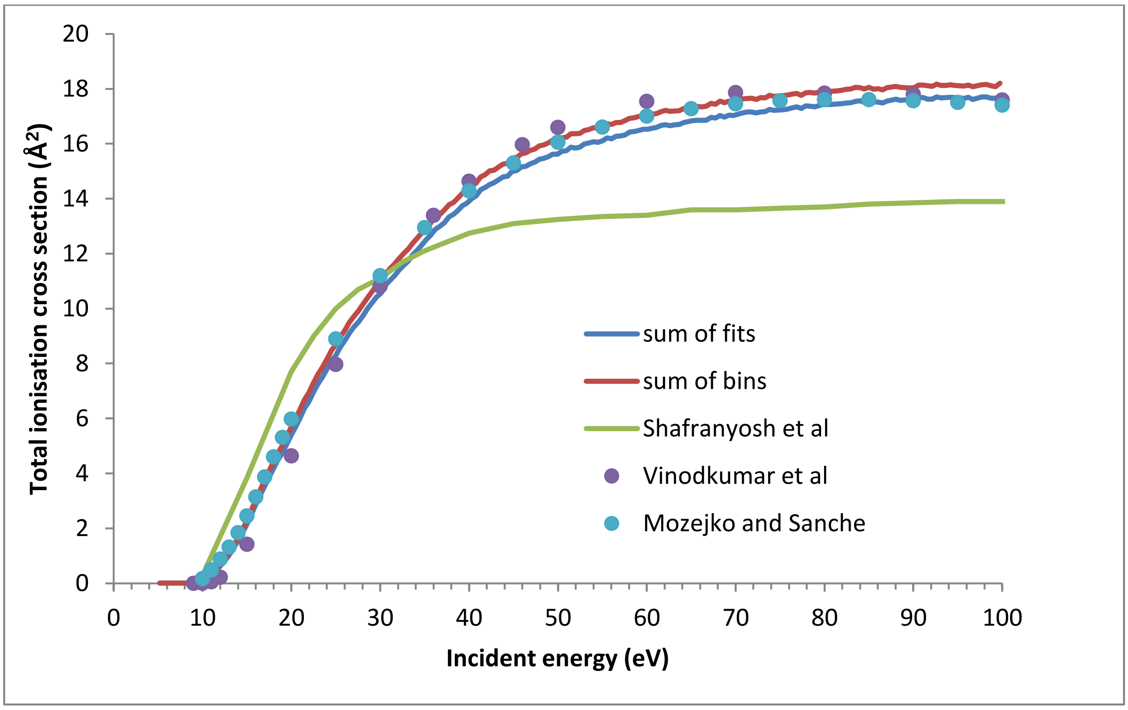

Figure 6.24. Total ionisation cross section of the sum of our fitted data and the sum of all the counts in our spectra compared to the theoretical models of Vinodkumar *et al* [55] and Mozejko and Sanche [56]. The experimental ionisation cross section from Shafranyosh *et al* [54] is also compared to our results.

6.7 Background contribution

Figure 6.25 shows our thymine mass spectrum at cycle 3 compared to the background contribution from cycle 24–cycle 21. The 41–45 u group has the most background contribution and the 28 u peak has a 12% background contribution which may explain the large difference between our 28 u peak and the Rice *et al* 28 u peak in figure 6.2. As discussed in section 5.5.1 and is evident from figure 6.25, the 32 u peak is almost entirely background which points to remnant air in the system. Further investigation into background contribution in the Maynooth apparatus will be conducted in future work.

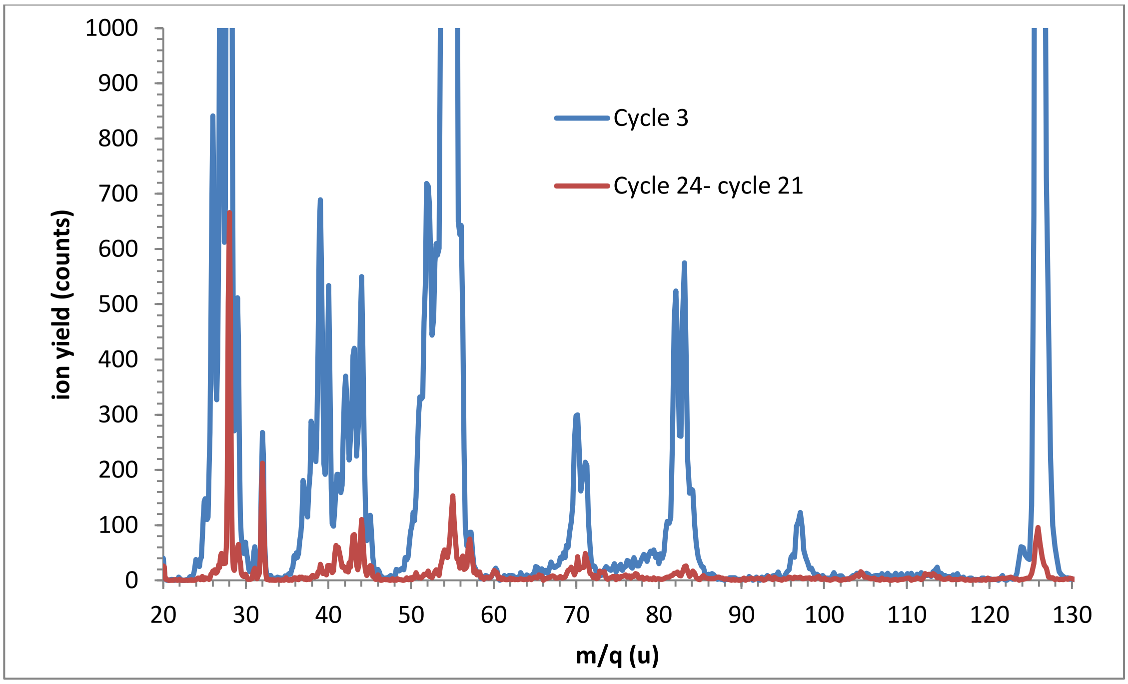

Figure 6.25. Maynooth thymine spectra at cycle 3 compared to the background contribution from cycle 24–cycle 21.

Chapter 7

Conclusion

The main objective of this project was the study of electron-impact fragmentation of thymine. A detailed description of the current apparatus used at the National University of Ireland, Maynooth was given in chapter 3. In the expansion chamber, a resistively heated oven is used to generate the beam of thymine at 180 ^{o}C. The forward focused beam enters the collision chamber where it is crossed with a pulsed beam of electrons produced by an electron gun. The positive ions are extracted into the reflectron chamber where they are detected and mass resolved by a reflectron time-of-flight mass spectrometer.

The electron gun was calibrated to produce a stable beam of electrons with a constant beam current down to 16 eV, and with approximately 60% of the current at 9 eV, allowing us to see the onset of the thymine parent ion peak (126 u) at 8.8 eV. A correction factor was used to correct our data for the depletion in our thymine beam during data accumulation. A study of the water peaks in our mass spectrum was conducted to calibrate the incident energy scale for our excitation functions.

As part of this project, a LabVIEW program was developed to automatically fit the peaks in our spectrum with normalised Gaussian functions. This allowed us to obtain accurate peak areas for all our peaks over a range of 0-99.7 eV from a single data set. This program helped to significantly reduce the time needed to create the excitation functions for the main fragments in our mass spectrum. This program will be used to obtain accurate peak areas for future experiments with adenine, cytosine, guanine and uracil.

The relative intensity of the peaks in our mass spectrum at 70 eV was compared to other groups. All data in the spectrum was set with respect to the 55 u peak due to it being the most abundant in our spectrum. Our data agrees quite well with spectra obtained by other groups using electron and photon impact. Excitation functions were created for the main fragments in our spectrum using the Gaussian fitting LabVIEW program. The appearance energies were determined from the excitation functions and compared to Jochims *et al* [*Chem Phys* **314** (2005) 263-285]. Our data is in good agreement with theirs and the appearance energies give us an insight into the fragmentation processes of thymine induced by electron impact. These processes are relevant for the improvement of our understanding of the processes that are happening on the microscopic scale, when ionising radiation passes through living cells. The total ionisation cross section of our mass spectrum was compared to other groups and agrees quite well with their data.

Experiments are already underway at Maynooth to study electron induced fragmentation on adenine, cytosine, guanine and uracil. Future plans involve the replacement of the oven with a new type of source. This new source will allow the biomolecules to be replaced without the need to open up the expansion chamber and release the vacuum. Other plans for the future are the detection of neutral metastable fragments using the metastable detector in the collision chamber, a redesign of the electron gun using molybdenum lens elements and the replacement of the diffusion pump on the expansion chamber with a turbomolecular pump.

References

[1] L. Sanche, *Eur. Phys. J. D*, **35** (2005) 367-390

[2] X. Pan and L. Sanche, *Phys. Rev. Lett.* **94** (2005) 198104

[3] H. Abdoul-Carime, M.A. Huels, L.Sanche, F. Bruening, E. Illenberger, *J. Chem. Phys.* **113** (2000) 2517

[4] K. Aflatooni, G.A. Gallup, P.D. Burrow, *J. Phys. Chem.* **102** (1998) 6205

[5] S. Denifl, S. Matejcik, B. Gstir, G. Hanel, M. Probst, P. Scheier and T. 0.Mark, J. *Phys. Chem.* (2002)

[6] J. E. Turner, "Atoms, *Radiation, and Radiation Protection*", Wiley-VCH (2010)

[7] S. Gohlke and E. Illenburger, *Europhysics News* **33** (2002) 207-209

[8] http://en.wikipedia.org/wiki/File:Thymine-3D-balls.png

[9] I. Baccarelli, I. Bald, F. A. Gianturco, E. Illenburger and J. Kopyra *Physics Reports* **508** (2011) 1-44

[10] B.Boudaiffa, P.Cloutier, D.Hunting, M.A. Huels and L.Sanche, *Science* **287** (2000) 1658

[11] B. D. Micheal, P.A. O'Neill, *Science* **287** (2000) 1658

[12] L. Aravind, D. Roland Walker, Eugene V. Koonin, *Nucleic Acid Research*, **27**, 5, (1999) 1223-1242

[13] J. K. Moore & J. E. Haber *Mol Cell Biol.* **5** (1996) 2164-73.

[14] M. Mc Vey & M. E. Lee, *Trends in Genetics* **24** (11) (2008) 529–538

[15] F.Martin, P.D. Burrow, Z.Cai, P.Cloutier, D.Hunting, L.Sanche, *Phys. Rev. Lett.* **93** (2004) 068101

[16] P. Burrow, G. A. Gallup, A. M. Scheer, G. Denifl, S. Ptasinska, T. Märk, and P. Scheier *J. Chem. Phys.* **124** (2006) 124310

[17] H. Hotop, M. W. Ruf, M. Allan and I. I. Fabrikant, *"Advances in atomic, molecular, and optical physics"*, **49** (2003) 85-215

[18] X. Pan, P. Cloutier, D. Hunting and L. Sanche, *Phys. Rev. Lett*. **90**, (2003) 208102

[19] M. A. Huels, I. Hahndorf, E. Illenberger, and L Sanche *J. Chem. Phys.* **108**, 1309 (1998)

[20] S. Denifl, S. Ptasinska, G. Hanel, B. Gstir, P. Scheier, M. Probst, B. Farizon, M. Farizon, S. Matejcik, E. Illenberger and T. D. Mark *Phys. Scr.* **252** (2004)

[21] S. Denifl, S. Ptasinska, M. Probst, J. Hrusak, P.Scheier and T.D Mark *J.Phys. Chem. A* **108** (2004) 6562 - 6569

[22] S. Ptasinska, S. Denifl, B. Mroz, M. Probst, V. Grill, E. Illenberger, P. Scheier and T.D. Mark, *J. Chem. Phys*. **123** (2005) 124302

[23] S. Ptasinska, S. Denfl, V. Grill, T. D. Mark, P. Scheier, S. Gohlke, M. A. Huels and E. Illenberger, *Angew. Chemie. Int. Ed.* **44** (2005) 1647

[24] S. Ptasinska, S. Denfl, V. Grill, T. D. Mark, P. Scheier, S. Gohlke, M. A. Huels and E. Illenberger, *Angew. Chemie. Int. Ed.* **44** (2005) 6941

[25] H. Abdoul-Carime, S. Gohlke and E. Illenberger, *Phys. Rev. Lett.* **92** (2004) 168103

[26] J. M. Rice, G. O. Dudek and M. Barber, *J. Am. Chem. Soc.* **87-20** (1965) 4569-4576

[27] M. Imhoff, J. Deng and M.A. Huels, *Int. J. Mass Spect*. **245** (2005) 68-77

[28] I. I. Shafranyosh, M. I. Sukhoviya, M. I. Shafranyosh, and L. L. Shimon, *Technical Physics*, **53** (2008) 1536-1540

[29] H. W. Jochims M. Schwell, H. Baumgartel and S. Leach, *Chem Phys* **314** (2005) 263-285

[30] E. Itala, D. T. Ha, K. Kooser, E. Rachlew, M. A. Heuls and E. Keuk, J. Chem. Phys. **133** (2010) 154316

[31] J. Tabet, S. Eden, S. feil, H. Abdoul-Carmine, B. Farizon, M. Farizon, S. Ouaskit and T.D. Mark, *Int. J. Mass Spect*. **292** (2010) 53–63

[32] T. Schlatholter, R. Hoekstra and R. Morgenstern, *Int. J. Mass Spect*. **233** (2004) 173-179

[33] J. H. Gross *"Mass spectrometry"* Springer (1965)

[34] C. G. Herbert and R. A. W. Johnstone *"Mass spectrometry basics"* CRC (2003)

[35] www.bris.ac.uk/nerclsmsf/images/quadrupole.gif

[36] www.instructor.physics.lsa.umich.edu/advlabs/Mass_Spectrometer/MassSpecQMS.pdf

[37] E. de Hoffman, V. Stroobart "*Mass Spectrometry Principles and applications"* Wiley (1999)

[38] www.nature.com/nrd/journal/v2/n2/full/nrd1011.html

[39] S. Bari, R. Hoekstra and T. Schlatholter, *Int. J. Mass Spect*. **209** (2011) 64-70

[40] W.C. Wiley, I.H. McLaren, *The review of Scientific instruments* **26** (1955) 12

[41] B.A. Mamyrin, *Int. J. Mass Spect*. **206** (2001) 251-266

[42] Model DG535 Digital Delay/Pulse Generator, Stanford Research Systems, Inc, 2.4, November 1997

[43] Model 7886 2 GHz Multiscaler User Manual, FAST ComTEC, 2.1, September 1998

[44] *"Electron and Ion Collisions on Adenine and Thymine"*, Jason James Howard, MSc thesis, National University of Ireland, Maynooth, October 2009

[45] *"Development of an Apparatus for the Study of Electron Impact Fragmentation of Molecular Clusters"*, Gerard Thomas Barrett, MSc thesis, National University of Ireland, Maynooth, October 2008

[46] Y. Itikawa and N. Mason, *J. Phys. Chem.* **34** (2005) 1

[47] H. C. Straub, B. G. Lindsay, K. A. Smith, and R. F. Stebbings, *J. Chem.Phys.* **108** (1998) 109

[48] B. G. Lindsay and M. A. Mangan, "*Photon and Electron Interactions with Atoms, Molecules and Ions*", Landolt-Bornstein **Vol. I/17**, Subvolume C, edited by Y. Itikawa, Springer, New York (2003)

[49] National Institute of Standards and Technology – Chemistry webbook (http://webbook.nist.gov/chemistry/)

[50] J. M. Rice, G. O. Dudek and M. Barber, *JACS* **87** (1965)

[51] H-W Jochims M. Schwell, H. Baumgartel and S. Leach *Chem Phys* **314** (2005) 263-285

[52] M. Imhoff, Z. Deng, M. A. Heuls, *Int. J. Mass Spect*, **245** (2005) 68–77

[53] J. Tabet, S. Eden, S. Feil, H. Abdoul-Carmine, B. Farizon, M. Farizon, S. Ouaskit and T.D. Mark, *Int. J. Mass Spect*. **292** (2010) 53–63

[54] I. I. Shafranyosh, M. I. Sukhoviya, M. I. Shafranyosh, and L. L. Shimon, *Technical Physics*, **53** (2008) 1536-1540

[55] M. Vinodkumar, C. Limbachiya, M. Barot, M. Swadia and A. Barot, *Int. J. Mass Spect*, **339-340** (2013) 16–23

[56] P. Mozejko and L. Sanche, *Radiation Physics and Chemistry,* **73** (2005) 77–84

Appendix

LabVIEW C code used in *multispectrum.vi*

```
#include <userint.h>
#include “test.h”
#include <utility.h>
#include “lw7887.h”

static unsigned short int fifo0, fifo1, fifo2, fifo3;
static unsigned int base, base1, base2, base3, base4, base5, base6,
base7, base8, base9, base10;
static unsigned char creg, fcreg, fscreg
void cardreset()

{
creg = 0x00;
fcreg = 0xf0;
outportb(base3,fcreg);
outportb(base1,creg); /* /RES=0, OUT=0 */
creg = 0x10; outportb(base1,creg); /* /RES=1 */
}

void fiforeset()

{
fcreg = inportb(base3);
fsreg = inportb(base5);
fcreg &= 0x0f; outportb(base3,fcreg);
/* FFRES=0 */
fcreg |= 0x01; outportb(base3,fcreg);
/* FRCLK=1 */
fcreg &= 0xfe; outportb(base3,fcreg);
/* FRCLK=0 */
fcreg |= 0x01; outportb(base3,fcreg);
/* FRCLK=1 */
fcreg &= 0xfe; outportb(base3,fcreg);
/* FRCLK=0 */
fcreg |= 0x01; outportb(base3,fcreg);
/* FRCLK=1 */
fcreg &= 0xfe; outportb(base3,fcreg);
/* FRCLK=0 */
fcreg |= 0x01; outportb(base3,fcreg);
```

```
/* FRCLK=1 */
fcreg &= 0xfe; outportb(base3,fcreg);
/* FRCLK=0 */

fifo0 = inport(base);
fifo1 = inport(base2);
fifo2 = inport(base4);
fifo3 = inport(base6);
fifo0 = inport(base);
fifo1 = inport(base2);
fifo2 = inport(base4);
fifo3 = inport(base6);
fifo0 = inport(base);
fifo1 = inport(base2);
fifo2 = inport(base4);
fifo3 = inport(base6);

fifo0 = inport(base);
fifo1 = inport(base2);
fifo2 = inport(base4);
fifo3 = inport(base6);

fcreg |= 0xf0; outportb(base3,fcreg);
/* /FFRES=1 */
fsreg = inportb(base5);
/* printf("%02X ",fsreg); */
fcreg |= 0x01; outportb(base3,fcreg);
/* FRCLK=1 */
fcreg &= 0xfe; outportb(base3,fcreg);
/* FRCLK=0 */
fcreg |= 0x01; outportb(base3,fcreg);
/* FRCLK=1 */
fcreg &= 0xfe; outportb(base3,fcreg);
/* FRCLK=0 */
fsreg = inportb(base5);
/* printf("%02X\n",fsreg); */
}

int testcard() /* test card to check if it is present and OK */
{
unsigned int itest;
int i,k;
creg = inportb(base1);
creg &= 0xfb; /* STARTI=0 */
fcreg = inportb(base3);
fsreg = inportb(base5);
fcreg |= 0x02; outportb(base3,fcreg); /* SETA=1 */
```

```
outport(base8, 0xA5A8);
outport(base10, 0xBBBB); /* P=BBBBA5A8 */
itest = inport(base8) & 0xFFF8;
if(itest != 0xA5A8)return FALSE;
fcreg |= 0x08; outportb(base3,fcreg); /* SEV=1 */
creg |= 0x08; outportb(base1,creg); /* ENA=1 */
creg |= 0x02; outportb(base1,creg); /* ENDR=1 */
creg |= 0x04; outportb(base1,creg); /* STARTI */
creg &= 0xfb;

/* FS */
for (k=0; k<1024; k++) {
for (i=0; i<4; i++) {
fsreg = inportb(base5);
if(fsreg & 0x40)break;
fifo3 = inport(base10);
}
if(fsreg & 0x40) {
fifo3 = inport(base6);
fifo2 = inport(base4);
fifo1 = inport(base2);
fifo0 = inport(base);
if (fifo3 != 0xBBBB) return FALSE;
if (fifo2 != itest) { /* may be new firmware version */
if (fifo2==0xA5A9 && itest==0xA5A8) itest++;
else return FALSE;
}
if (fifo1 != 0xAAAA) return FALSE;
if (fifo0 != 0xAAAA) return FALSE;
}
else {
return FALSE; /* printf("geht nicht! (OR == 0)\n"); */
}
itest++;
}
return TRUE;

}

int lw7886_init(unsigned int newbase)

{
base = newbase;
base1 = base+1;
base2 = base+2;
base3 = base+3;
base4 = base+4;
```

```
base5 = base+5;
base6 = base+6;
base8 = base+8;
base10 = base+10;
cardreset();
creg = inportb(base1);
fcreg = inportb(base3);
fsreg = inportb(base5);
if (!(creg & 0x04)) return FALSE;
/* OFF != 1 -> no 7886 found! */
creg = (creg & 0xfb); /* STARTI=0 */
fiforeset();
if (!testcard()) return FALSE;
cardreset();
fiforeset();
return TRUE;
}

int lw7886_acq(unsigned int *buffer, int range, in sweeps, double
timeout)
{

int hitim;
unsigned int I;
int amount;
int range5;
int counter=0;
double starttime;
unsigned int preset;
creg = inportb(base1);
creg = (creg & 0xfb); /* STARTI=0 */
fcreg = inportb(base3);
fsreg = inportb(base5);
starttime=Timer();
range &=0xffffff00;
range5=range>>5;
preset=(unsigned)-range5;
fiforeset();

creg &= 0xfe; outportb(base1,creg); /* runs("mode=0"); */
creg &= 0xfd; outportb(base1,creg); /* runs("endr=0"); */
outpw (base8, (preset & 0x0000fff8)|0x3);
outpw (base10, (preset & 0xffff0000)>>16);
creg &= 0xf7; outportb(base1,creg); /* runs("ena=0"); */
creg |= 0x02; outportb(base1,creg); /* runs("endr=1"); */
creg |= 0x08; outportb(base1,creg); /* runs("ena=1"); */
for(;;) { /*Dummy read until output ready*/
```

```
if(inpw(base8)& 0x02)

{
while(inp(base5)&0x40)

{
fifo3=inpw(base6);
fifo2=inpw(base4);
fifo1=inpw(base2);
fifo0=inpw(base);
hitim=(fifo0+fifo3*65536-preset)<<5;
if (fifo0 & 0x01) ss[hitim]++;
if (fifo0 & 0x02) ss[1+hitim]++;
if (fifo0 & 0x04) ss[2+hitim]++;
if (fifo0 & 0x08) ss[3+hitim]++;
if (fifo0 & 0x10) ss[4+hitim]++;
if (fifo0 & 0x20) ss[5+hitim]++;
if (fifo0 & 0x40) ss[6+hitim]++;
if (fifo0 & 0x80) ss[7+hitim]++;
if (fifo0 & 0x0100) ss[8+hitim]++;
if (fifo0 & 0x0200) ss[9+hitim]++;
if (fifo0 & 0x0400) ss[10+hitim]++;
if (fifo0 & 0x0800) ss[11+hitim]++;
if (fifo0 & 0x1000) ss[12+hitim]++;
if (fifo0 & 0x2000) ss[13+hitim]++;
if (fifo0 & 0x4000) ss[14+hitim]++;
if (fifo0 & 0x8000) ss[15+hitim]++;
if (fifo1 & 0x01) ss[16+hitim]++;
if (fifo1 & 0x02) ss[17+hitim]++;
if (fifo1 & 0x04) ss[18+hitim]++;
if (fifo1 & 0x08) ss[19+hitim]++;
if (fifo1 & 0x10) ss[20+hitim]++;
if (fifo1 & 0x20) ss[21+hitim]++;
if (fifo1 & 0x40) ss[22+hitim]++;
if (fifo1 & 0x80) ss[23+hitim]++;
if (fifo1 & 0x0100) ss[24+hitim]++;
if (fifo1 & 0x0200) ss[25+hitim]++;
if (fifo1 & 0x0400) ss[26+hitim]++;
if (fifo1 & 0x0800) ss[27+hitim]++;
if (fifo1 & 0x1000) ss[28+hitim]++;
if (fifo1 & 0x2000) ss[29+hitim]++;
if (fifo1 & 0x4000) ss[30+hitim]++;
if (fifo1 & 0x8000) ss[31+hitim]++;
}
outpw(base8,inpw(base8)|0x02);
counter++;
}
```

```
if (counter==sweeps)
return counter;
if(Timer()-starttimer>timeout)
return counter;

}
}
```

Code for LabVIEW Programs

Spectra-vs-E-v7.vi Back panel 1

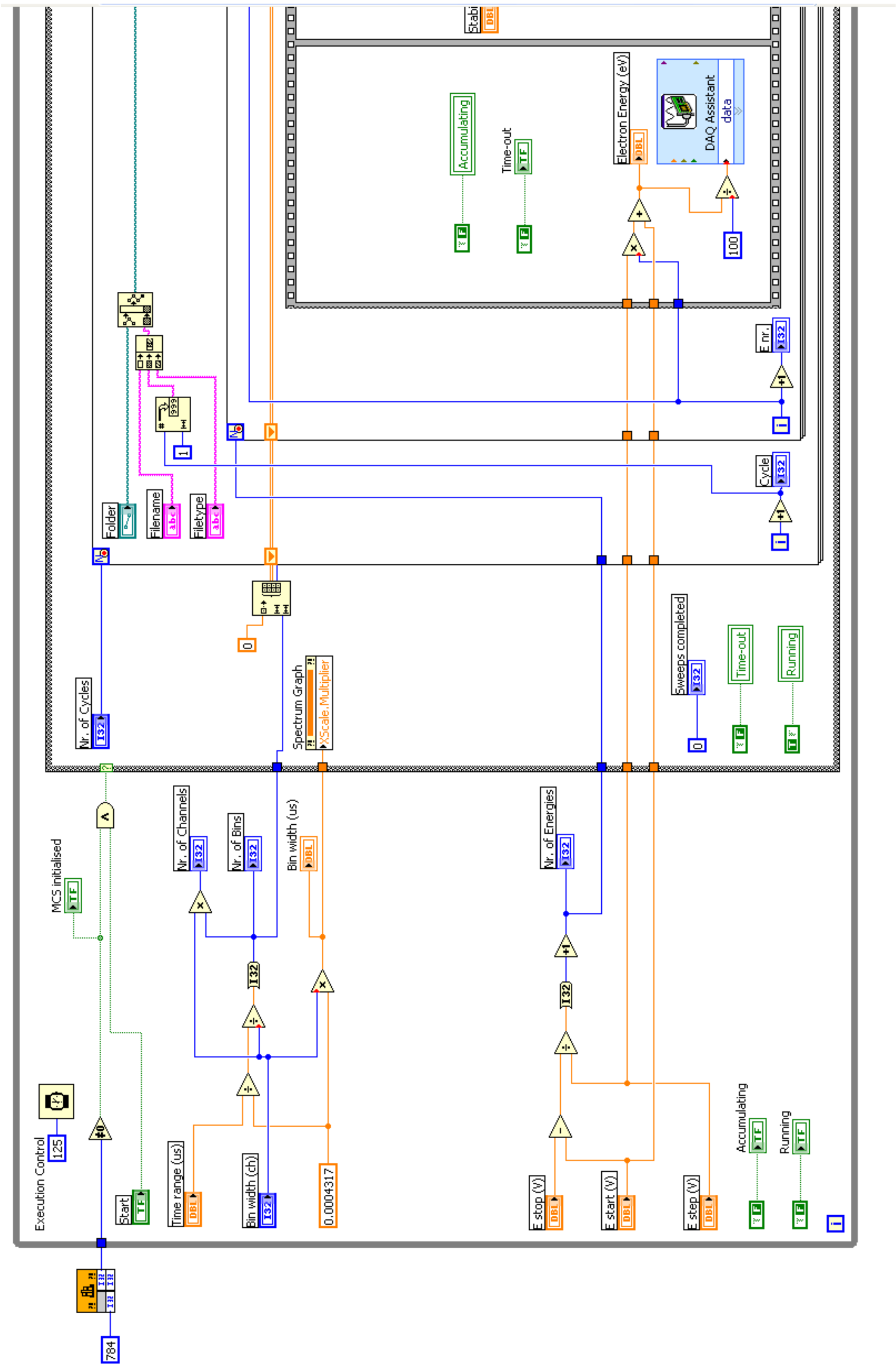

Spectra-vs-E-v7.vi Back panel 2

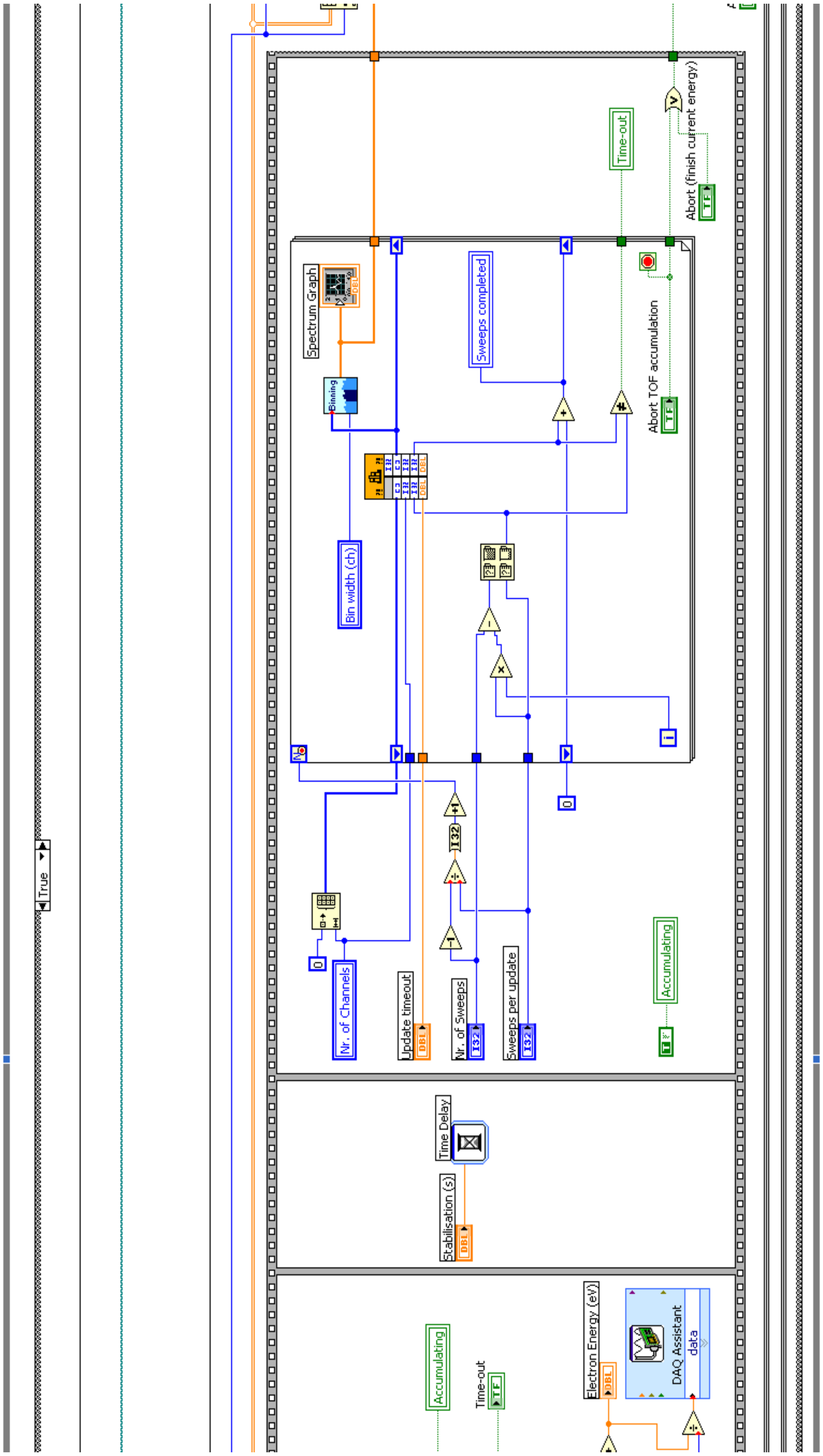

Spectra-vs-E-v7.vi **Back panel 3**

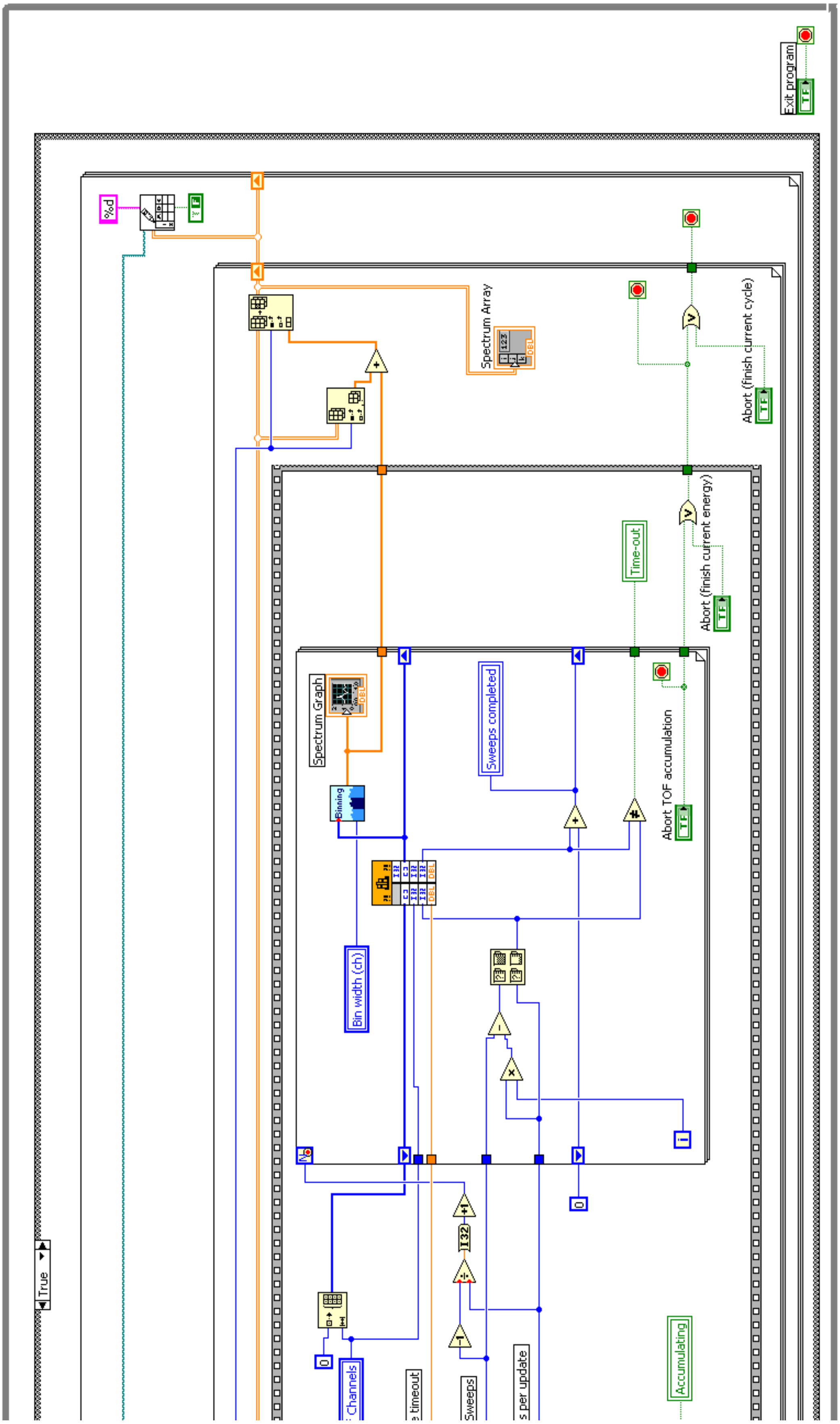

***multigauss test.vi* Back panel 1**

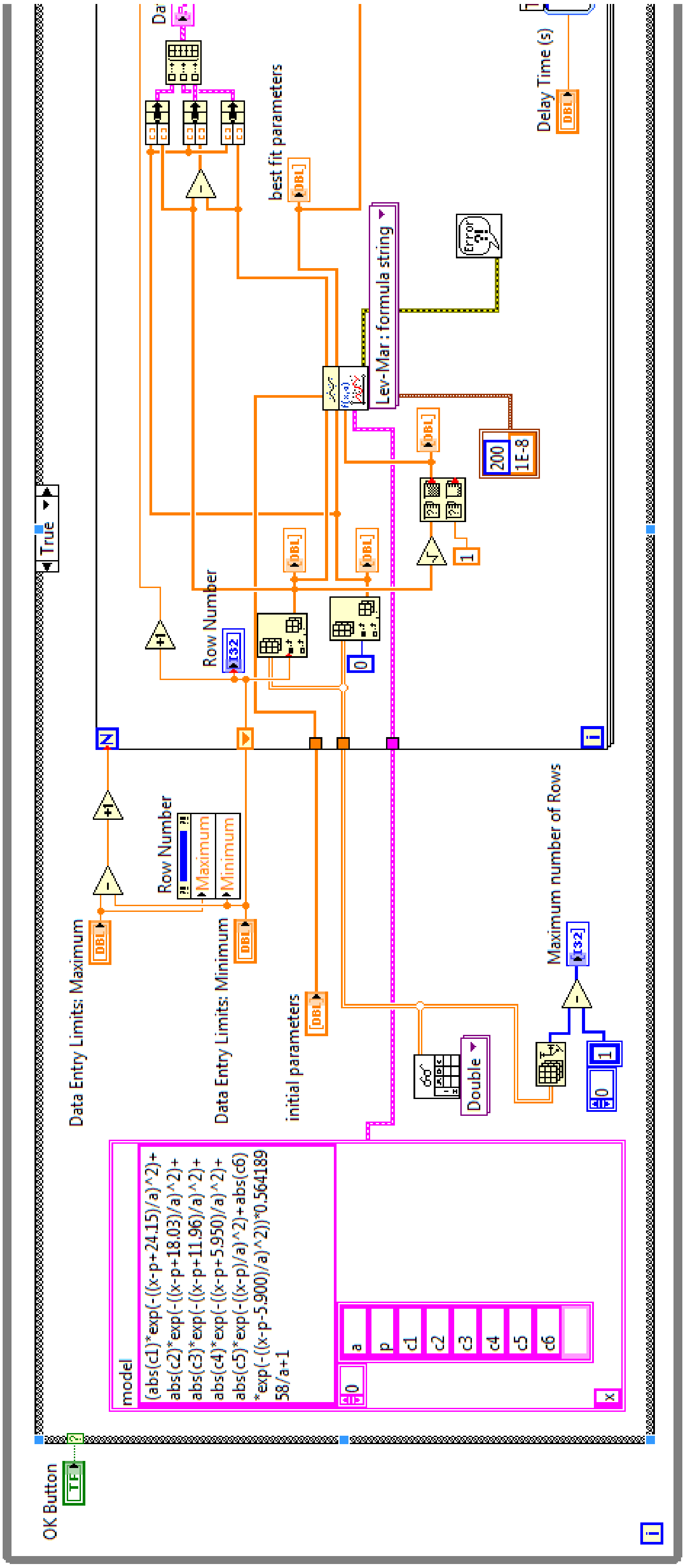

```
model
(abs(c1)*exp(-((x-p+24.15)/a)^2)+
abs(c2)*exp(-((x-p+18.03)/a)^2)+
abs(c3)*exp(-((x-p+11.96)/a)^2)+
abs(c4)*exp(-((x-p+5.950)/a)^2)+
abs(c5)*exp(-((x-p)/a)^2)+abs(c6)
*exp(-((x-p-5.900)/a)^2))*0.564189
58/a+1
```

multigauss test.vi **Back panel 2**